2016

Studies of Dirac and Weyl fermions by angle resolved photoemission spectroscopy

Lunan Huang
Iowa State University

Studies of Dirac and Weyl fermions by angle resolved photoemission spectroscopy

by

Lunan Huang

A dissertation submitted to the graduate faculty

in partial fulfillment of the requirements for the degree of

DOCTOR OF PHILOSOPHY

Major: Condensed Matter Physics

Program of Study Committee:

Adam Kaminski, Major Professor

Sergey L. Budko

Rebecca Flint

John G. Lajoie

Guang Song

Jiang Wang

Iowa State University

Ames, Iowa

2016

DEDICATION

I would like to dedicate this thesis to my wife, Wenjia, without whose support I would not have been able to complete this work.

TABLE OF CONTENTS

LIST OF TABLES

LIST OF FIGURES

ACKNOWLEDGEMENTS

I would like to take this opportunity to express my thanks to those who helped me with various aspects of conducting research and the writing of this dissertation.

First and foremost, thanks to Dr. Adam Kaminski for his guidance and support throughout this research and the writing of this dissertation. His insights and words of encouragement have often inspired me and renewed my hopes for completing my graduate education. He also has an open mind and really encourages students to explore novel areas in both research and life. I feel extremely lucky to be one of his students. Also, many thanks to my other committee members for their efforts and contributions to this work: Drs.

Sergey L. Budko, Rebecca Flint, John G. Lajoie, Guang Song and Jiang Wang.

I would also like to thank my former and present colleagues in Adam's group for their help in the experiment and data analysis part during my Ph.D. study: Daixiang Mou, Rui Jiang, Yun Wu, and Benjamin Schrunk.

My gratitude is also given to numerous academic colleagues around the world, including Prof. Paul Canfield, Prof. Michael Tringides, Dr. Myron Hupalo, Dr. Valentin Taufour, Tej Lamichhane, and Matthew Hershberger in Ames Laboratory and Iowa State University, Prof. Nandini Trivedi and Tim McCormick in Ohio State University, Dr. Jiaqiang Yan in Oak Ridge National Laboratory, as well as Dr. Masayuki Ochi and Ryotaro Arita in Tohoku University.

Finally I would express my special thanks to my parents Gang Huang and Yan Lan, for their unconditional belief, support, and love.

ABSTRACT

This dissertation consists of three parts. First, we study magnetic domains in $Nd_2Fe_{14}B$ single crystals using high resolution magnetic force microscopy (MFM). In addition to the elongated, wavy nano-domains reported by a previous MFM study, we found that the micrometer size, star-shaped fractal pattern is constructed of an elongated network of nano-domains about 20 nm in width, with resolution-limited domain walls thinner than 2 nm. Second, we studied extra Dirac cones of multilayer graphene on SiC surface by ARPES and SPA-LEED. We discovered extra Dirac cones on Fermi surface due to SiC 6×6 and graphene $6\sqrt{3} \times 6\sqrt{3}$ coincidence lattice on both single-layer and three-layer graphene sheets. We interpreted the position and intensity of the Dirac cone replicas, based on the scattering vectors from LEED patterns. We found the positions of replica Dirac cones are determined mostly by the 6×6 SiC superlattice even graphene layers grown thicker. Finally, we studied the electronic structure of $MoTe_2$ by ARPES and experimentally confirmed the prediction of type II Weyl state in this material. By combining the result of Density Functional Theory calculations and Berry curvature calculations with out experimental data, we identified Fermi arcs, track states and Weyl points, all features predicted to exist in a type II Weyl semimetal. This material is an excellent playground for studies of exotic Fermions.

CHAPTER 1. ANGLE RESOLVED PHOTOEMISSION SPECTROSCOPY (ARPES)

1.1 Introduction

ARPES is an experimental technique that allows to directly study the electronic structure and properties of solids. Over the years it was proven to be extremely useful to measure energy gaps, lifetime of the quasiparticles, interaction between quasiparticles and collective excitations, and many more. In this section, we introduce some basic solid-state concepts such as band structure and Fermi surface. In the next section, we discuss the theoretical basics of ARPES.

1.1.1 Free electron Fermi gas

A free electron gas contains N free electrons not interacting with each other in a finite volume, V. Therefore, the ground state (at temperature T = 0) of N electrons can be found by first determining the energy level of a single electron in V, and then filling these levels according to the Pauli exclusion principle. A free single electron satisfies the time-independent Schrödinger equation

$$-\frac{\hbar^2}{2m}\nabla^2\psi(\mathbf{r}) = \mathcal{E}\psi(\mathbf{r}), \tag{1.1}$$

and the Born-von Karman boundary condition

$$\psi(r_i + L_i) = \psi(r_i), \tag{1.2}$$

where L_i is the size of dimension i where the electrons are confined. The solution to Eq. 1.1 with boundary condition 1.2 is

$$\psi_{\mathbf{k}}(\mathbf{r}) = \frac{1}{\sqrt{V}} e^{i\mathbf{k}\cdot\mathbf{r}}, \tag{1.3}$$

with energy

$$\mathcal{E}(\mathbf{k}) = \frac{\hbar^2 k^2}{2m}, \tag{1.4}$$

where the wave vector $\mathbf{k} = (k_1, k_2, k_3)$ satisfies $k_i = \frac{2\pi n_i}{L_i}, n_i = integer$. A different set of n_i corresponds with a different energy level for the free electron. The Pauli exclusion principle states that no two electrons can have exactly the same set of quantum numbers. In this case, two electrons must have different momentum and/or spins. Thus, to build up the N-electron ground state, we begin by placing two electrons with opposite spins in the $\mathbf{k} = 0$ level, then fill each energy level (in increasing order) with two electrons of opposite spins until we fill all N states with N electrons. A situation where N electrons fills the N lowest states is the ground state of the N-electron system. When N is very large ($\sim 10^{22}$ electrons) the occupied energy levels form a sphere in 3D momentum space with radius k_F. N and k_F are related by

$$N = 2(\frac{4\pi k_F^3}{3})(\frac{V}{8\pi^3}) = \frac{k_F^3}{3\pi^2} V, \tag{1.5}$$

where 2 stands for spin up and spin down, $(\frac{4\pi k_F^3}{3})$ is the volume of the sphere in k space, and $(\frac{V}{8\pi^3})$ is the number of allowed k-values per unit volume in k space. The sphere of radius k_F contains the occupied energy levels by the N electrons called "Fermi sphere". The surface for a Fermi sphere separating the occupied and unoccupied energy levels, is called "Fermi surface". The electrons energy at Fermi surface is

$$\mathcal{E}_F = \frac{\hbar^2 k_F^2}{2m}, \tag{1.6}$$

and it is called "Fermi energy."

When the temperature, T, is non-zero, some of the electrons within energy $k_B T$ below the Fermi surface will become thermally excited, increase their energy and occupy an energy level above Fermi energy, as shown in Figure 1.1. For non-zero temperatures, the Fermi energy is equal to the chemical potential, μ, in the Fermi distribution function:

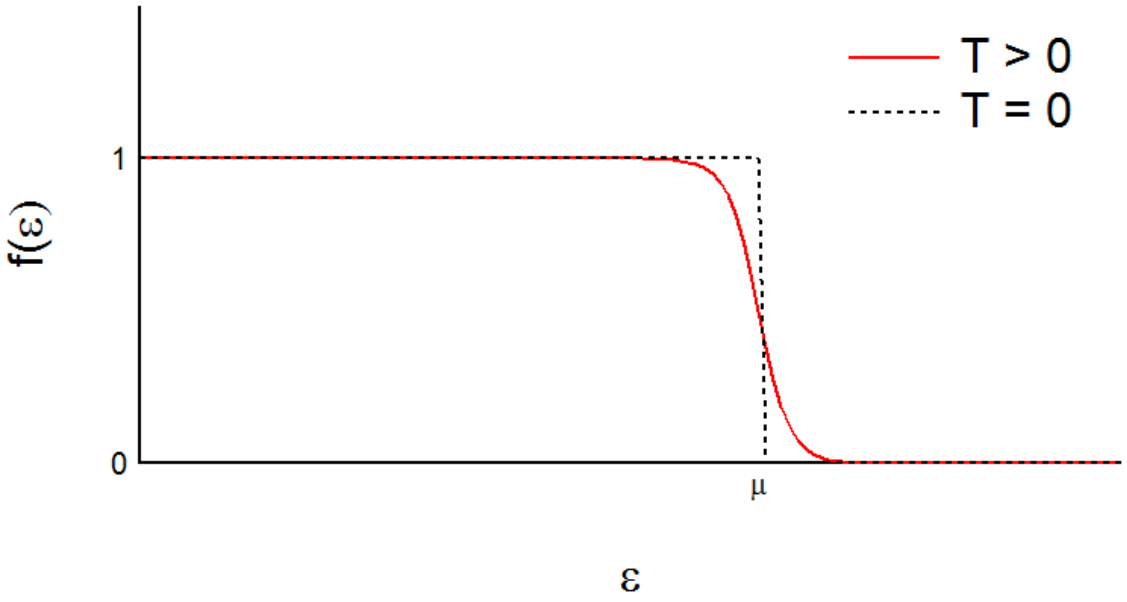

Figure 1.1 The Fermi function 1.7 at T = 0 (black dotted line) and T > 0 (red solid line). The two curves differ only in a region of order, k_BT, about μ.

$$f(\epsilon) = \frac{1}{e^{\frac{\epsilon-\mu}{k_BT}} + 1}. \tag{1.7}$$

At the Fermi energy (chemical potential) the number of energy levels occupied is one-half of the number for the ground state value.

1.1.2 Reciprocal lattice and Brillouin zone

In solid-state physics, a fundamental concept in the description of any crystalline solid is that of the Bravais lattice. The Bravais lattice is an infinite array of discrete points with an arrangement and orientation that appear exactly the same from every point the array is viewed. There could be an atom, a group of atoms, a molecule or an ion at every point for different crystals, but the Bravais heeds only the geometry of the periodic structure, regardless of what unit is at each point. A three-dimensional Bravais lattice consists of all points with position vectors **R** of the form

$$\mathbf{R} = n_1\mathbf{a}_1 + n_2\mathbf{a}_2 + n_3\mathbf{a}_3, \tag{1.8}$$

where $\mathbf{a}_1$, $\mathbf{a}_2$, $\mathbf{a}_3$ are three base vectors and n_i is any integer.

For a given set of points, $\mathbf{R}$, and a plane wave, $e^{i\mathbf{k}\cdot\mathbf{r}}$, the plane wave usually does not have the same periodicity as the Bravais lattice. However, for wave vectors $\mathbf{K}$ satisfying

$$e^{i\mathbf{K}\cdot\mathbf{R}} = 1, \tag{1.9}$$

for all $\mathbf{R}$ in the Bravais lattice, the plane wave will have the same periodicity as the Bravais lattice. Hence, we define the reciprocal lattice for the Bravais lattice points, $\mathbf{R}$, to be the set of all wave vectors, $\mathbf{K}$, that satisfy Eq. 1.9. Based on Eq. 1.9, the three base vectors $\mathbf{b}_i$ of the reciprocal lattice can be generated from the Bravais lattice base vectors, $\mathbf{a}_i$:

$$\mathbf{b}_i = 2\pi\frac{\mathbf{a}_j \times \mathbf{a}_k}{\mathbf{a}_i \cdot (\mathbf{a}_j \times \mathbf{a}_k)}; i, j, k = 1, 2, 3. \tag{1.10}$$

The reciprocal lattice is a Fourier transformation of the Bravais (real) lattice, and the reciprocal lattice of a reciprocal lattice is the real lattice.

The Wigner-Seitz primitive cell of the reciprocal lattice is known as the first Brillouin zone. That is, the area is surrounded by all lines perpendicular, and bisect the origin and all its nearest neighbor points. These lines are shown in Figure 1.2 as red. There are also second, third, etc., Brillouin zones, corresponding to a sequence of disjoint regions (all with the same volume) at increasing distances from the origin. However, other Brillouin zones are replicates to the first. Therefore, we sometimes use " Brillouin zone " to refer only to the first Brillouin zone. For a plane wave, $e^{i\mathbf{k}\cdot\mathbf{r}}$, is identical to $e^{i(2\pi+\mathbf{k}\cdot\mathbf{r})}$ and, the first Brillouin zone contains all electronic information about the crystal.

1.1.3 Band theory and Fermi surface of crystals

The independent electrons in a crystalline periodic potential, $U(\mathbf{r} = U(\mathbf{r} + \mathbf{R}))$, can be described by the Schrödinger equation:

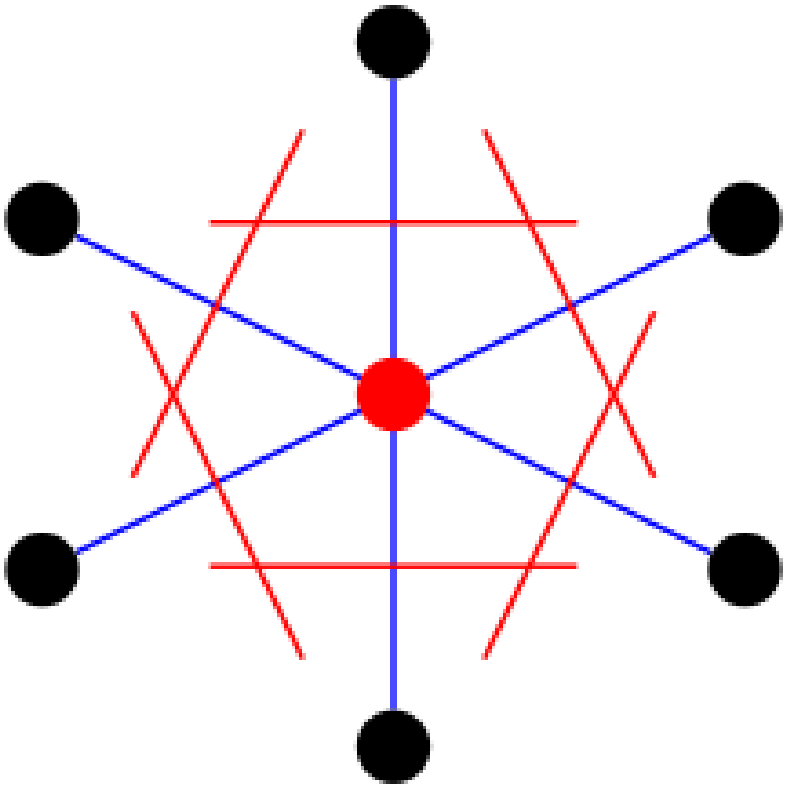

Figure 1.2 Construction of a Wigner-Seitz primitive cell

$$H\psi = (-\frac{\hbar^2}{2m}\nabla^2 + U(\mathbf{r}))\psi = \mathcal{E}\psi. \tag{1.11}$$

According to Bloch's theorem, the eigenstates of Eq. 1.11 can be chosen to have the form of a plane wave times a function with the same periodicity of the Bravais lattice:

$$\psi_{n\mathbf{k}}(\mathbf{r}) = e^{i\mathbf{k}\cdot\mathbf{r}} u_{n\mathbf{k}}(\mathbf{r}), \tag{1.12}$$

where $u_{n\mathbf{k}}(\mathbf{r}+\mathbf{R}) = u_{n\mathbf{k}}(\mathbf{r})$.

The wave vector $\mathbf{k}$ can be always confined to the first Brillouin zone. Any $\mathbf{k}'$ not in the first Brillouin zone can be written as

$$\mathbf{k}' = \mathbf{k} + \mathbf{K}. \tag{1.13}$$

The index n in Eq. 1.12 distinguishes the solutions to the same $\mathbf{k}$ in Eq. 1.11. We can assign n to the levels in such a way that for given n, the eigenstates and eigenvalues are periodic functions of $\mathbf{k}$ in the reciprocal lattice:

$$\begin{aligned} \psi_{n,\mathbf{k}+\mathbf{K}}(\mathbf{r}) &= \psi_{n\mathbf{k}}(\mathbf{r}), \\ \mathcal{E}_{n,\mathbf{k}+\mathbf{K}} &= \mathcal{E}_{n\mathbf{k}}. \end{aligned} \tag{1.14}$$

The family of continuous functions, $\mathcal{E}_{n\mathbf{k}}$, is referred to as the band structure of a solid. They describe the energy levels of an electron in a periodic potential. For each n, the set of energy levels specified by $\mathcal{E}_{n\mathbf{k}}$ is called an energy band.

Similar to the system of N free electrons, a system of N Bloch electrons (electrons in periodic potential) has ground state constructed by occupying the lowest N energy levels, except now the levels are labeled by quantum numbers n and $\mathbf{k}$. When the lowest levels are filled by N electrons, two quite different configurations can result, depending if there are bands partially filled. If a certain number of bands is completely filled and other bands are completely empty, there will be a band gap between the highest level of the occupied bands and the lowest level of the unoccupied bands. Typically, a material with band gap energy greater than k_BT (T near room temperature) is an insulator. If the band gap is comparable to k_BT, it is an intrinsic semiconductor. On the other hand, if a certain number of bands is partially filled, typically metals and conductors fall in this category, the energy for the highest occupied level is called Fermi level. For each partially filled band there will be a surface in k space separating the occupied and unoccupied levels. The set of all such surfaces is known as the Fermi surface. For example, if the potential $U(\mathbf{r})$ in Eq. 1.11 equals zero, the Fermi surface in k space will become a sphere, just like for a free electron gas.

1.1.4 Surface states

The band theory discussed above is based on solving Schrödinger's Eq. 1.11 with Born-von Karman boundary condition 1.2. It is valid for bulk states because in practice the sample size is much larger than the size of a unit cell. We can assume infinite unit cells in all directions of the bulk sample. However, band structures at the sample's surface may be quite different from

that for the bulk for the following reasons.

When a solid is terminated at a certain plane, its translational symmetry is broken at that plane. Therefore, atoms at the surface of the solid may rearrange their positions to minimize their surface energy. Based on how the positions of surface atoms changed, we can categorize the changes as relaxation or reconstruction. If the entire surface plane moves as a whole in respect to the bulk planes and the relative position of all atoms in this plane is unchanged, this is called surface relaxation. Otherwise, if the two-dimensional structure of the surface plane has changed, this is called surface reconstruction. Relaxation usually does not affect the band structure in a very significant way, but reconstruction usually changes the band structure at the surface in a dramatic way. An example is shown in Figure 1.3.

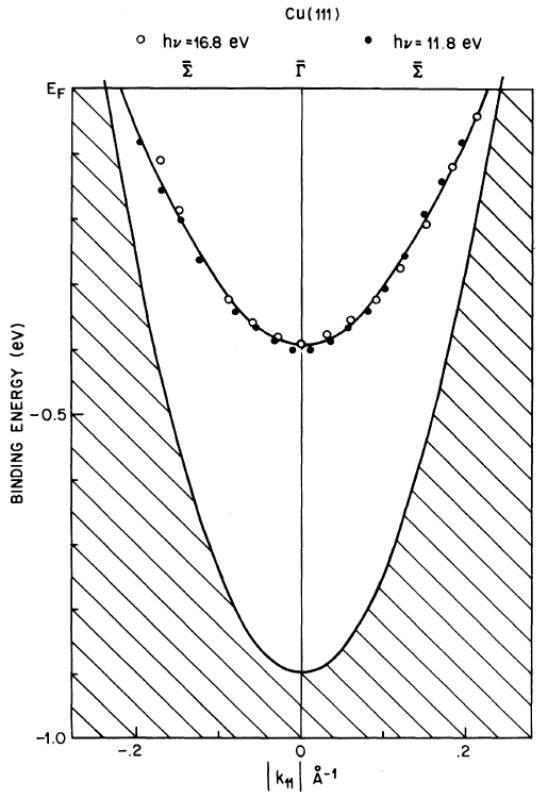

Figure 1.3 Energy dispersion relation for the Cu (111) surface state. The solid curve is a parabolic least-squares fit. The shaded region is the projected bulk continuum of states. Note, the surface state enters the bulk continuum just above the Fermi level. [1]

Surface states could also emerge even if there is no surface relaxation or reconstruction. When a material has non-trivial topology, i.e., a topological insulator, the interface between the bulk of the material and vacuum must be metallic. Its band structure is different from bulk because a vacuum can be seen as a trivial insulator. We will discuss these materials in detail in Chapter 3. ARPES measurements can calculate both bulk and surface states.

1.2 Photoemission Spectroscopy and ARPES

Photoemission spectroscopy refers to all techniques, which measure the kinetic energy of electrons exited from a given sample by monochromatic photons. It is based on the photoelectric effect observed by Hertz in 1887 [27] and explained by Einstein in 1905 [28] with a discrete energy light (photon) model:

$$E_k = hf - W, \tag{1.15}$$

where E_k is the maximum electron kinetic energy, h is Planck's constant, and f is the frequency of incident light. The term W is the work function, the minimum energy required to remove an electron from the solid sample to a point in vacuum immediately outside the solid surface. The work function for a typical metal is 4 - 5 eV, except for alkali metals that have very low work function 2 eV. The work function is a complex combination of work functions of materials lining out the chamber and the electron analyzer. To determine the value of the Fermi energy we measure the spectrum of polycrystalline gold as reference that is in good electrical contact with the rest of the system.

The energetics of the photoemission process is shown in Figure 1.4: A monochromatic beam of photons with energy hν is incident on a single crystal sample. As a result, electrons in the sample are excited and ejected into vacuum because of the photoelectric effect. Measuring the kinetic energy distribution for electrons in the vacuum allows derivation of the energy distribution or density-of-state of electrons in the solid.

By introducing the binding energy, E_B, and the conservation laws of total energy and momentum, we can relate the kinetic energy and momentum to the binding energy and crystal

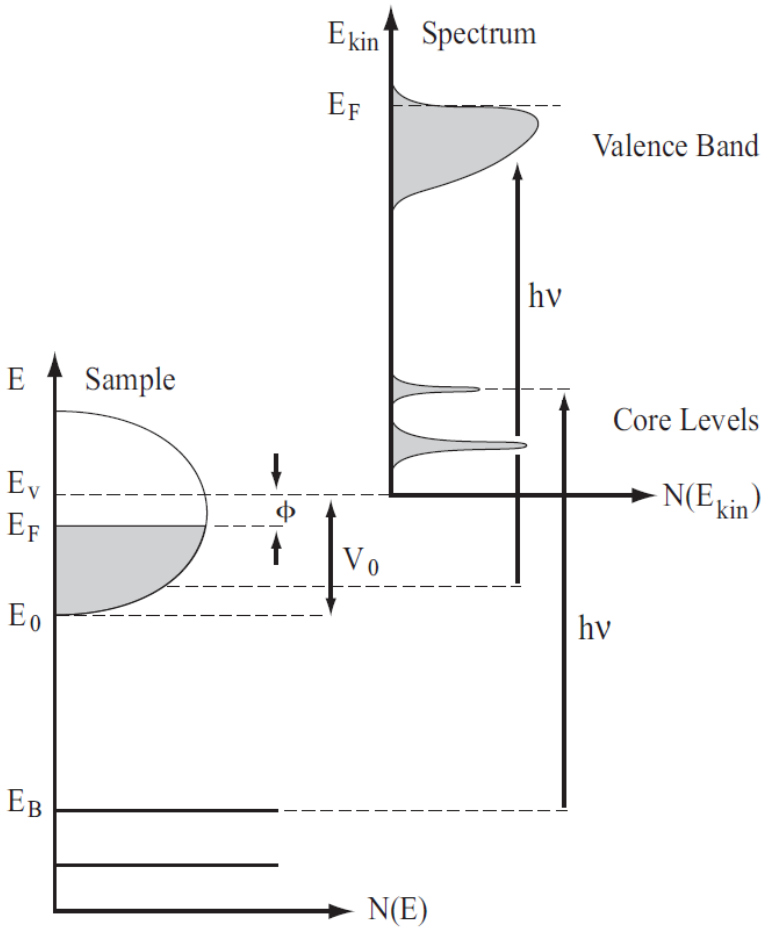

Figure 1.4 Energetics of the photoemission process. The electron energy distribution produced by incoming photons and measured as a function of the kinetic energy, E_{kin}, of the photoelectrons (right) is more conveniently expressed in terms of the binding energy, E_B (left), when one refers to the density-of-states inside the solid ($E_B = 0$ at E_F). [2]

momentum, $\hbar\mathbf{k}$, inside the solid:

$$E_{kin} = hf - W - |E_B|, \tag{1.16}$$

$$\mathbf{p}_{\|} = h\mathbf{k}_{\|} = \sqrt{2mE_{kin}} \cdot sin\theta, \tag{1.17}$$

where $\mathbf{p}_{\|}$ is the measured electron momentum parallel to the sample surface. This is equal to the component of electron momentum parallel to the crystal surface, $\hbar\mathbf{k}_{\|}$. However, the perpendicular component, $\hbar\mathbf{k}_{\perp}$, is not equal to $\mathbf{p}_{\perp}$ due to the lack of translational symmetry

along the normal direction to sample surface, $\hbar\mathbf{k}_\perp$, is not conserved when electrons cross the surface. In Eq. 1.17, the photon momentum, $\hbar\mathbf{k}_{h\nu}$, is neglected because at low photon energy, it is much smaller than that for an electron, i.e., $\hbar\mathbf{k}_{h\nu} = 0.08$ Å^{-1} at energy 1 keV, is two orders smaller than the electron momentum, $\hbar\mathbf{k}_\parallel = 1.8$ Å^{-1}, at the same energy. Equations 1.16 and 1.17 are used together to determine the binding energy, E_B, and corresponding $\hbar\mathbf{k}_\parallel$. Based on these considerations, one can determine the band structure of a solid.

1.3 Three-Step Model

In this section we will discuss the theory of photoemission. One approach is called "one-step model" as shown in Figure 1.5 b. In this model, the photoemission process is considered as single step. The electron is excited from its Bloch initial state into "time reversed LEED" state — a state composed of a free propagating component outside the crystal and a dampened portion inside the crystal. However, this model is more complex than the one more commonly used in ARPES — the three-step model, shown in Figure 1.5 a. In this model, the photoemission process is divided into three steps: (1) excitation of electrons inside the crystal, (2) transport of electrons to the surface of the crystal, and (3) escape of the electrons from the crystal to a vacuum.

To evaluate the first step, we calculate the transition probability, w_{fi}, for an electron excited from its initial state, according to Fermi's golden rule:

$$w_{fi} = \frac{2\pi}{\hbar}| < \Psi_f^N|H_{int}|\Psi_i^N > |^2\delta(E_f^N - E_i^N - h\nu), \tag{1.18}$$

where Ψ_i^N and Ψ_f^N are N-electron ground state and one possible final state, $E_i^N = E_i^{N-1} - E_B^k$ and $E_f^N = E_f^{N-1} + E_{kin}$ are the initial- and final-state energies of the N-electron system. The operator, H_{int}, represents the interaction with photons, given by

$$H_{int} = -\frac{e}{2mc}(\mathbf{A}\cdot\mathbf{p} + \mathbf{p}\cdot\mathbf{A}) = -\frac{e}{mc}\mathbf{A}\cdot\mathbf{p}, \tag{1.19}$$

where $\mathbf{p}$ is the electronic momentum operator and $\mathbf{A}$ is the electromagnetic vector potential.

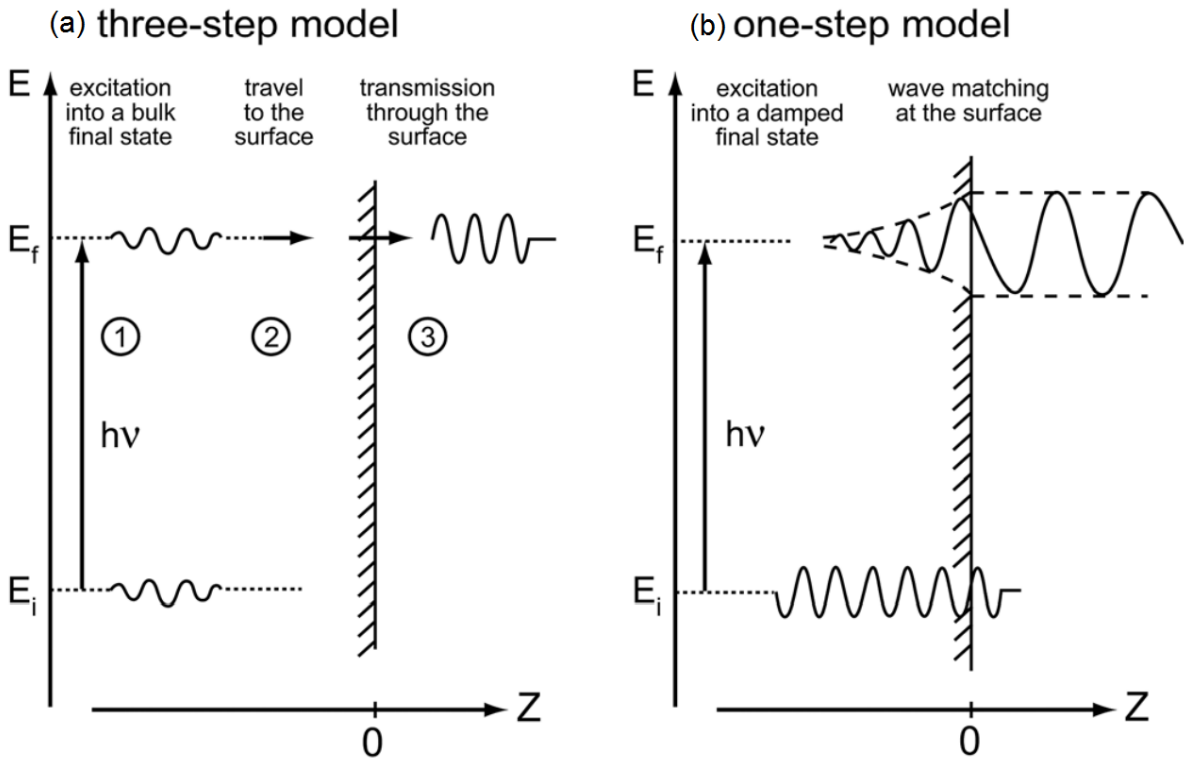

Figure 1.5 Schematic representation of (a) three-step and (b) one-step model descriptions of the photoemission process. [3]

Equation 1.18 could be simplified by introducing a "sudden approximation" assumption that the excited electron is instantaneously removed with no interaction with the system after excitation. In other words, effective potential of the system changes discontinuously at the moment of Step 3. The sudden approximation is not appropriate at low photon energies, where the photoelectrons need more time to escape from the sample's surface than the system relaxation time. In this situation, the interaction between photoelectron and photohole must be taken into account.

Under sudden approximation, we can factorize the N-particle state as:

$$\Psi^N = \mathcal{A}\phi^k\Psi^{N-1}, \tag{1.20}$$

where $\mathcal{A}$ is a Fermionic antisymmetric operator to ensure the N-electron system satisfies the Pauli principle, ϕ^k is the wave function of the photoelectron, and Φ^{N-1} is the N - 1 particle state

wave function. The N - 1 particle final state can be expressed as a sum of excited eigenstates, Ψ_m^{N-1}, Thus, the matrix element in Eq. 1.18 can be written as:

$$< \Psi_f^N | H_{int} | \Psi_i^N > = < \phi_f^k | H_{int} | \phi_i^k > < \Psi_m^{N-1} | \Psi_i^{N-1} >, \tag{1.21}$$

where $< \phi_f^k | H_{int} | \phi_i^k > \equiv M_{f,i}^k$ is the dipole matrix element for photon-electron interaction, and $< \Psi_m^{N-1} | \Psi_i^{N-1} > \equiv |c_{m,i}|^2$ is the probability that the state Ψ_m^{N-1} is left behind after one electron is removed. Therefore, the total photoemission intensity is proportional to

$$\sum_{f,i} |M_{f,i}^k|^2 \sum_m |c_{m,i}|^2 \delta(E_{kin} + E_m^{N-1} - E_i^N - h\nu), \tag{1.22}$$

In a noninteracting electron system, $|c_{m,i}|^2$ is unity at a single m and zero everywhere else. If $|M_{f,i}^k|^2$ does not equal zero, the spectral function will consist of a series of delta functions at a given momentum and energy as shown in Figure 1.6 b. In a Fermi-liquid system, or strongly correlated systems, many of the $|c_{m,i}|^2$ will be non-zero. This is a more realistic situation. In this case, the ARPES spectra will consist of a main line and several satellites instead of single delta functions, as shown in Figure 1.6 c. An example of such situation would be the photoemission from gaseous molecular hydrogen as shown in Figure 1.6 c. Many peaks separated by a few tenths of meV would be observed in such a case. They correspond to the excitations of different vibrational states of the H_2^+ molecule. In the case of a solid hydrogen, the spectra (dashed line) becomes a broad continuum with a sharp peak corresponding to a fundamental transition from H_2 ground state to H_2^+ molecule.

Step two of the three-step model is the transportation of excited electrons to the sample's surface. When the electron travels within the sample, it could be scattered mostly by the lattice. Such scattering could be either elastic or inelastic. In inelastic case, the secondary electrons will be produced and added to the background at higher binding energies. They do not carry any important information and the measured data can be normalized to remove this background [29].

The excited electron cannot penetrate any significant thickness of the sample. Instead, it is expected to only go through a thickness equal to its mean free path. Mean free path of an

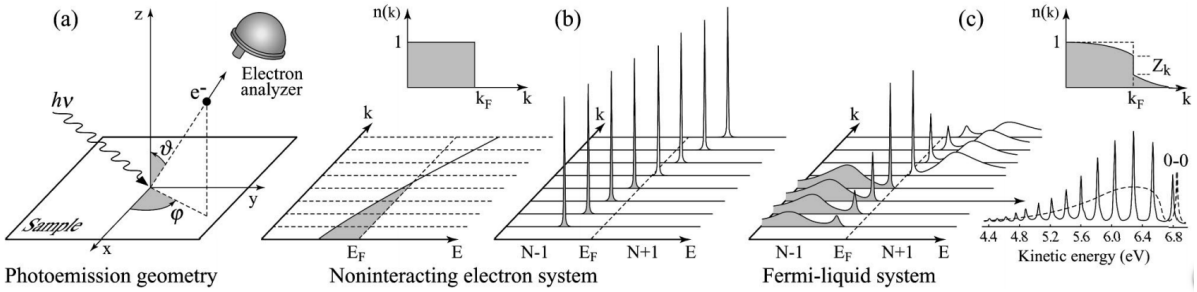

Figure 1.6 Angle-resolved photoemission spectroscopy: (a) geometry of an ARPES experiment in which the emission direction of the photoelectron is specified by the polar (θ) and azimuthal (ϕ) angles; (b) momentum-resolved one-electron removal and addition spectra for a noninteracting electron system with a single energy band dispersing across EF; (c) the same spectra for an interacting Fermi-liquid system. For both noninteracting and interacting systems the corresponding groundstate (T = 0 K) momentum distribution function n($\mathbf{k}$) is also shown. (c) Lower right, photoelectron spectrum of gaseous hydrogen and the ARPES spectrum of solid hydrogen developed from the gaseous one. [2]

electron depends on its energy as shown in Figure 1.7. The minimum value of mean free path occurs at 50 eV. The photon energy of our helium lamp ARPES system is 21.2 eV and for our laser ARPES system is about 6.7 eV. At this energy, the mean free path is ~ 3.3 nanometers, which means we are probing the top several layers of the sample. According to Figure 1.7, the laser ARPES (6.7 eV) has better bulk sensitivity than the helium lamp system (21.2 eV).

1.4 Single-particle Spectral Function

To obtain the value of $|c_{m,i}|^2$ in Eq. 1.22 for the Fermi liquid (interacting) case, the most common approach is to introduce a time-dependent correlation function, $\mathcal{G}(t-t')$, which describes the possibility amplitude for propagation of an electron in the many-body system. Initially, the system is at a Bloch state with momentum $\mathbf{k}$. At a time interval $|t-t'|$ after an electron is added to the system, the system is still in the same state. The Fourier transformation for $\mathcal{G}(t-t')$ is the sum of $G^+(\mathbf{k},\omega)$ and $G^-(\mathbf{k},\omega)$, defined as the one-electron addition, removal of Green's function.

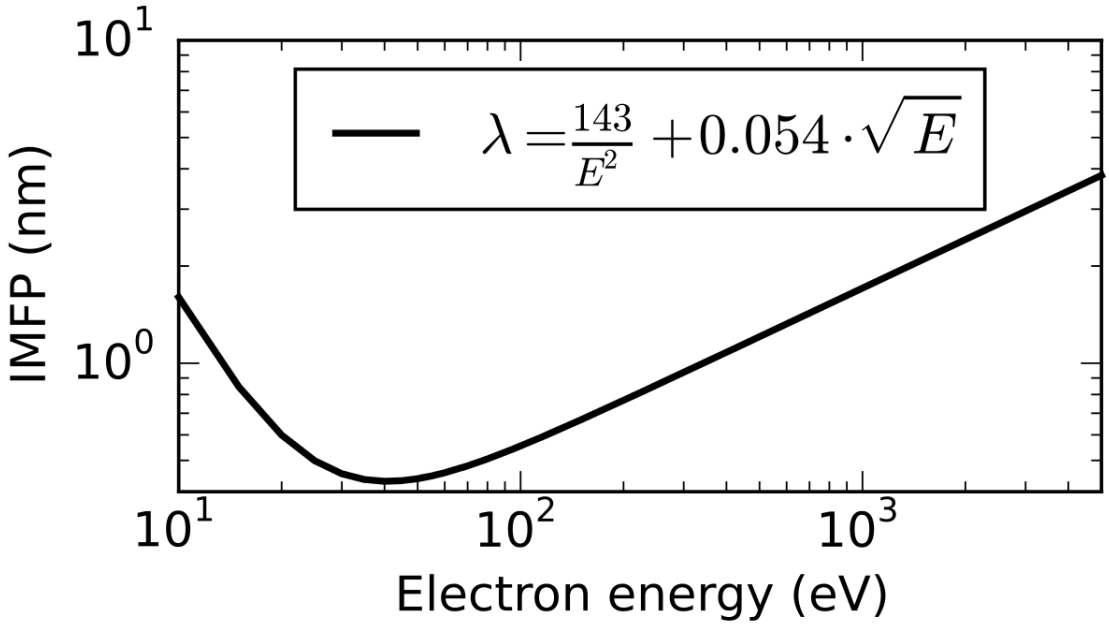

Figure 1.7 Universal Curve - Mean free path of electrons in solids as a function of their energy. [4]

$$G^{\pm}(\mathbf{k},\omega) = \sum_m \frac{|<\Psi_m^{N\pm1}|c_{\mathbf{k}}^{\pm}|\Psi_i^N>|^2}{\omega - E_m^{N\pm1} + E_i^N \pm i\eta}, \tag{1.23}$$

where $c_{\mathbf{k}}^{\pm}$ are the creation and annihilation operators, respectively, and η is a positive infinitesimal number. With $\eta \to 0^+$, we can obtain the single-particle spectral function, $A(\mathbf{k},\omega) = A^+(\mathbf{k},\omega) + A^-(\mathbf{k},\omega) = -(1/\pi)ImG(\mathbf{k},\omega)$, with

$$A^{\pm}(\mathbf{k},\omega) = \sum_m |<\Psi_m^{N\pm1}|c_{\mathbf{k}}^{\pm}|\Psi_i^N>|^2, \tag{1.24}$$

where $G(\mathbf{k},\omega) = G^+(\mathbf{k},\omega) + [G^-(\mathbf{k},\omega)]^*$ is the retarded Green's function. By comparing Eqs. 1.24 and 1.22 we see that the total intensity measured by ARPES is the product of the matrix element and single particle spectral function: $I(\mathbf{k},\omega) \propto \sum_{f,i} |M_{f,i}^k|^2 A^-(\mathbf{k},\omega)$. Considering that ARPES is probing only the occupied electronic states, Fermi distribution function $f(\omega)$ is introduced:

$$I(\mathbf{k},\omega) \propto \sum_{f,i} |M^k_{f,i}|^2 f(\omega) A^-(\mathbf{k},\omega). \tag{1.25}$$

Therefore, the imaginary part of the retarded Green's function $G(\mathbf{k},\omega)$ can be directly determined from the ARPES spectrum. The real part of $G(\mathbf{k},\omega)$ can be calculated from the imaginary part by using Kramers-Kronig relations.

If we take the electron-electron correlation into account, the Green's function and one-particle spectral function must be corrected as

$$G(\mathbf{k},\omega) = \frac{1}{\omega - \epsilon_k - \sum(\mathbf{k},\omega)}, \tag{1.26}$$

$$A(\mathbf{k},\omega) = -\frac{1}{\pi} \frac{\sum''(\mathbf{k},\omega)}{[\omega - \epsilon_k - \sum'(\mathbf{k},\omega)]^2 + [\sum''(\mathbf{k},\omega)]^2}, \tag{1.27}$$

where $\sum(\mathbf{k},\omega) = \sum'(\mathbf{k},\omega) + i\sum''(\mathbf{k},\omega)$ is called the electron self-energy. Its real and imaginary parts contains all the information about electron energy renormalization and lifetime. In principle, self energy can be extracted from the experiment and modeled theoretically [30, 31]. However, the exact calculation of self energy and $A(\mathbf{k},\omega)$ is very difficult. For the purpose of this dissertation, we will assume that the shape of $A(\mathbf{k},\omega)$ for a fixed w has a lineshape of a Lorentzian.

1.5 Matrix Elements

As shown in Eq. 1.25 the ARPES signal intensity is proportional to the one-particle spectral function $A(\mathbf{k},\omega)$. It is also proportional to the term $|M^k_{f,i}|^2$, which depends on the interaction between the electrons and the incoming photons. This matrix element term also depends on the experimental geometry with respect to the sample orientation, and may result in suppression of the ARPES intensity. For example, in cuprates, the Cu^{2+} has a $d_{x^2-y^2}$ atomic orbital and O^{2-} has p_x, p_y atomic orbitals. The $d_{x^2-y^2}$ orbital is even with respect to the mirror plane as shown in Figure 1.8 a. It is odd with respect to a plane rotated 45 ° from mirror plane in z direction. To have a non-zero intensity detected at the electron analyzer located at the mirror plane, the matrix element $|M^k_{f,i}|^2 =< \phi^k_f|\mathbf{A}\cdot\mathbf{p}|\phi^k_i >$ must be an even function with respect to

the mirror plane. First, the final state $< \phi_f^k|$ must be even because if it is odd, it will equal zero at the mirror plane, where the electron analyzer is located. Therefore, the reminder of the matrix element, $\mathbf{A} \cdot \mathbf{p}|\phi_i^k >$, must also be even. We summarize the polarization conditions for an even matrix element as:

$$< \phi_f^k|\mathbf{A} \cdot \mathbf{p}|\phi_i^k > \left\{ \begin{array}{c} \phi_i^k even < +| + |+ > \Rightarrow \mathbf{A} \text{ even} \\ \phi_i^k odd < +| - |- > \Rightarrow \mathbf{A} \text{ odd} \end{array} \right\}, \tag{1.28}$$

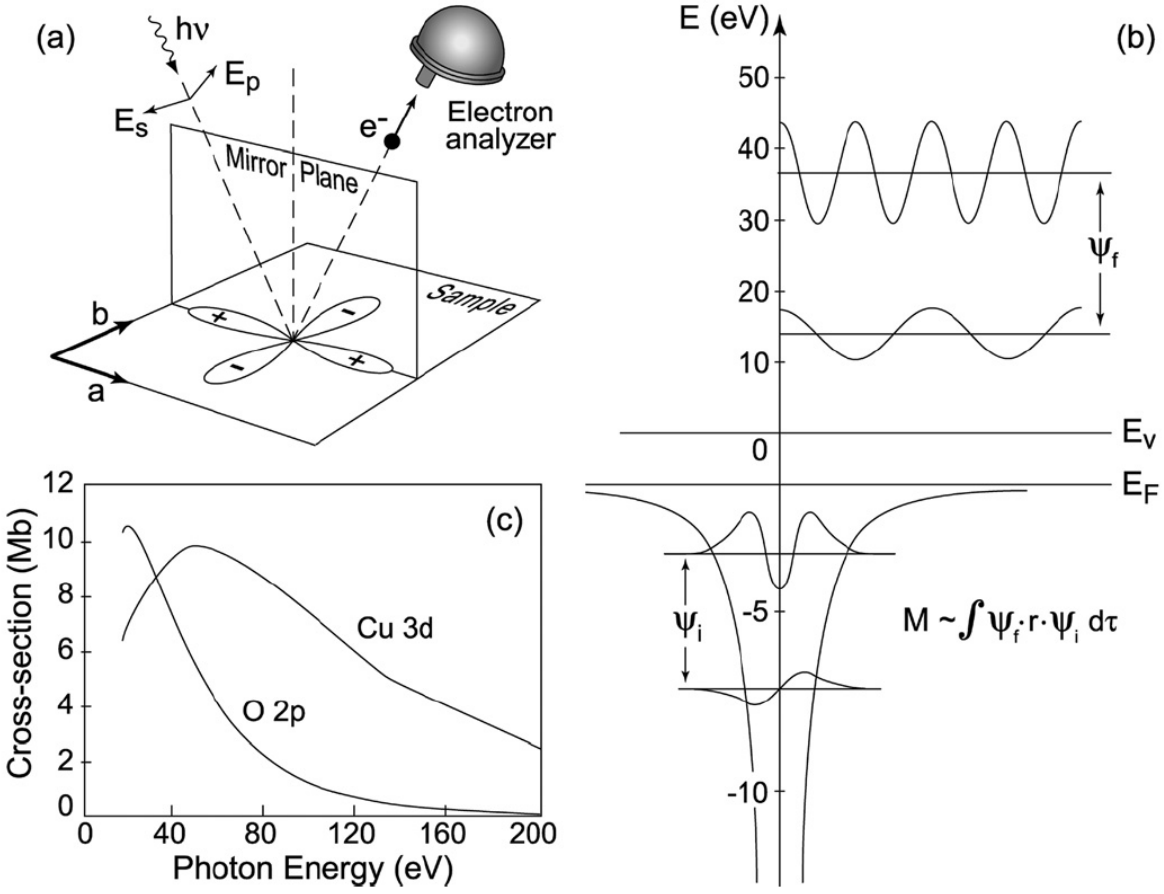

Figure 1.8 (a) Mirror plane emission from a $d_{x^2-y^2}$ orbital. (b) Sketch of the optical transition between atomic orbitals with different angular momenta (the harmonic oscillator wavefunctions are here used for simplicity) and free electron wavefunctions with different kinetic energies. (c) Calculated photon energy dependence of the photoionization crosssections for Cu 3d and O 2p atomic levels. [2]

Consider a plane wave $e^{i\mathbf{kr}}$ for the final state of an electron at the analyzer, the matrix element $< \phi_f^k|\mathbf{A}\cdot\mathbf{p}|\phi_i^k >$ will be proportional to $|(\epsilon\cdot\mathbf{k}) < \phi_i^k|e^{i\mathbf{kr}} > |^2$, where ϵ is a unit vector along the direction of $\mathbf{A}$. The next term $< \phi_i^k|e^{i\mathbf{kr}} >$ depends on ϕ_i^k and $e^{i\mathbf{kr}}$, which are the initial state wave function and wavelength of the outgoing plane wave as shown in Figure 1.8 b. Figure 1.8 c shows the variation of the cross-section of Cu 3d and O 2p orbits as a function of photon energy. Larger photon energy will provide larger photoelectron momentum and kinetic energy, and thus change the cross-section. The cross-sections have a maximum at 20 and 50 eV for O 2p and Cu 3d, respectively. Beyond 120 eV, the cross-section of O 2p becomes very small. It is very challenging to perform ARPES measurements for an atomic orbital with a very small cross-section. Therefore, we need to carefully choose the incident photon energy.

1.6 Experimental Setup

A simple ARPES spectrometer is sketched in Figures 1.6 a and 1.8 a. The spectrometer consists of three major components: (1) light source (which emits photons with energy $h\nu$), (2) vacuum chamber (in which the sample is placed) and (3) electron analyzer. We have two sets of ARPES spectrometers that differ mostly in photon source type. Next, we discuss the photon sources.

1.6.1 Photon sources

There are two photon sources in our lab — helium discharge lamp and tunable vacuum UV (VUV) laser. They provide photons of different energies, and have different energy resolutions. According to equation 1.17, the minimum momentum we could measure is 0 while the maximum momentum depends on the energy of the incoming photons and the angle θ. Since the maximum angle θ in the experiment is fixed, the momentum range we could measure depends mostly on the energy of incoming photons. Therefore, for a given range of angle θ and the same angular step $\Delta\theta$, lower photon energy gives us a smaller momentum range and a higher momentum resolution.

The helium discharge lamp produces VUV photons from He electron cyclotron resonance (ECR) plasma. In operation, the low pressure (< mTorr) gas is ionized in a cavity placed

in a magnetic field by microwave radiation. Some electrons in the gas atoms will be excited by collision to higher energy level. When the electrons transition back to lower energy level, they emit photons with energy equal to the energy difference of the two atomic levels. If the pressure is high (∼1 bar), the collisions between excited ionized gases will distort the energy levels and broaden the spectrum line. Therefore, high pressure discharge lamps can produce a continuous spectrum of photons and it is widely used for street lighting, artificial photoassimilation for growing plants, etc [32]. In our experiment, we use a low pressure helium discharge lamp. Our He discharge lamp emits photons with three main energies: 21.2, 23.1 and 40.8 eV. Approximately eighty percent of the total intensity is due to the He Iα emission line. The remainder are the He Iβ and He IIα emission lines. Each contributes ∼10% of the total intensity. A total UV flux of 2×10^{16} photons / (sr·s) can be obtained. For some of the studies, we use He Iα line to measure for example the electronic structure of graphene on SiC substrate. As we will see later, there are some background signals, due to the He IIα and He Iβ emission lines. However, the spectra from these lines do not overlap with those from the He Iα line. Therefore, it is sufficient to apply the light produced by our He discharge lamp on the sample without a monochromator. The beam size can be focused to $\sim 1mm^2$ on sample.

The other photon source is a tunable VUV laser. This consists of a green pump laser, a Ti:Sapphire laser, and a conversion box as shown in Figure 1.9. The oscillator in Ti:Sapphire laser is pumped by an 18 W continuous wave Verdi laser at 532 nm. The wavelength of photons generated by the Ti:Sapphire laser can be tuned from 710 to 920 nm. This corresponds to a range of photon energies 1.35 - 1.75 eV, lower than the work function of a typical sample (∼4.3 eV). Therefore, we use a conversion box to quadruple the photon energy to 5.4–7 eV (177.5–205 nm) range. There is a series of optical devices inside the conversion box, including a standard barium borate (BBO) crystal to double the frequency of the incoming laser IR beam and a potassium beryllium fluoroborate (KBBF) crystal to double this frequency again. The power of the laser when it hits the sample is close to 1 mW at 205 nm and more than 20 μW at 177.5 nm. The photon flux is more than enough for our ARPES measurements because the beam consists of more than 10^{15} photons/s which is much higher than ones available at best synchrotrons.

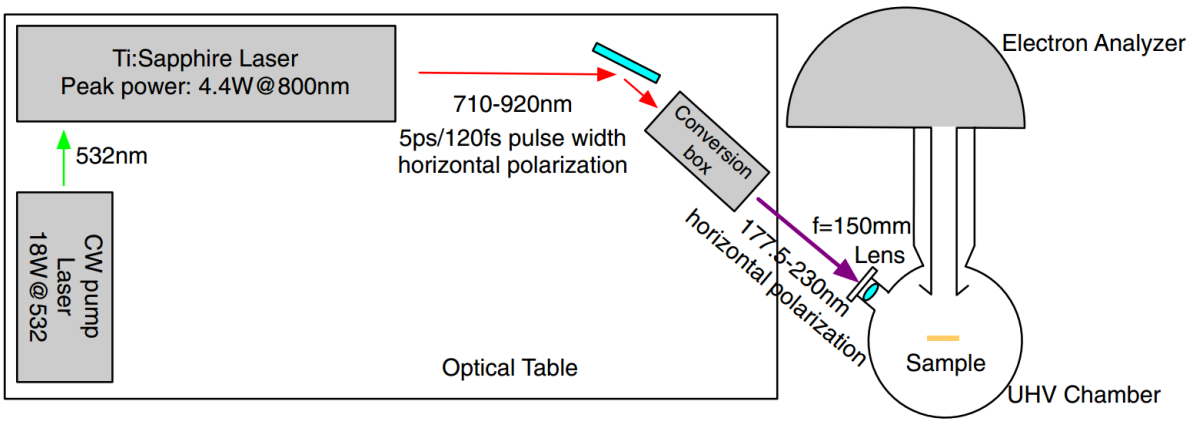

Figure 1.9 Layout of the tunable laser ARPES system. The pump laser, Ti:Sapphire oscillator, and FHG conversion box are mounted on a 12 in. non-magnetic optical table. The electron analyzer and measurement chamber are mounted on an aluminum extrusion frame connected to the optical table.

Table 1.1 Photon source comparison.

	Ti:Sapphire Laser	Helium Lamp
Intensity (photons / s)	10^{15}	10^{13}
Energy resolution (meV)	< 1	8
Spot diameter (μm)	1 - 30	1000
Momentum resolution (Å^{-1})	10^{-3}	10^{-2}
Time resolved	100 fs - ps	none
Polarization	easy to change	unpolarized
Bulk sensitivity (layers)	10 - 100	5
Photon energy	small range	fixed
Momentum range	partial BZ	2 BZ

Table 1.1 summarizes the properties for the Ti:Sapphire laser and helium Lamp. The data measured from the Ti:Sapphire laser usually has better energy and momentum resolution. Also, since the spot size of the Ti:Sapphire laser is smaller, it can measure very small samples. The advantage of the helium lamp system is its large momentum measurement range. Most of the time, the sample has lattice constant in the range of several angstroms, the helium lamp system can measure the whole Brillouin zone in a single scan, while the laser system must perform multiple scans to obtain the sample's band structure in the first Brillouin zone.

1.6.2 Vacuum chamber

The vacuum chamber is used for keeping the sample in an ultrahigh vacuum and shielding any external magnetic field. A simplified sketch of ultra high vacuum (UHV) chamber is shown in Figure 1.9 as a sphere containing the sample. There are two main reasons for keeping the sample in a ultra high vacuum during the measurement process. First, photoelectrons coming from the sample must be able to travel to the electron detector at the end of the semi-sphere electron analyzer without scattering. The mean free path of an electron is inversely proportional to the collision cross-section and pressure. To make the electron mean free path greater than the distance between sample and electron collector ($\sim$2m), a vacuum smaller than $\sim 10^{-4}$ torr is required. Second, since ARPES measures the electronic structure of only the top few layers of a sample, the sample surface must be atomically clean — not covered with gas molecules. At lower pressure, there are fewer gas molecules moving toward the sample's surface, thus the sample's surface will be covered with gas molecules much slower compare to the samples in high pressure environment. When the entire sample's surface is covered with a layer of gas molecules, the ARPES signal will primely consist of the signal from the top layer of gas molecules instead of the sample itself. To ensure the sample will remain useful for several days to complete a measurement, the vacuum must be ultra high — of the order of 10^{-11} torr.

The magnetic field is shielded to prevent alternations of the photoelectron trajectories by Lorentz force. Even a magnetic field as weak as the earth's field will significantly distort the ARPES spectrum. To shield the external magnetic field, a layer of mu-metal is added to the vacuum chamber's stainless steel wall. Mu-metal is a soft magnetic alloy of iron and nickel that has very high permeability suitable for shielding sensitive electronic equipment against static or low-frequency magnetic fields [33]. Since mu-metal does not cover chamber windows and ports mostly located along the main-chamber-electron-analyzer direction, the orientation of the main chamber and electron analyzer are along east-west direction, perpendicular to the earth's north-south magnetic field. Even the residual magnetisation of the mumetal shield must be eliminated. A straight thick copper wire is run through the chamber and the analyzer with AC current $\sim$600 A that generates the AC magnetic field. By very slowly decreasing the current

to zero, the mu-metal shield is cycled through smaller and smaller hysteresis loop, reducing residual magnetization. After orienting the main chamber and demagnetization, we measure the field with a magnetic meter to make sure that the magnetic fields are less than 3 mGauss in the sample-lens area.

1.6.3 Electron analyzer

To record the number of photoelectrons at a specific energy and momentum, an electron analyzer is connected to the main chamber and collects the photoelectrons coming from the sample. The laser-based ARPES system uses an R8000 electron analyzer, while the He-lamp ARPES system uses an R2002 electron analyzer supplied by VG Scienta. They are different in some parameters, (i.e. lens, slit, pass energy, etc.), yet, their working principles are the same. First they sort the photoelectrons by momentum with a series of electrostatic lenses. Next they sort the electrons with the same momentum by the use of a hemispherical capacitor. Such "sorted" photoelectrons are then detected as 2D detector array by using multichannel electron multiplied plates, phosphorus screen and CCD camera.

The electrostatic lens is located in the tube between UHV chamber and electron analyzer hemisphere as shown in Figure 1.9. Figure 1.10 a shows an electron ray diagram in the lens tube. The sample is at (0, 0) mm. Photoelectrons are emitted from different positions (represented by different rays of the same color) on the sample's surface with different emission angle (or momentum, represented by different colors). Photoelectrons with the same emission angle are focused to the same position on the slit at the entrance of the electron analyzer, regardless the position on the sample's surface where they come from. This is better shown in a zoom in Figure of 1.10 b. Figure 1.10 c shows the image we obtained from the electron detector for the rays shown in Figure 1.10 a. The maximum emission angle for a lens to collect the photoelectrons depends on the setting of the electron analyzer. It could be from $\pm 7^\circ$ to $\pm 40^\circ$. Larger acceptance angles require a larger lens aperture and closer distance between the sample and lens.

At the entrance of the hemisphere capacitor, there is a rectangular slit with a fixed length, which determines the maximum k-range. The width of the slit can be changed between 100–800

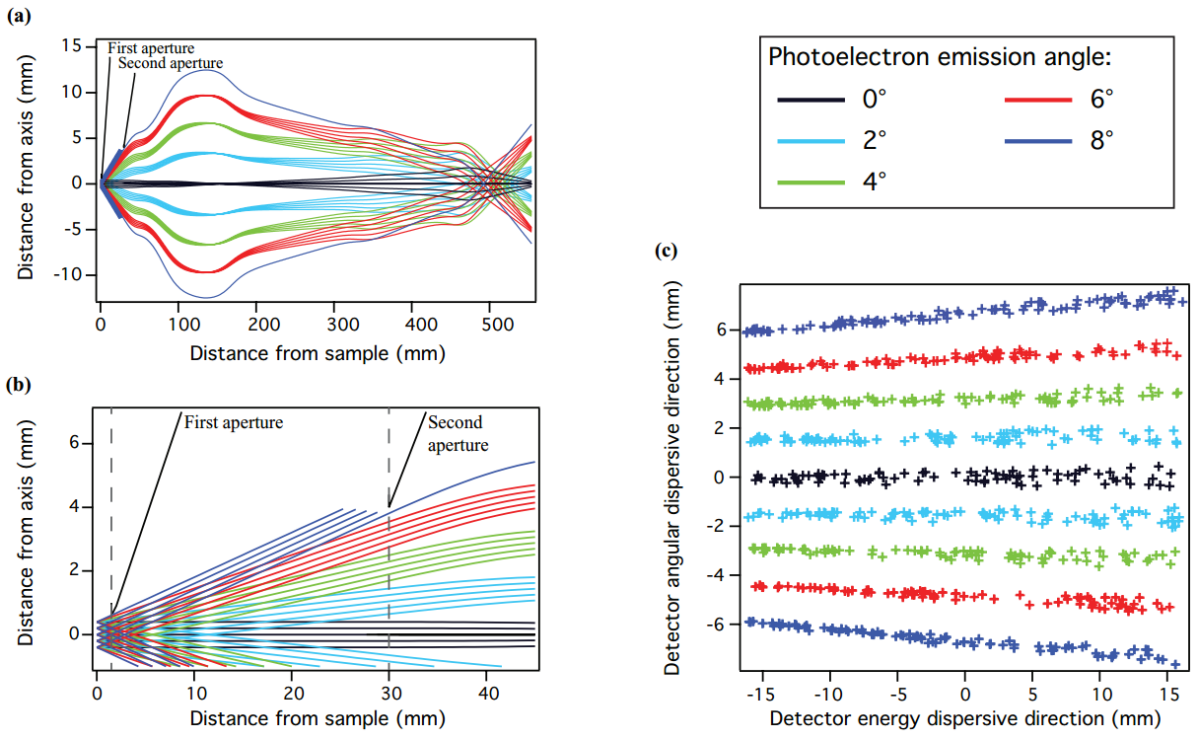

Figure 1.10 (a) Electron ray-tracing calculations. (b) Zoomed view of the electron trajectories shown in (a). The corresponding simulated detector image is shown in (c). At the center of this axis, electrons emitted along the electrostatic lens axis are detected. [5]

μm. Larger widths result in larger electron intensity, but lower lateral momentum resolutions. After passing through the slit, electrons enter the hemispherical analyzer, as shown in Figure 1.11. A voltage, V_B is applied to the outer hemisphere, while voltage, V_A, is applied to the inner hemisphere. The electric field between these two hemispheres will deflect electrons. Electrons with lower energy will be deflected more, so electrons with different energies will strike different positions in the radial direction of the hemisphere. Electrons will hit the inner hemisphere before being detected, if their energy is too small. If their energy is too large, they will hit the outer hemisphere before detection. The energy, E_0, of an electron following the center trajectory (Figure 1.11) is called pass energy. By altering the voltages of inner and outer hemispheres, the pass energy can be changed. The energy range detected by the electron detector is $\sim$7% of the pass energy. For example, pass energy for 5 eV allows detection of

electrons with energy between 4.84 and 5.16 eV. Thus, the energy range is 0.32 eV, 6.4 % of 5 eV. Since the size of electron detector is fixed, smaller pass energy will a have higher energy resolution.

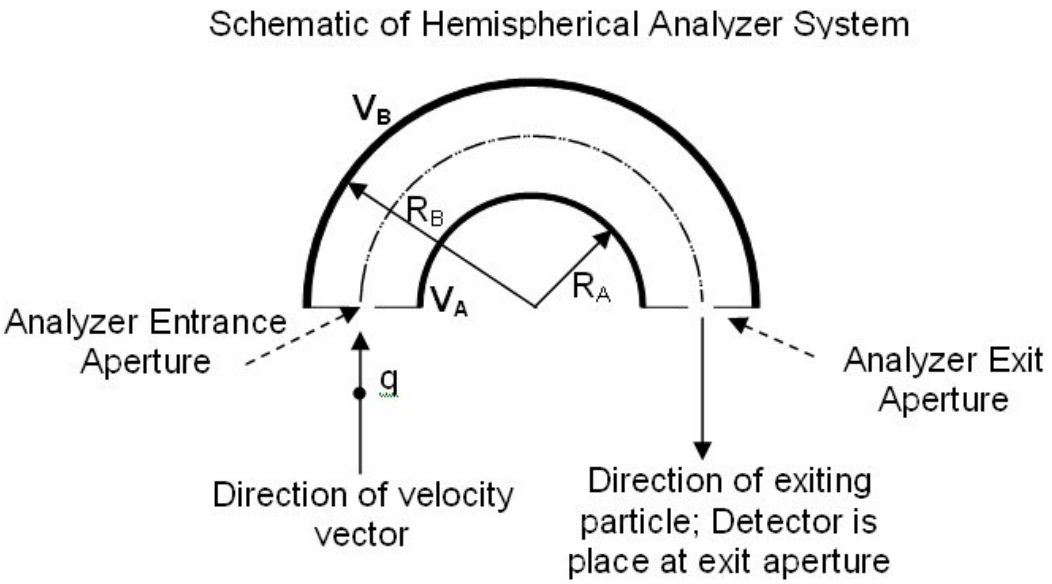

Figure 1.11 The hemispherical analyzer.

The final destination for the photoelectrons is a 2D micro-channel plate (MCP) detector located at the end of the hemisphere. A micro-channel plate is a slab made from highly resistive materials with a regular array of tiny tubes or slots (microchannels) leading from one face to the opposite face, densely distributed over the entire surface. Each microchannel is a continuous-dynode electron multiplier, where the multiplication takes place under the presence of a strong electric field [34]. After passing through the MCP, electrons strike a florescent phosphor screen and a high-speed CCD camera collects the images as raw ARPES data.

1.6.4 Sample preparation

As discussed earlier in this section, photons with lower energy have a higher energy resolution. However, we cannot go to an arbitrary small photon energy because the incident photon

energy must be greater than the work function for the sample (Eq. 1.16). Otherwise, there will be no electrons excited from the sample surface. Another major disadvantage of using low energy photons is the large penetration depth of the photons. According to the Beer-Lambert law, the intensity of an electromagnetic wave traveling inside a material falls exponentially by

$$I(z) = I_0 e^{-\frac{z}{\delta}}, \tag{1.29}$$

where δ is the penetration depth. δ is high for Low energy photons. Thus for low energy beam, its intensity is more equally distributed between sample surface and hundreds of nanometers into the surface. However, based on Figure 1.7 the mean free path for photoelectrons of energy 20 - 100 eV is approximately 5 Å[4]. The energy of ARPES photoelectrons in our experiments is typically below 20 eV. Therefore, the mean free path of our photoelectrons is less than 20 Å, which means we are only detecting the electron signal from the topmost layer. Therefore, most of the intensity of low energy photons gets lost.

To obtain the ARPES signal, we need to carefully prepare the sample so there is a fresh, flat sample surface present that can emit photoelectrons without additional scattering. The most common method to achieve this is to cleave the sample inside the vacuum chamber as shown in Figure 1.12. First, we glue the sample to the sample holder. Next, we glue a metal bar on top of the sample and transfer the whole holder into the ultrahigh vacuum chamber. Finally, use a rod (transfer arm) to knock the metal bar from the sample holder. This should cause the sample to break. The part connected to the metal bar falls into the main chamber and the other part remains on sample holder, hopefully with a fresh, flat surface ready for measurement.

To ensure the sample is in good electric contact with the sample holder, one use conductive epoxies (e.g. the EPO-TEK H21D silver epoxy) or add a layer of graphite that electrically connects the sample with the holder. Note, this cleaving method does not always provide a nice, flat surface. Sometimes the cleaved surface is not flat, sometimes the entire sample is gone with the metal bar. Other times, the entire sample and layers of epoxy on top remain on the sample holder after cleaving. Unfortunately in these uncontrollable cases no effective measurements are possible. Instead, we must remove the sample holder from the main chamber

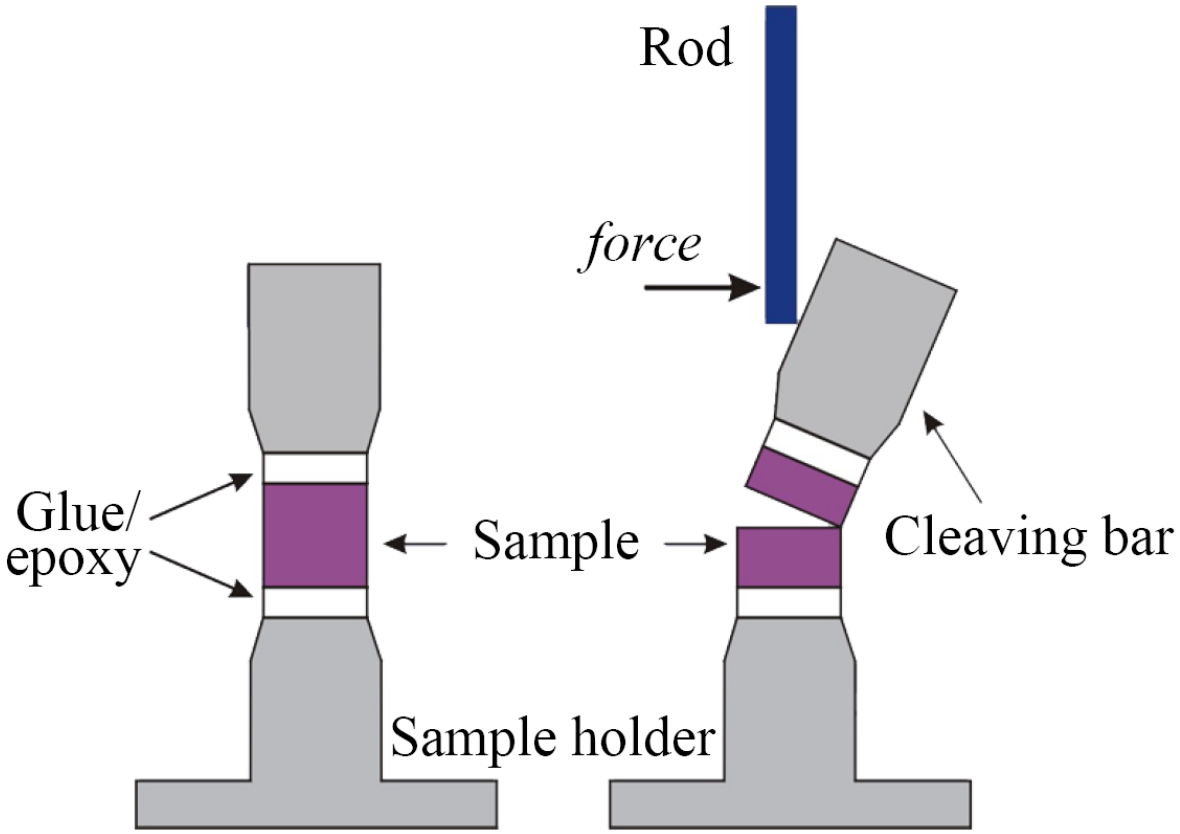

Figure 1.12 Process of sample cleaving. A cleaving bar is attached to the sample before being loaded into the vacuum chamber. Next, it is removed mechanically inside the vacuum chamber. [6]

and repeat the entire preparation process.

Another method to prepare the sample is to polish it in air before transferring it into the vacuum chamber. Since no metal bar is used to glue the sample, there will be a layer of air molecules on top of the sample when it is inside the vacuum chamber. To remove the molecule layer, we use annealing and sputtering. After several minutes, the air molecule layer on the sample leaves the surface so a clean sample surface remains. This method is not applicable for small samples, because the current must be applied to an approximately 10 mm long by 1 mm wide stripe.

CHAPTER 2. SCHWARZSCHILD OBJECTIVE

2.1 Introduction

An ideal ARPES sample should be a conductive single crystal, is a $\sim$1 mm^2 and atomically flat with a clean surface. When a beam of monochromatic photons is used for "ideal" sample, the size of beam spot does not affect data quality. However, only a few samples are ideal or close to ideal in practice. For most samples, it is very helpful to focus the light to an area as small as possible and there are many benefits of that.

First, a small spot size provides an ability to measure small samples. It is usually not simple to grow large single crystals in the laboratory, especially a single crystal from novel materials, such as superconductors, topological insulators, and Dirac materials. If the spot size is too large compared with the size of the sample, there could be two problems. First, the light intensity (in unit of photons per second) on the sample is small. Only less than 0.5% of the light from IR laser in Figure 1.9 is converted to VUV and incident on the sample, exciting the electrons. Since the conversion box already reduces the power of light from the Ti:Sapphire laser by a factor of 1000, it is a great power loss. Second, the portion of light that does not hit the sample produces a background signal that interferences with data collection. This is worse than the first problem, because we could still obtain high quality data by increasing the laser's power and the measuring time. While for this second problem, there is no easy way to obtain good data.

A second benefit is the small spot size provides the ability to study single grains in polycrystalline samples. Figure 2.1 shows a microscopic image of $NdFeAsO_{(1-x)}F_x$ polycrystal. This polycrystal is about 1 cm^2 large and consists of many single crystal grains (shown in different colors) about 100 $\times$ 100 μm^2 in size. Since the single crystal grains are not oriented in the

same direction, their band structures will be different. The helium lamp has a circular light spot $\sim$ 1 mm in diameter. If we measure this sample with the helium lamp ARPES system, we will obtain the superposition of band structures for all the different single crystal domains. This is similar to the second problem, and one cannot obtain momentum resolved data this way. On the other hand, if we measure the sample with a laser ARPES system, which has a light spot diameter $\sim 30\mu$m, we are able to focus the light on one single crystal. Therefore, we can measure band structure of each single crystal separately.

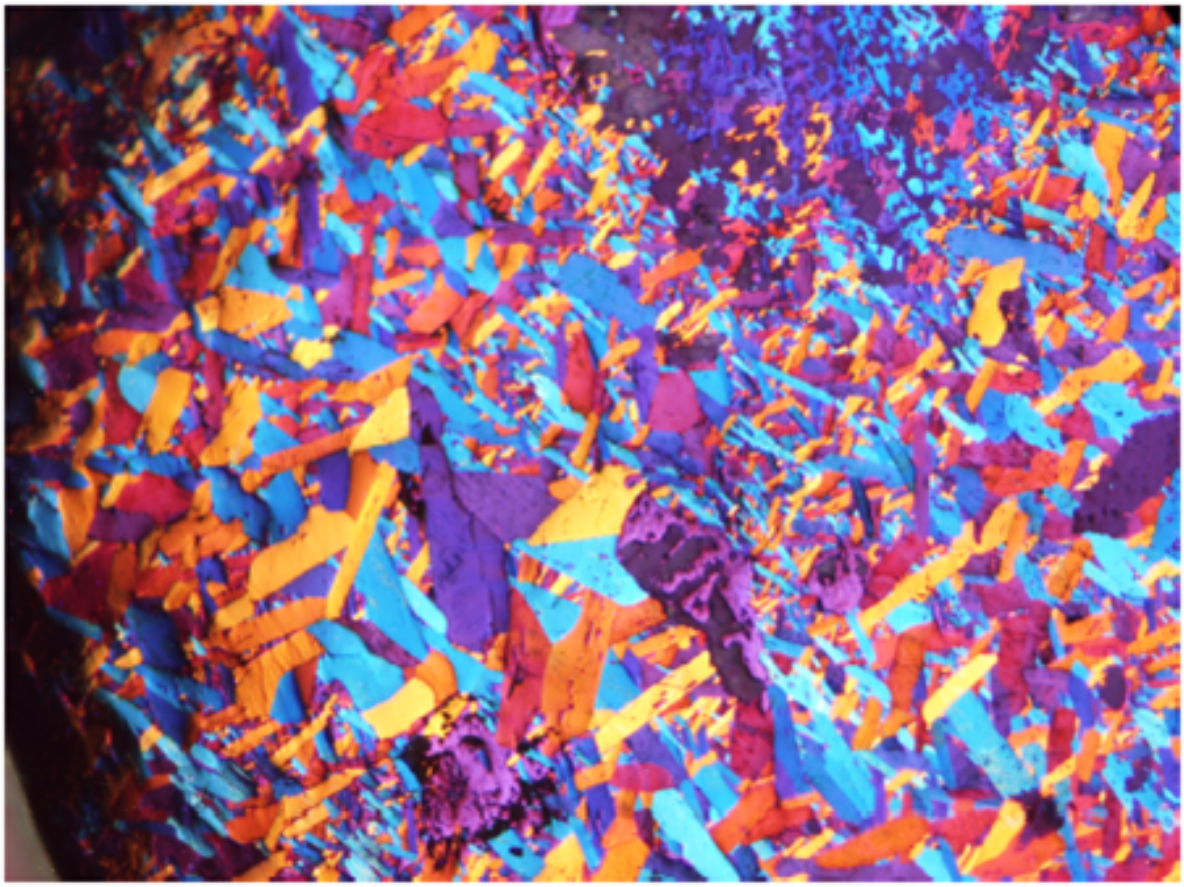

Figure 2.1 "Large" grain sample of $NdFeAsO_{(1-x)}F_x$. The image scale is $\sim 1mm^2$ and the size of each grain is $\sim$100 $\times$ 100 μm^2

Third, a small spot size provides an ability to measure samples with a rough, but clean, surface. For a flat sample surface, we can rotate the sample to measure band structure at different angles or positions in the Brillouin zone. However, for a sample that is not flat, there

are many tiny planes on its surface oriented at different angles. If the light spot size covers all these tiny planes, the band structures of different angles will be superimposed. Also, it is impossible to revert the superposition process to obtain the band structure of a single tiny plane.

Finally, a small spot size provides the ability to study the sample's intrinsic and extrinsic inhomogeneities. For example, the unit cell of the high temperature superconductor, $YBa_2Cu_4O_8$, consists of two layers of Cu_2O chains, one layer of BaO, and two layers of Cu_2O planes (See Figure 2.2). Cleaving could occur at the surface of Cu_2O chains or the surface of Cu_2O planes. Because ARPES is very sensitive to the sample's surface, these two terminations have very different surface states, as shown in the ARPES data in Figure 2.3. On a typical cleaved surface for $YBa_2Cu_4O_8$, we obtain some areas of Cu_2O chain surface and some areas of Cu_2O plane surface. A large spot light measures them together (Figure2.2), while a small light spot measures these cleaved surfaces separately (Figure 2.3).

Currently, our laser ARPES system has a spot size of $\sim 30 \times 30\ \mu m^2$. This is sufficient for the $NdFeAsO_{(1-x)}F_x$ sample shown in Figure 2.1, because the spot size is smaller than the size of a single crystal grain. However, other materials may have single crystal grains much smaller than $NdFeAsO_{(1-x)}F_x$. This requires focusing the light further to an even smaller spot size. The wavelength of the light is around 200 nm. Therefore, it is impossible to focus the light on a spot with a diameter less than 200 nm. For our study, we set our goal to focus the light spot to a 1 μm diameter.

There are a variety of optic devices that can focus beam of light. The most common is a convex lens. Ideally, a convex lens focuses a parallel incident light on a single point. However, rays with different wavelengths are focused to different points. Since the laser produces light wavelengths in a range from 178 to 230 nm, the focal point will change when we tune the wavelength. As a consequence, we must adjust the lens' position each time we change the wavelength. More importantly, convex lens suffers from spherical aberration problem, which puts lower limit on the size of the spot of $\sim 30\ \mu m$. For these reasons, we do not use convexes lens to focus the light. Instead, we use Schwarzschild Objectives, because they are based on light reflection and the focal length is the same for rays of all wavelengths.

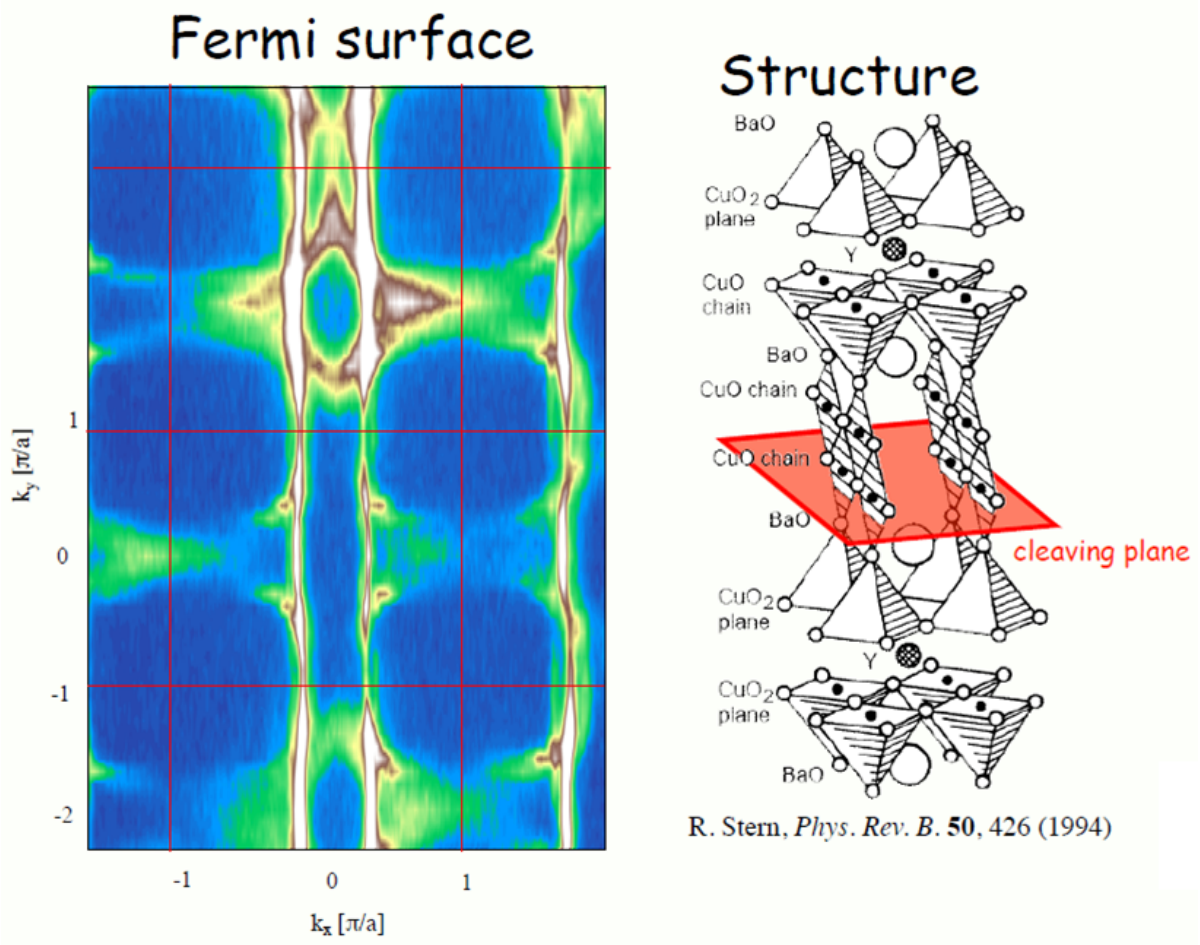

Figure 2.2 Electronic and crystal structure of $YBa_2Cu_4O_8$. [7]

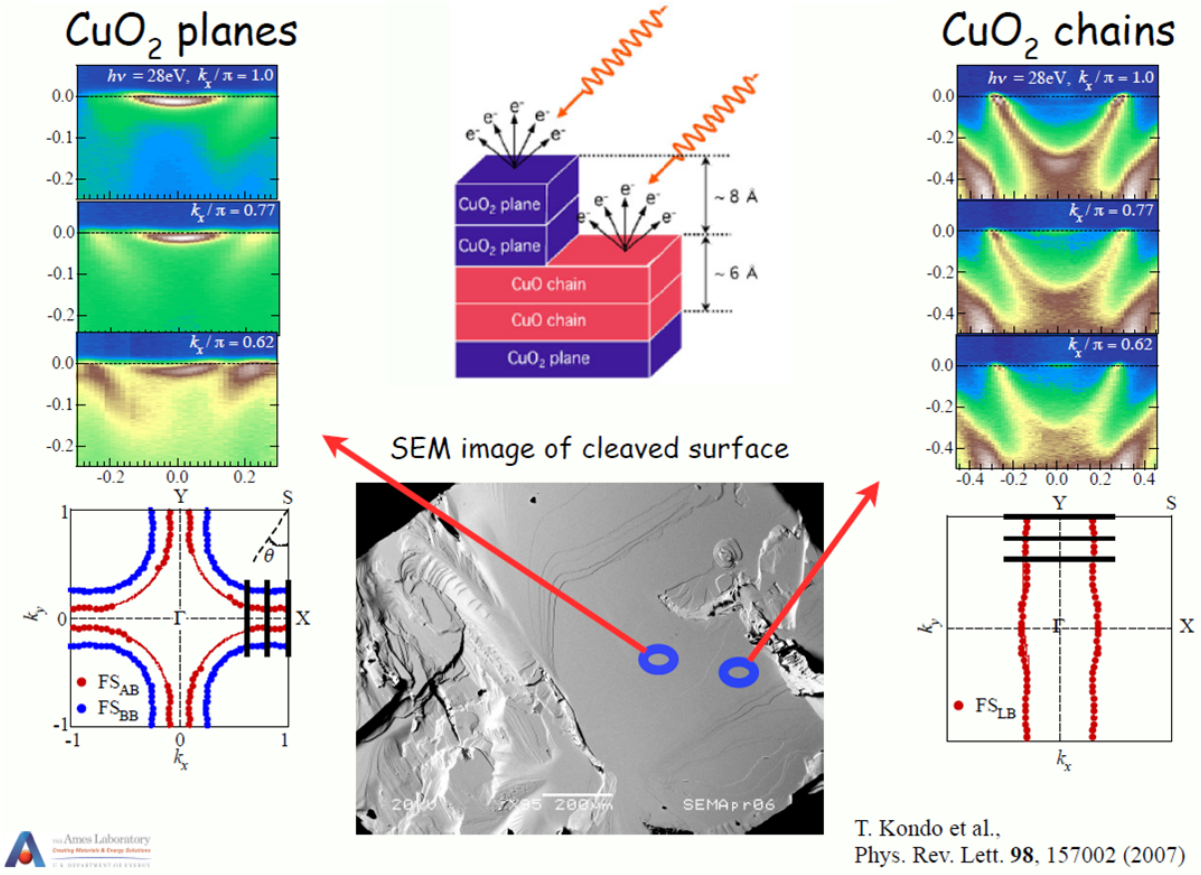

Figure 2.3 Different cleaved planes of $YBa_2Cu_4O_8$ have different band structures measured by ARPES. [8]

2.2 Working Principle of Schwarzschild Objective

A Schwarzschild Objective (SO) consists of two concentric spherical mirrors — one convex and one concave — as shown in Figure 2.4. The large concave mirror on the left has a hole in the center to allow light to pass through. Incident light comes from point P, goes through the center hole of the concave mirror, reflects at the convex mirror, then reflects from the concave mirror, finally arriving at point Q. In Figure 2.4, Φ_1 and Φ_2 are the diameters of the two mirrors, and R_1 and R_2 are the radii of curvature, respectively. C is the center of these two sphere mirrors. The magnification of the SO depends only on the ratio of the radii of these two mirrors [35]:

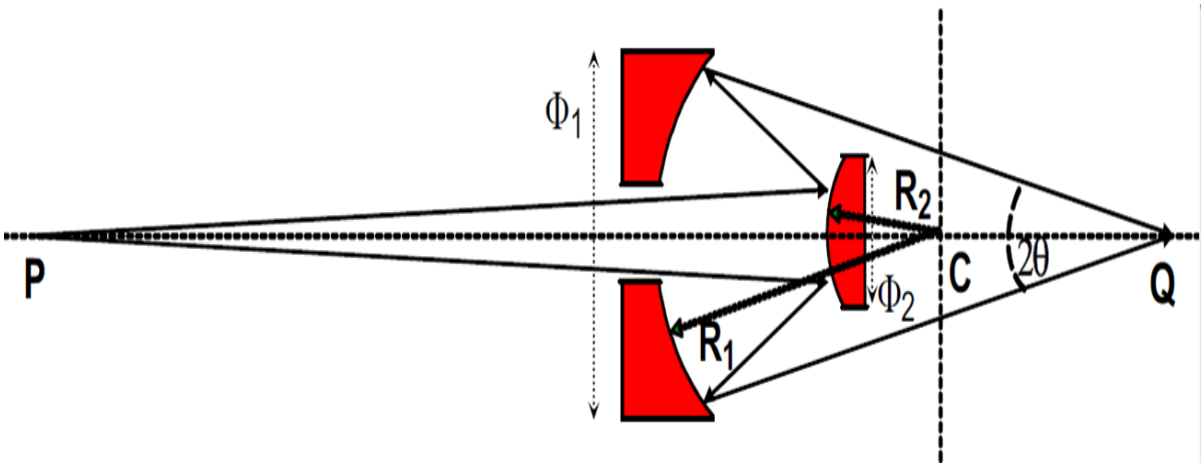

Figure 2.4 Ray diagram of a Schwarzschild Objective. [9]

$$M = \frac{r - 1 + \sqrt{r}}{r - 1 - \sqrt{r}}, \tag{2.1}$$

where $r = \frac{R_1}{R_2}$ is the ratio. Under the condition of small incident angle (< 0.5 rad), first order of spherical aberrations cancel for the two mirrors. [35].

2.3 Requirements

There are commercially available SOs. The SO produced by Edmund Optics (Stock No. 59885) has ideal optical properties for our purposes. However, it is too big to fit in front of the

sample holder without touching the lens of the electron analyzer. Therefore, we must design our own SO. It should satisfy the following requirements.

First, the two mirrors for SO and all mechanical components holding these parts must fit in the vacuum chamber. They must be located in the light's path, ∼30 mm (the focal length of SO) from the sample, and not touch the electron analyzer lens. A sketch of the sample area in the UHV chamber is shown in Figure 2.5. Based on the drawing, the diameter of the concave mirror can not be greater than 1.97 inches or 50 mm. The diameter of the convex mirror can not be greater than 0.32 inches or 8.13 mm.

Second, the SO must have a large magnification and low diffraction limit. The magnification is calculated by Eq. 2.1, which can be rewritten as

$$M = 1 + \frac{2}{\sqrt{r} - \frac{1}{\sqrt{r}} - 1}. \tag{2.2}$$

To maximize the value of M, r must be greater than and close to 2.62 ($r \to 2.62+$). On the other hand, the diffraction limit of a concave mirror is calculated by

$$\Delta x = 1.22\lambda \frac{d}{\Phi_1}, \tag{2.3}$$

where λ is the wavelength of the light, d is the distance between the focal plane and the concave mirror, and Φ_1 is the diameter of the concave mirror. The wavelength is always in the range of 178 to 230 nm. Image distance, d, depends on the focal length of SO, which is not sensitive to the change of the other parameters. As a result, we can treat λ and d as constants in Eq. 2.3. According to Eq. 2.3, a larger Φ_1 provides a lower diffraction limit. Therefore, we would like Φ_1 to be close to 50 mm (the largest possible value) and r to be close to 2.62.

Third, the focal depth of SO must be as large as possible. Focal depth is a concept that measures the tolerance of placement of the image plane in relationship to the lens as shown in Figure 2.6. The light is focused on the smallest spot on the focal plane, and the distance between the lens and the focal plane is the focal length. If we place a screen parallel to the focal plane, but away from the focal point, the size of the spot on the screen is larger than that on the focal plane. As the screen is moved farther from the focal plane, the spot size on

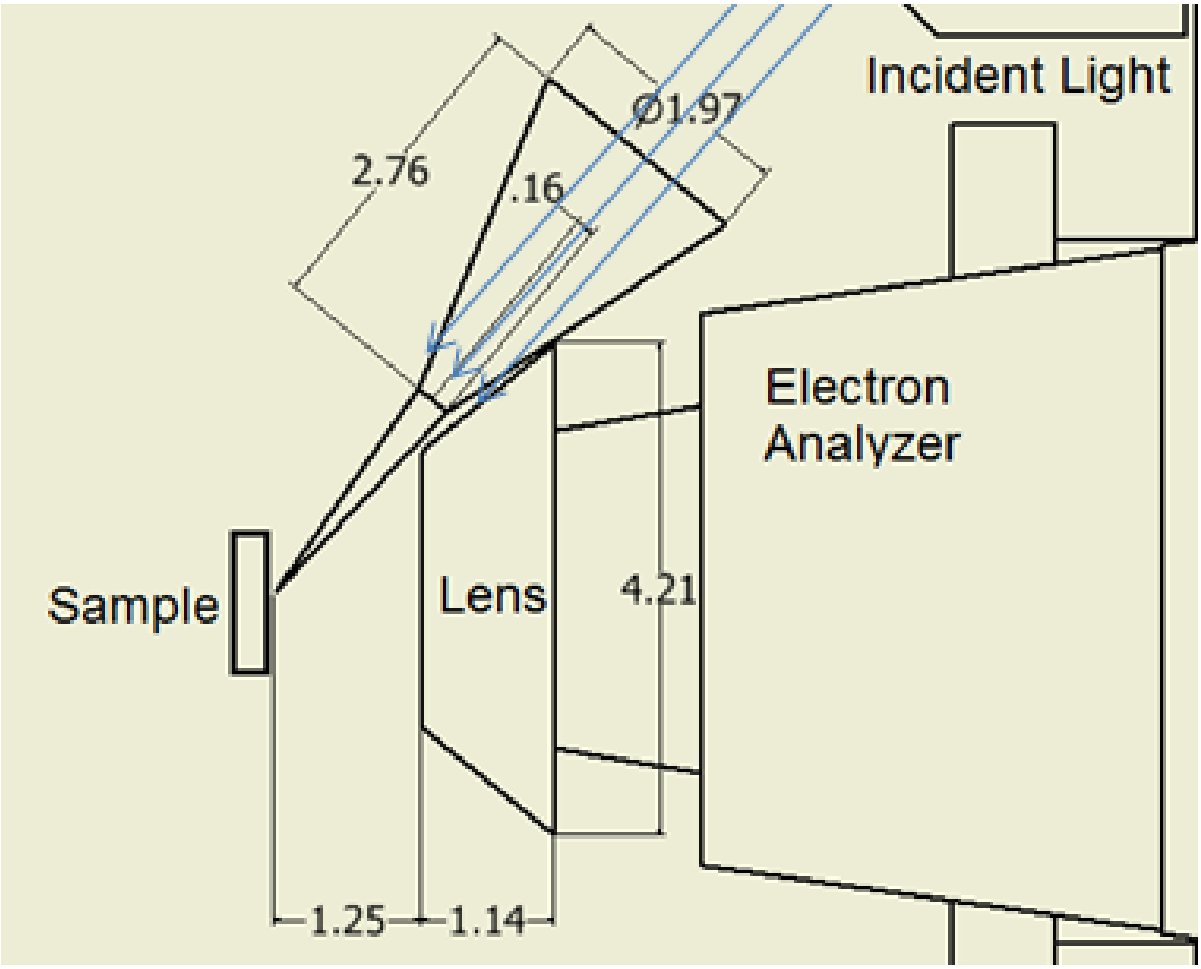

Figure 2.5 Top view of the sample area in a vacuum chamber. The blue arrows are incident light rays. The distance between the sample and the electron analyzer lens is marked, as well as size of the lens. A cone with the maximum allowed dimensions for SO is shown between the sample and the incident light. The unit for all numbers is inches.

the screen increases. If the spot size does not exceed $\sqrt{2}$ times the minimum size, we say the screen is within the focal depth of the lens. An SO with a larger focal depth tolerates more misalignment of the sample. A smaller Φ_1 provides a larger focal depth. This is contradictory to the second requirement. We will calculate the value of Φ_1 in the next section to determine the optimum design for the SO.

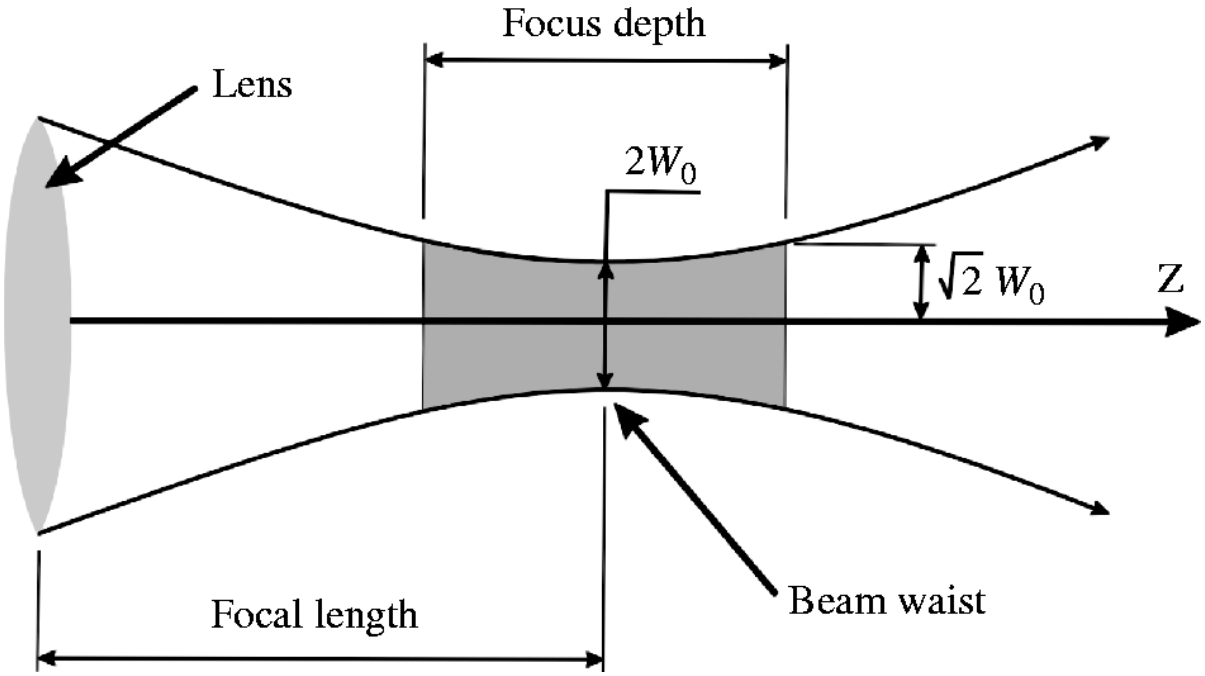

Figure 2.6 Concept of focal depth.

Fourth, the precision grade of the surface of the two mirrors must be at least $\lambda/20$. Precision grade is a variable to specify the deviation of an optical surface. Since our final spot size is close to the diffraction limit, the precision grade of the SO must be very high. The precision grade is measured using an optically smooth test surface. When the test surface is placed against the sample mirror, fringes appear whose shape dictates the sample mirror's precision grade. If the fringes are evenly spaced, straight, and parallel, the sample mirror is as good as the test surface. If the fringes are curved, the number of fringes between two imaginary lines, one tangent to the center of a fringe and one through the ends of this same fringe, indicate the deviation. The precision grade is often measured in values of the test light wavelength, λ. One fringe corresponds to $\lambda/2$.

Finally, the light intensity loss should be minimized. In the SO system, the incident light may lose intensity near four places, (1) Hole of the concave mirror, (2) Center of the convex mirror, (3) Edge of the concave mirror, (4) Edge of the convex mirror. as shown in Figure 2.7. If the hole of the concave mirror is too small compared with the incident angle at point P in Figure 2.4, those rays with a large incident angle will be blocked by the edge of concave mirror (Ray 1 in Figure 2.7). On the other hand, the reflected ray from the convex mirror with a very small incident angle will go through the hole of the concave mirror and be lost (Ray 2 in Figure 2.7). If the diameter of the concave mirror is too small, it cannot catch the rays reflected at the edge of the convex mirror (Ray 3 in Figure 2.7). If any ray hits the convex mirror more than once, it will not arrive at the focal point and will be lost (Ray 4 in Figure 2.7). Therefore, all rays that finally reach point Q in Figure 2.4 leave a ring shape bright area on the convex mirror. By calculating the solid angle of this area with respect to point P divided by the total solid angle of all rays emitted from point P, we obtain the energy loss for the SO. The intensity loss cannot be completely eliminated regardless how we design the two mirrors. However, by carefully selecting the diameters of the two mirrors and the size of the hole at center of the concave mirror, we can minimize the intensity loss.

2.4 SO Design

For the design of SO, we can tune the radius of the two mirrors, R_1 and R_2, to optimize the magnification and focal depth of the SO. Additionally, we can tune the diameters of the two mirrors, as well as the hole in the concave mirror, to optimize the diffraction limit, focal depth, and intensity loss of the SO. We designed a program with a software called "Igor" to determine the optimum parameters for the SO.

The ray diagram for SO is shown in Figure 2.8. The origin is the center of the two mirrors. The concave mirror is represented by two arcs located on the circle with radius R_1, while the convex mirror is represented as an arc on the circle with radius R_2. Suppose the light source position is at P(x_0, y_0) and a light ray is emitted at angle α with respect to the horizontal line. This light ray hits the convex mirror at point A. The position of point A, (x_1, y_1) is the solution to the equations

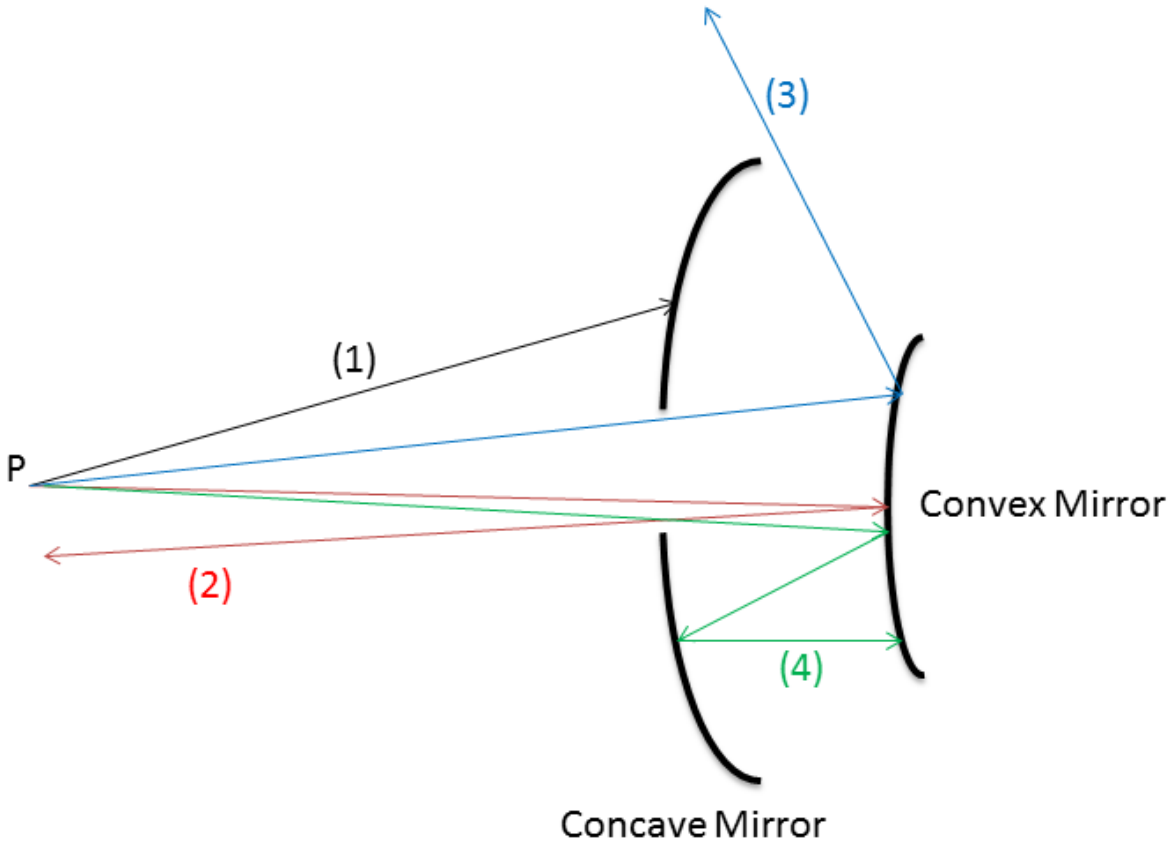

Figure 2.7 Possible ways to lose intensity.

$$\begin{cases} \frac{y_1-y_0}{x_1-x_0} = tan\alpha \\ x_1^2 + y_1^2 = R_2^2 \end{cases} . \tag{2.4}$$

The reflected ray, AB, from the convex mirror and the incident ray, PA, are symmetric about line OA from the origin. Therefore, the intersection of ray AB and the concave mirror, B(x_2, y_2), can be calculated from the equations

$$\begin{cases} \frac{y_2-y_1}{x_2-x_1} = tan(2arctan(\frac{y_1}{x_1}) - \alpha) \\ x_2^2 + y_2^2 = R_1^2 \end{cases} . \tag{2.5}$$

The ray is then reflected again by the concave mirror at point B. Point Q is the point where ray PABQ and another ray with incident angle $-\alpha$ (PA'B'Q) cross. Q is the focal point and its position, (x_3, y_3), is given by

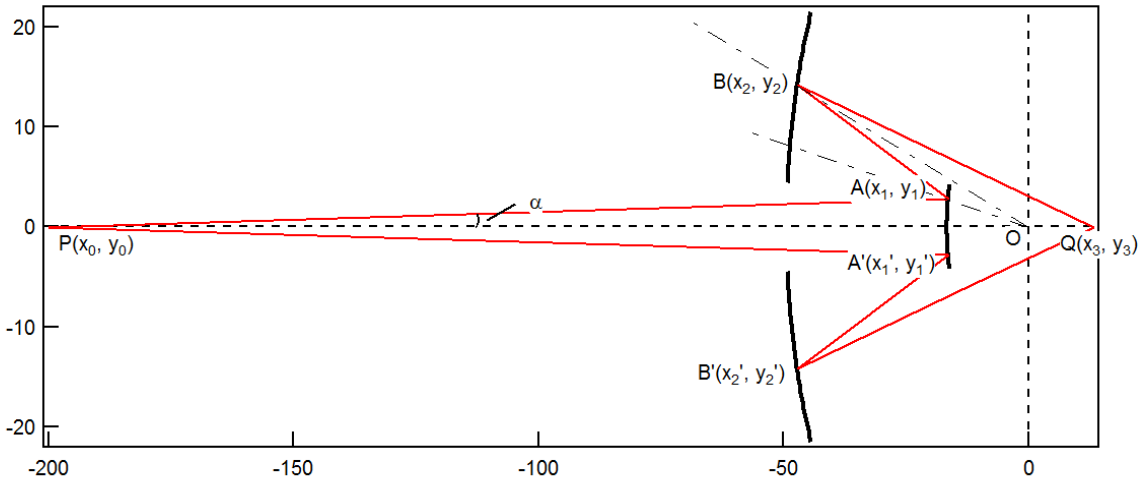

Figure 2.8 Ray diagram of the Schwarzschild objective. The unit is mm for both x and y axes.

$$\begin{cases} \frac{y_3-y_2}{x_3-x_2} = tan(2arctan(\frac{y_2}{x_2}) - arctan(\frac{y_2-y_1}{x_2-x_1})) \\ \frac{y_3-y_2'}{x_3-x_2'} = tan(2arctan(\frac{y_2'}{x_2'}) - arctan(\frac{y_2'-y_1'}{x_2'-x_1'})) \end{cases} . \tag{2.6}$$

The effective magnification, M_{eff}, is calculated by the ratio of $|\frac{y_0}{y_3}|$. It is close to the magnification, M, calculated from Eq. 2.1 at small incident angles. The diffraction limit Δx is calculated from Eq. 2.3, where d $= x_3 + R_1$ and $\Phi_1 = 2y_2$. The focal depth d_f is calculated from y_3 and θ in Figure 2.4: $d_f = \frac{(\sqrt{2}-1)y_3}{tan\theta}$.

Figure 2.9 shows the user interface of the software to calculate the SO's performance. Inputs are on the left side and outputs are on the right side. In the input column, "a max" is the maximum value for θ in Figure 2.4. "Original Spot Size" is twice y_0. "Image Distance" is $-x_0$. "Divergence Angle" is twice of angle α in Figure 2.8. By tuning these parameters, we optimized a SO with performance satisfying all requirements. The concave mirror has 49.3 mm radius and 43 mm diameter, while the convex mirror has a 16.6 mm radius and 8.5 mm diameter.

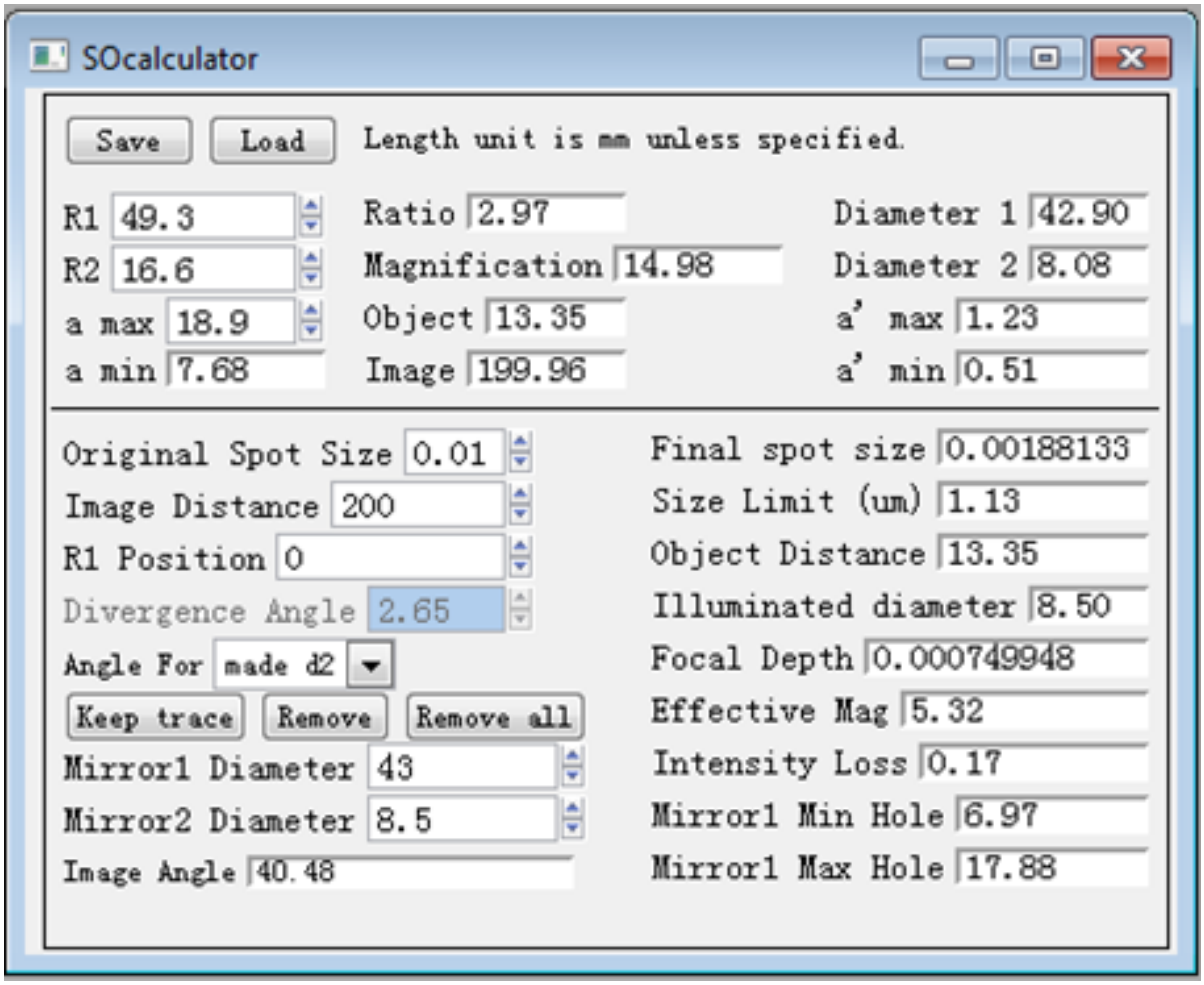

Figure 2.9 User interface of SO performance calculator.

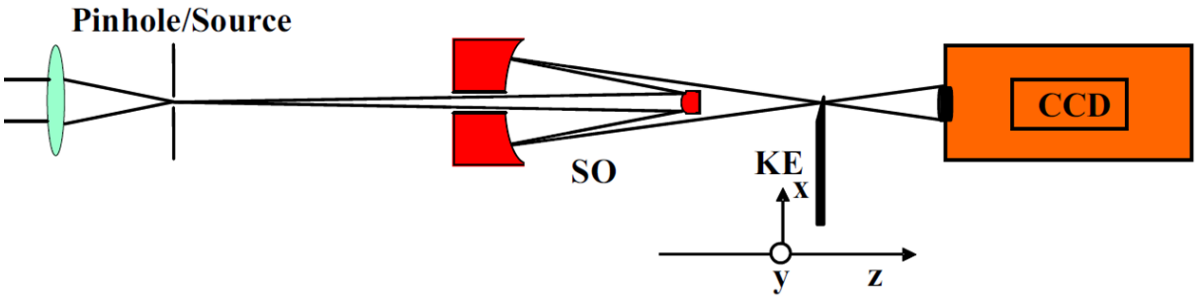

Figure 2.10 Schematic of the experimental setup for the SO alignment by means of the revised Foucault test (not to scale); KE = knife edge. [9]

2.5 SO Test

Before assembling the two mirrors and installing them inside the vacuum chamber, we test them on an optical table to verify their performance is as good as our calculations. The first step of the SO test is to align the two mirrors accurately. A revised Foucault test is applied to guarantee alignment, shown in Figure 2.10.

In the Foucault test, we fix the convex mirror at a position between the light source and a CCD camera. The position and rotation of the concave mirror are adjustable. We define the z-direction to be the direction parallel to the light path, the x-direction to be parallel to the surface of the paper and perpendicular to the z-direction, and the y-direction to be perpendicular to both x- and z-directions, as shown in Figure 2.10. The main axis is the same as the line (x = 0, y = 0). A knife edge (KE) is in the focal plane and can move in the x-direction with very high precision. Initially, the KE is placed at x = -10 μm, and the CCD camera is reading the full image on a plane to the right of the focal plane. As the KE moves up and reaches the light spot in the focal plane, it starts blocking part of the image on the CCD screen. When the KE moves to x = 0, it should block half of the image on the CCD if the two mirrors are aligned perfectly. And if the KE moves up more, it will finally block the entire image on the CCD.

Figure 2.11 shows the simulation results when the KE is moved to x = 0, blocking half of the light spot at the focal plane, (a) is the image on the CCD of the target alignment, and (b),

Figure 2.11 Zemax image simulation.

(c) and (d) are the images if the concave mirror is misaligned by 1 mm from y = 0, x = 0, or z = 0, respectively. The position of the concave mirror is adjusted by comparing the simulation images with the images captured by the CCD. Therefore, the optimum alignment for these two mirrors is achieved.

The size of the pinhole in Figure 2.11 is 10 μm. This is also the size of the incident light spot. We must measure the size of the light spot at the focal plane to calculate the effective magnification of the SO. After the alignment of the two mirrors, we replace the CCD camera with a power meter (Newport, model 1918-C). Measure the power of the light passing through the KE as a function of the KE's position. The results are shown in Figure 2.12a. Initially, the KE position is 0 (about -3.5 μm in x-direction). It does not block any light. When it moves 2.8 μm, it starts to block light, and blocks all light at position 4.2 μm. Figure 2.12b is the derivative of the curve in Figure 2.12a and its Gaussian fit. The size of the light spot is equal to the full width at half maximum (FWHM) of the Gaussian fit, 1.8 μm. This agrees well with the calculated result, 1.88 μm, shown in Figure 2.9.

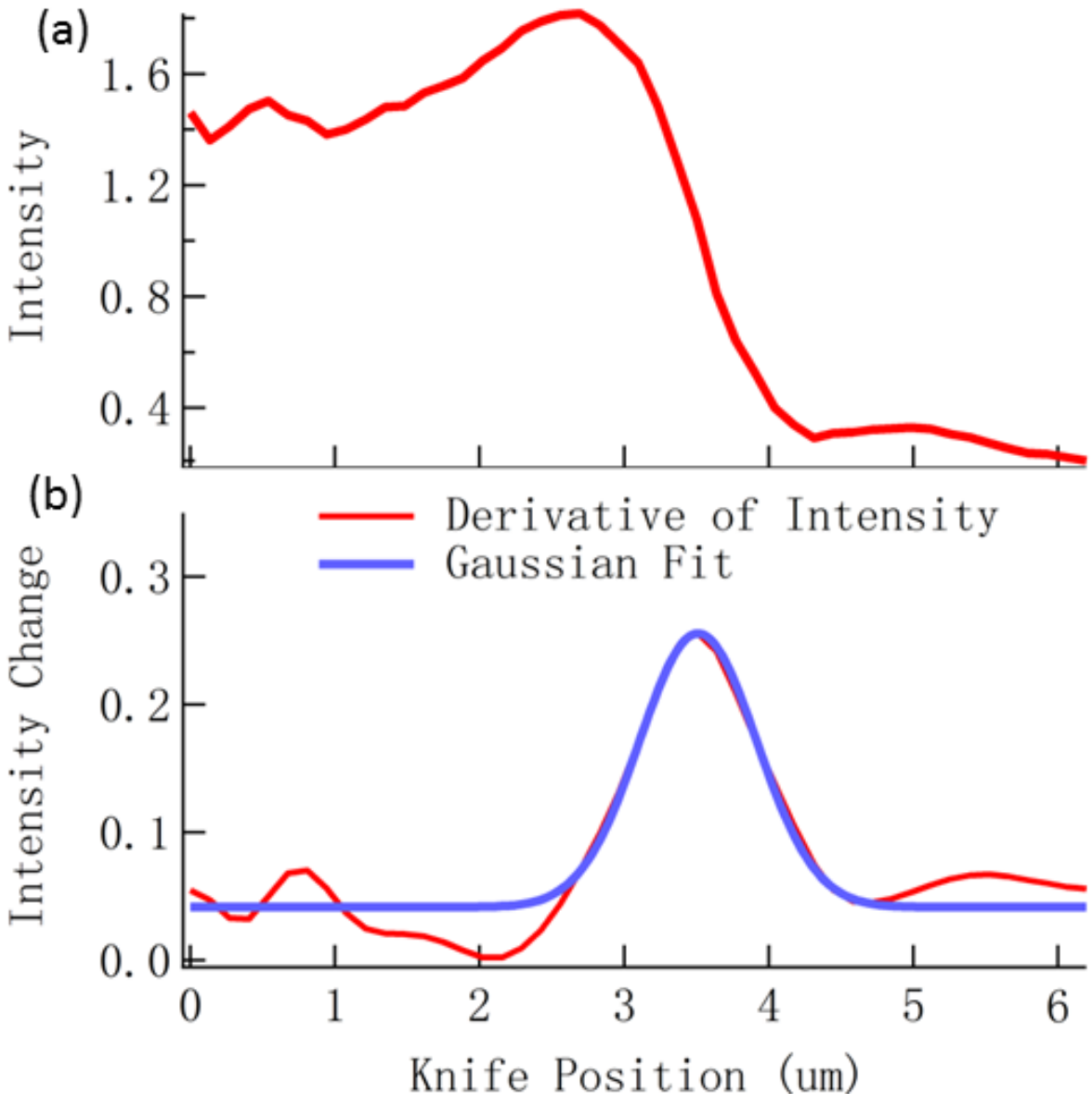

Figure 2.12 (a) The power of light measured by the power meter versus the KE position. Intensity unit is μW. (b) The derivative of (a), and its Gaussian fit. The knife position is not the same as the x coordinate.

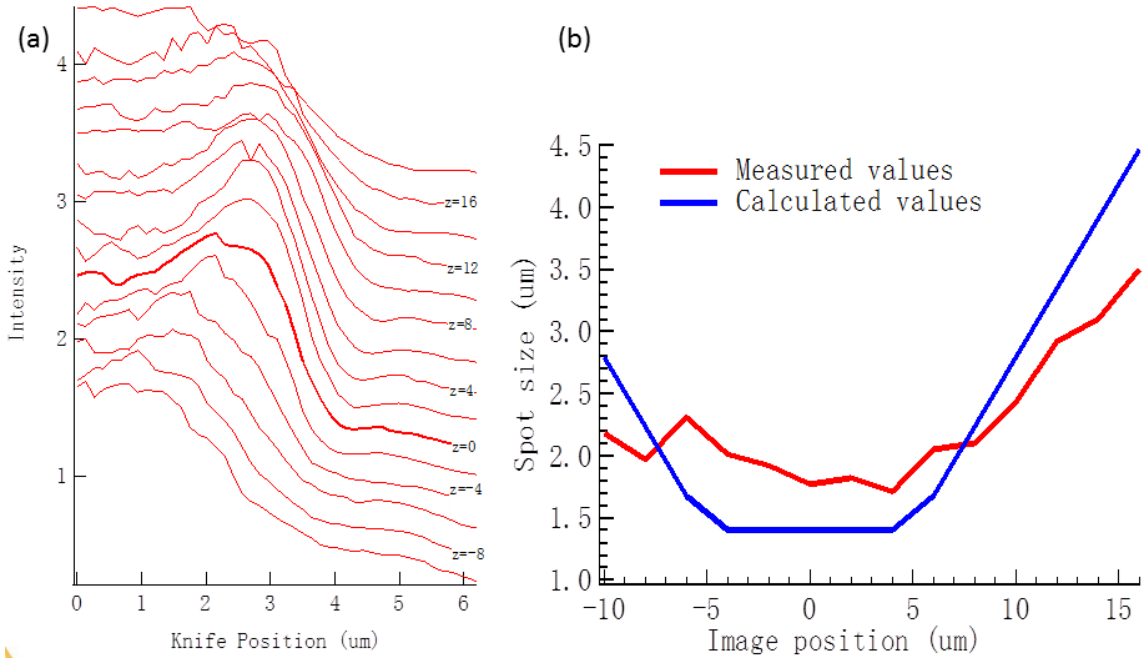

Figure 2.13 Focal depth measurement.

If we change the position of the KE in the z-direction and repeat the measurements in Figure 2.12, we obtain the light spot size at different planes parallel to the focal plane. Then, we calculate the focal depth of SO. The result is shown in Figure 2.13a. Different red curves are shown in Figure2.12a measured by placing the KE at different z-positions from -10 to 16 μm. Figure 2.13b shows the spot size as a function of the position of the image. The blue curve is the calculated result from our SO calculator, the flat bottom of this curve results from the diffraction limit. The red curve is the result extracted from Figure 2.13a. For each curve in a, we compute its derivative and apply Gaussian fit to the results. The FWHM is the y-axis in Figure 2.13b, while the z values are the x-axis. Experimental results agree well with calculations.

The test results show the SO satisfies all the requirements. We are ready to install the SO in the ARPES system, once a device to hold the two mirrors is made and allows to attach it inside the vacuum chamber without touching the lens of the electron analyzer. The design drawing is shown in Figure 2.14. The material for this device is aluminum. Because aluminum is light, strong enough to hold the mirrors, and non-magnetic. The convex mirror is fixed on a tripod

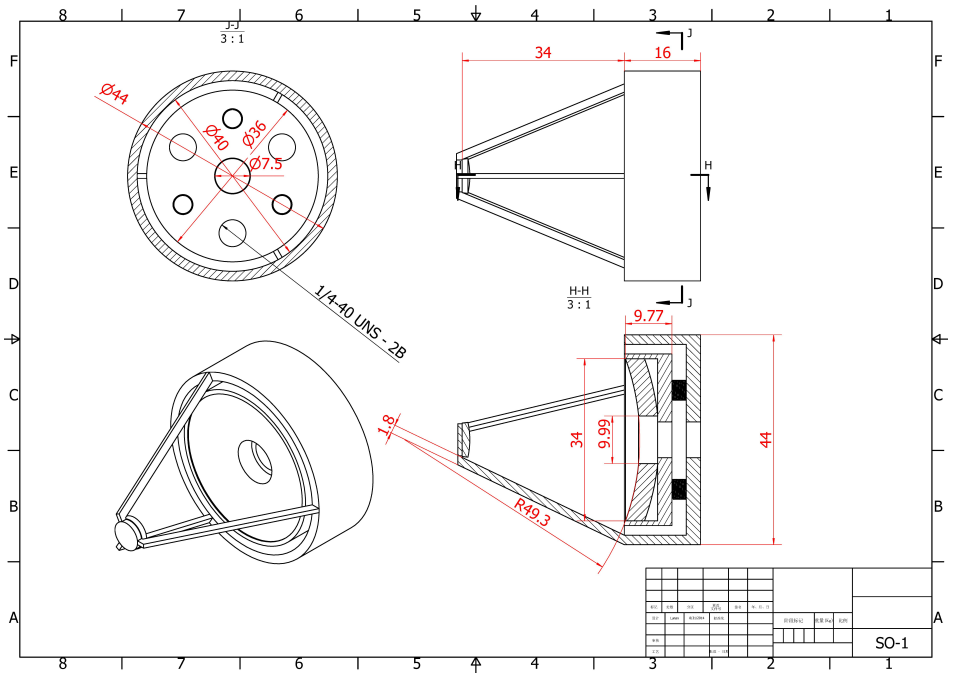

Figure 2.14 Design of SO holder. All units are in mm.

support, designed to be as thin as 0.5 mm to minimize the light blocked by it. The concave mirror is attached to a wide, shallow cup inside another cup. These two cups are connected with three springs. Three screws on the larger cup are utilized to adjust the position of the inner cup with respect to the outer cup, then adjust the position of the concave mirror. This is the development of the SO in our laboratory to date. Future work includes machining the SO holder, placing it inside the vacuum chamber, and testing its performance by conducting ARPES experiments to measure real samples.

CHAPTER 3. COLD FINGER

3.1 Introduction

The cold finger is the device in the ARPES system that holds the sample in the UHV chamber and cools it to low temperatures. The ability to cool samples provides a variety of benefits. First, it allows measurement of a sample's electronic band structure at different temperatures and resolve how it varies with temperature. Second, low temperatures can reduce pressure in the UHV chamber further and produce a higher vacuum because many gas molecules will condense on the cold finger at temperatures below their boiling point. Third, in some cases the sample's surface remains pristine longer for effective ARPES measurement at low temperatures. Therefore, unless there is a reason (i.e., need to resolve phase transition or band structure above Fermi level) to increase the temperature, it is best to conduct ARPES experiments at a temperature as low as possible.

Liquid helium (LHe) has a boiling point of 4.2 K. Using LHe is a traditional method to cool samples. The advantage of this method is its device is simple. A sample can reach a low temperature (4.2 K) with just a LHe dewar. LHe cools a sample by thermal contact with the sample. However, this method is not easy to use in our ARPES experiment, because it consumes too much LHe during cooling. For example, to cool 1 kg copper from room temperature, 300 K to 4.2 K, will utilize 32 L LHe. Typical LHe consumption for an ARPES system is about 200 L per week. The price of LHe is \$7 / L, which is prohibitively expensive, not to mention that He is non-renewable resource.

Currently our laboratory uses a Gifford-McMahon refrigerator to build the cold finger (Figure 3.1). This cold finger can cool samples to $\sim$ 15 K. However, many samples have interesting properties below 15 K. For example, Niobium-titanium (NbTi) is a superconductor with critical

temperature 10 K [36]. We would like to measure its electronic structure below 10 K. Another disadvantage of this cold finger is the motor is installed directly on top of this cold finger connected with the sample by a rigid metal rod. Therefore, when the cold finger is working, it introduces a lot of vibrations to the sample. The amplitude of this vibration is about 20 μm. In this case, the incident light will not always hit the same place on the sample's surface during the measurement. The case is worse, if the light spot becomes smaller. To reduce the sample's vibration and reach a lower sample temperature, a pulse tube refrigerator was purchased and a cold finger was constructed for it. Next, we explain the principle of a pulse tube refrigerator.

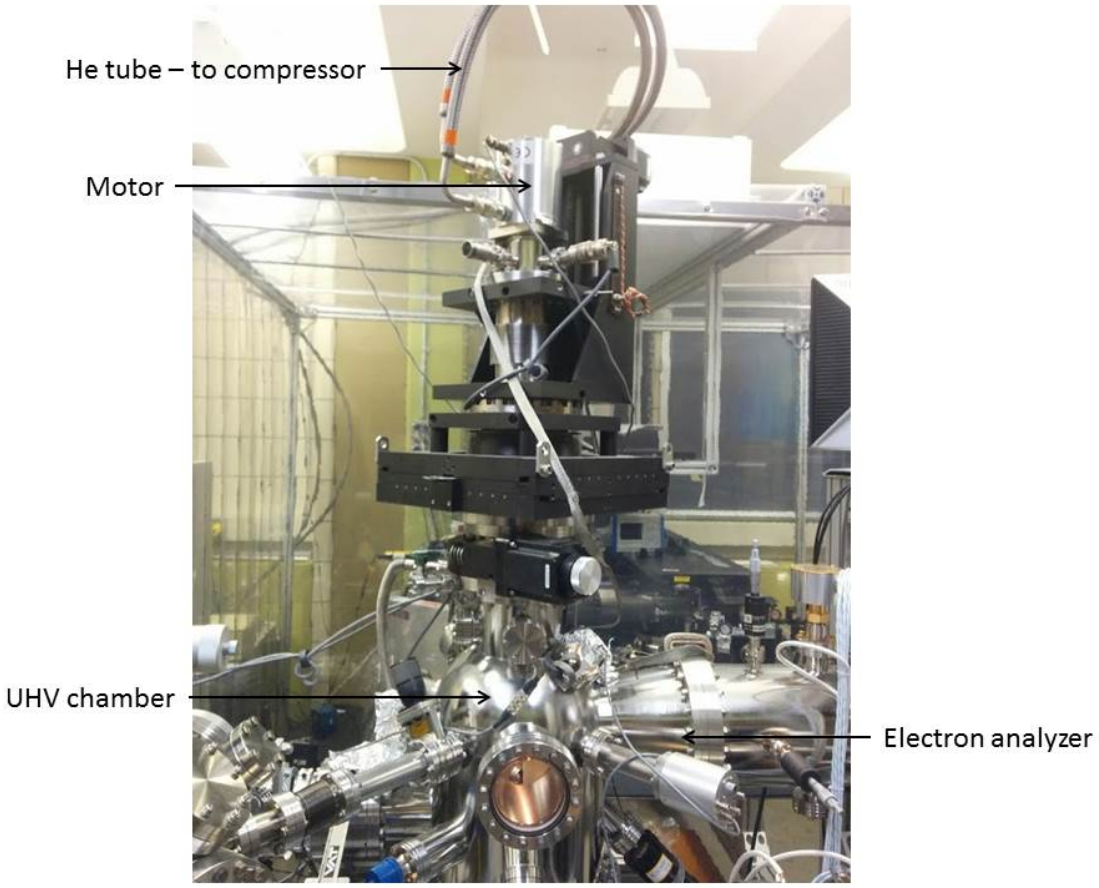

Figure 3.1 Cold finger in the laser ARPES system in Ames laboratory.

3.2 Principle of a Pulse Tube Refrigerator

A schematic drawing of a single stage pulse tube refrigerator (PTR) is shown in Figure 3.2. A model PTR consists of (1) helium gas filled everywhere, (2) a compressor that moves back and forth to compress and expand the helium gas, and (3) heat exchangers X_1, X_2, X_3 to exchange heat with the environment. T_H is a high environment temperature, while T_L is a low environment temperature, (4) a regenerator with a large specific heat, working as a heat sink, (5) a tube (often called "the pulse tube"), (6) an orifice which controls the flow rate between the buffer tank and the pulse tube, and (7) a buffer volume, whose pressure is kept constant.

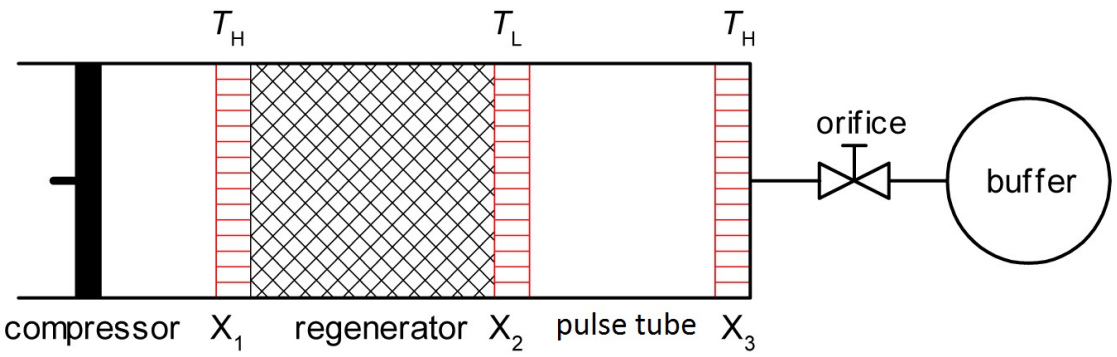

Figure 3.2 Schematic drawing of a Stirling-type single-orifice PTR. From left to right: a compressor, a heat exchanger (X_1), a regenerator, a heat exchanger (X_2), a tube (often called "the pulse tube"), a heat exchanger (X_3), a flow resistance (orifice), and a buffer volume. The cooling is generated at the low temperature T_L. Room temperature is T_H. [10]

Next, a working cycle of the PTR is described. As the compressor moves to right, the volume of the pulse tube decreases. Thus, as the helium pressure increases, the pressure in the pulse tube is higher than the pressure in the buffer. This high pressure helium gas moves from the pulse tube to the buffer through the orifice. On the other hand, according to the ideal gas law, $pV = nRT$, high pressure results in high temperatures and more heat. Since the gas is moving from left to right, it brings heat to the heat exchanger, X_3, and releases heat to the environment through X_3. As the compressor moves to left, the volume of the pulse tube increases. Thus, the helium pressure decreases and, the pressure in the pulse tube is lower than

the pressure in the buffer. Low pressure helium gas moves from the buffer to the pulse tube through the orifice. On the other hand, according to the ideal gas law, low pressure results in low temperature and less heat. Since gas is moving from right to left, it absorbs heat from the heat exchanger, X_2. The regenerator on the other side of the heat exchanger, X_2, retains a constant temperature gradient between X_2 and X_3. Since the compressor moves back and forth continuously, the helium gas in the pulse tube repeats releasing heat to X_3 and absorbing heat from X_2. Therefore, the environment at X_2 is cooled to low temperatures.

The performance of the PTR is mostly determined by the quality of the regenerator. A temperature of 10 – 50 K can be achieved with lead as the regenerator material. Below 10 K, magnetic materials are used as the regenerator. However, magnetic materials cannot be used on our cold finger, because the sample is mounted on the cold finger and the magnetic field produced by the PTR will deflect the photoelectrons excited from the sample surface. An alternative way to obtain a lower temperature is to use a two-stage PTR, as shown in Figure 3.3. The principle of a two-stage PTR is the same as a one-stage PTR. The difference is another pulse tube with its heat exchanger, X_1, connected to the heat exchanger, X_2, for a single-stage PTR. Therefore, the temperature at the second stage (CT2) is lower than the temperature at first stage (CT1).

3.3 Requirements

There are three main requirements for the new cold finger. First, it should be able to cool the sample to a temperature as low as possible, at least lower than 4.2 K — the boiling point of LHe. This allows measurement of the band structure of samples and reveals sample electronic properties at low temperatures. Second, its vibration amplitude should not exceed 1 micrometer in all directions. This ensures the incident light points to the same position on the sample throughout a measurement and eliminates the influence of polycrystalline, inhomogeneous, and rugged samples as discussed in Chapter 2. Finally, its installation and removal should be easy for the ARPES system. Because we keep upgrading the ARPES system, the cold finger needs to be installed and detached fairly frequently (several times per year).

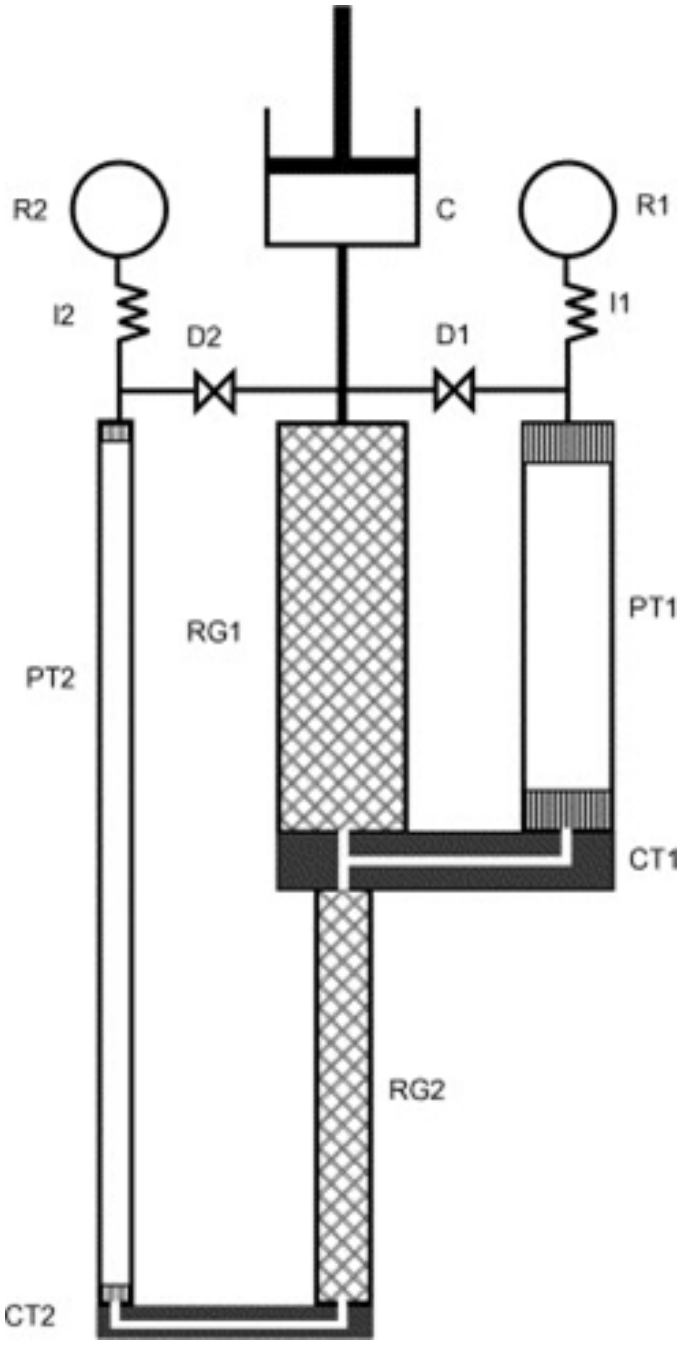

Figure 3.3 Schematic drawing of the two-stage PTR with gas-coupled stages; C: compressor; R1, R2: reservoirs; PT1, PT2: pulse tubes of first and second stage; RG1, RG2: first stage and second stage regenerators, CT1, CT2: cold tips; I1, I2: inertance lines; D1, D2: second-inlet valves. [11]

3.4 Cold Finger Design

The temperature and vibration requirements are satisfied by purchasing a commercially-available pulse tube refrigerator — PT410-RM-CP289C (PT410) produced by Cryomech Inc. The commercial PTR has two stages. Its cooling power is 31.5 W @ 45 K at the first stage and 0.9 W @ 4.2 K at the second stage. If there is no load at all, the temperature can reach as low as 2.8 K at the second stage. The cold head cannot be heated up above ~ 80°C.

To improve the vacuum in the UHV chamber, we need to periodically "bake" it. That is, to increase the temperature of the chamber to 120 $\sim$ 140 °C, continuously pumping at these temperatures for a few days and cool the chamber to room temperature slowly. Therefore, the pressure of UHV chamber can reach as low as $\sim 10^{-11}$ torr. The baking temperature (120 °C) is well above the maximum allowed temperature for the cold head of PT410. This makes it necessary to detach the cold head from the UHV chamber without breaking vacuum during baking.

The cold finger based on PT410, must therefore have good thermal contact with the sample, but allow to be disconnected for the bake. It should also hold the sample at the correct position as stated previously in the UHV chamber, and thermally isolate the second stage and the sample from the room temperature environment. The design of the cold finger is shown in Figure 3.5a. There are two coaxial stainless steel cylinders. The outer cylinder is straight, and the inner cylinder is wider on top and thinner at bottom. The PT-410 is inserted into these two cylinders from the top. The outer cylinder is used for isolating vacuum from the atmosphere and supports the cold finger. The inner cylinder is thinner at bottom because (1) we want the weight of the cylinder smaller, (2) the upper part of the inner cylinder must be wider than the PT-410 cooling stages and the lower part of it must be thinner to fit inside the UHV chamber. The space inside the inner cylinder is filled with helium, while the space between inner and out cylinders is vacuum. During system baking, the cold head is removed from the top, but the vacuum in the main chamber is preserved. The vertical distance between the cold head and the sample is 41.42 inches (Figure 3.5b), which is the same as the distance between the cold head and the light source level or the center of the lens of the electron analyzer (Figure 3.5c).

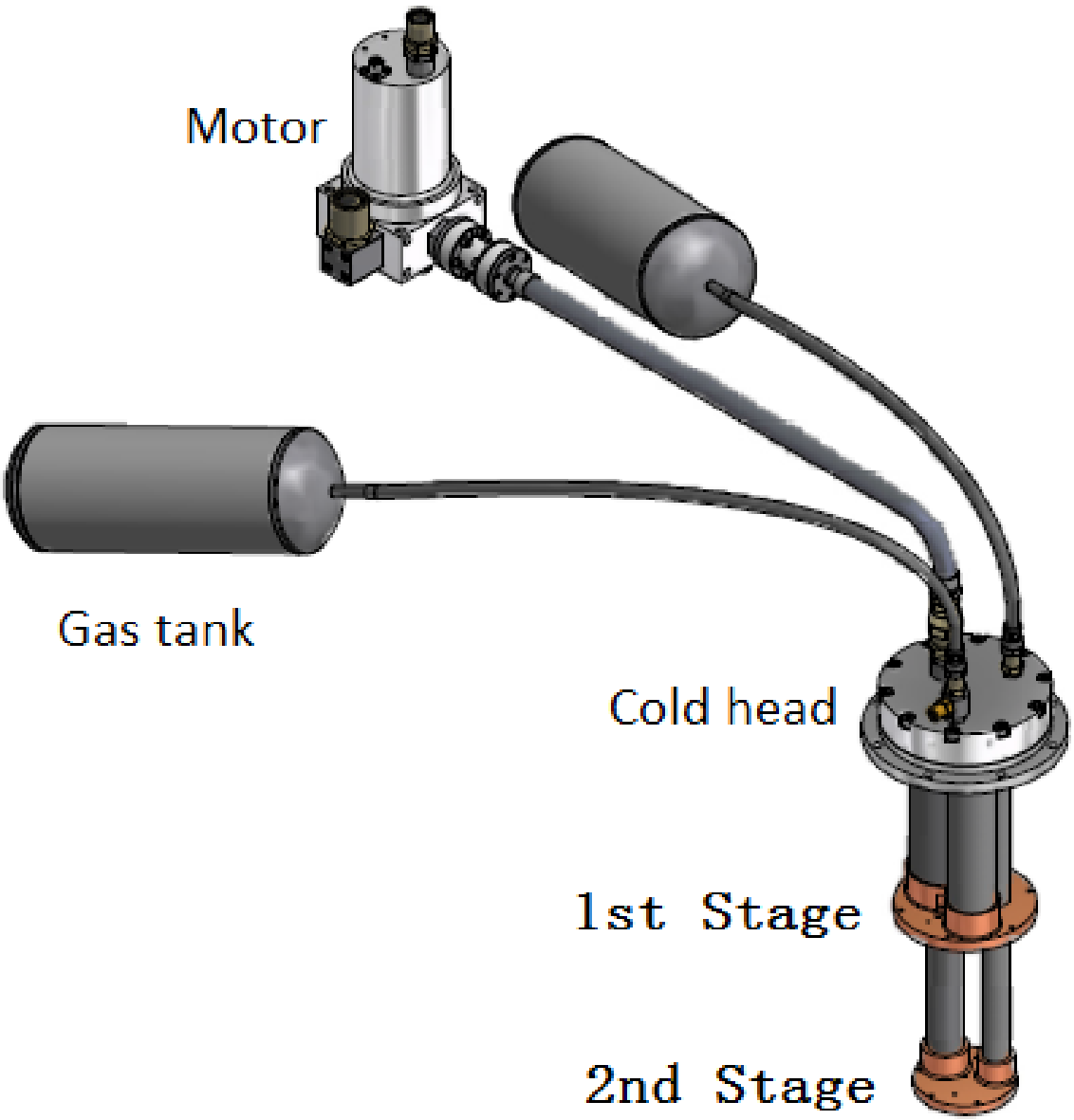

Figure 3.4 System drawing of a PT410-RM cold head.

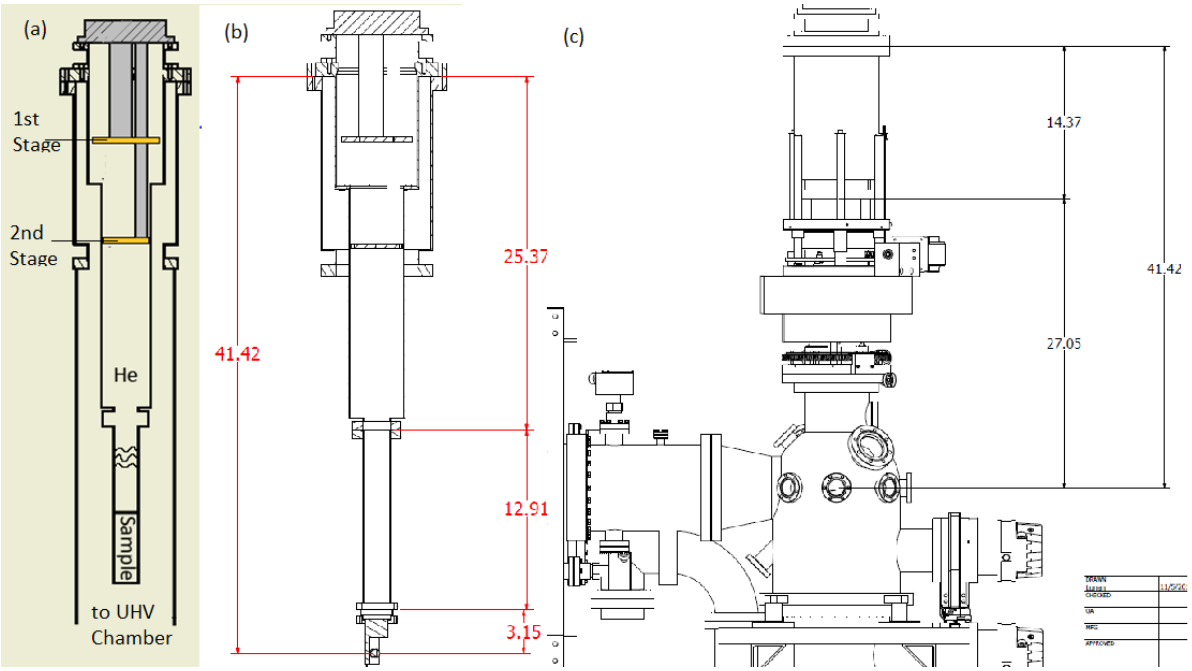

Figure 3.5 Cold finger design. (a) A schematic drawing of the cold finger. (b) A detailed drawing with main dimensions marked. (c) A schematic drawing of the cold finger installed on the ARPES system. The units in (b) and (c) are inches.

When the PT-410 is operating, the temperature at the second stage is less than 4.2 K. This temperature will liquefy helium and produce LHe. The LHe produced at the second stage drops to the top of the sample holder and cools the holder and sample. The temperatures at the top, at the first stage, at the second stage of the cold finger are room temperature (300 K), 31.5 K, 4.2 K, respectively. The cooling power of PT-410 maintains such a temperature gradient. If the heat dissipation rate is higher than PT-410 cooling power, the temperature at the second stage will not be sufficiently low to liquefy helium. The heat dissipation comes from the thermal power between two surfaces, assuming the two surfaces are identical and one surface is directly on top of the other, and thermal radiation. Thermal power, P, is given by

$$P = \frac{\kappa \cdot S \cdot \Delta T}{L}, \tag{3.1}$$

where κ is the thermal conductivity of the material between the two surfaces, S is the surface area, ΔT is the temperature difference between the two surfaces, and L is the distance between

them. The thermal conductivity of helium is 0.142 W/(m·K) at 25 °C [37], the area of the first stage is about 170 cm^2, and the distance between cold head and first stage is 7.3 inches. Based on these numbers, we estimate thermal power at the first stage, P_1, to be 3.5 W. The thermal power of the stainless wall, P_{ss}, is also calculated from Eq. 3.1. The parameters are 16 W/(m·K) for thermal conductivity of stainless steel [37], 11.96 cm^2 for the cross section area of the wall, and 7.3 inches for the wall height. The result is $P_{ss} = 27.65$ W. The exact calculation of thermal radiation power is complicated. But, it can be estimated from the Stefan-Boltzmann Law

$$P = e\sigma AT^4, \tag{3.2}$$

where e is the emissivity of the object (e = 1 for ideal radiator), A is the surface area of the object, T is the temperature, and $\sigma = 5.6703 \times 10^{-}8$ W/(m^2K^4). The emissivity of polished stainless steel is 0.075. Thus, the thermal radiation from other parts to the first stage is approximately $0.075 \cdot \sigma \cdot 170cm^2 \cdot 300^4 = 0.59$ W. Therefore, the total thermal dissipation rate at the first stage is 3.5 + 27.65 + 0.59 = 31.74 W, very close to the first stage power of 31.5 W @ 45 K on the PT-410 specification sheet. From Eqs. 3.1 and 3.2 we can also estimate the thermal dissipation rate at the second stage. Since the second stage does not connect to the stainless steel wall, it does not have the P_{ss} term as in the first stage. The result is 0.2 W, well below the power of the second stage, 0.9 W @ 4.2 K according to the PT-410 specification sheet.

3.5 Cold Finger Test

In practice, a small modification to the cold finger design may affect its performance significantly. We test the performance every time a new component is installed on the cold finger. We begin with the setup shown in Figure 3.6a. The PT-410 is installed without any shielding. Therefore, the thermal radiation power from the wall of the cold finger is larger than the cooling power of the PT-410. This setup cannot reach 4.2 K as noted in the specification sheet. A temperature sensor is attached at the second stage. This takes about one hour for the cold

finger to reach its lowest temperature (Figure 3.6b). The lowest temperature it can cool is about 5 K, which means the thermal radiation load rate at the second stage is greater than 0.9 W. After cooling is stopped, the temperature of the system takes about 30 hours to raise to room temperature.

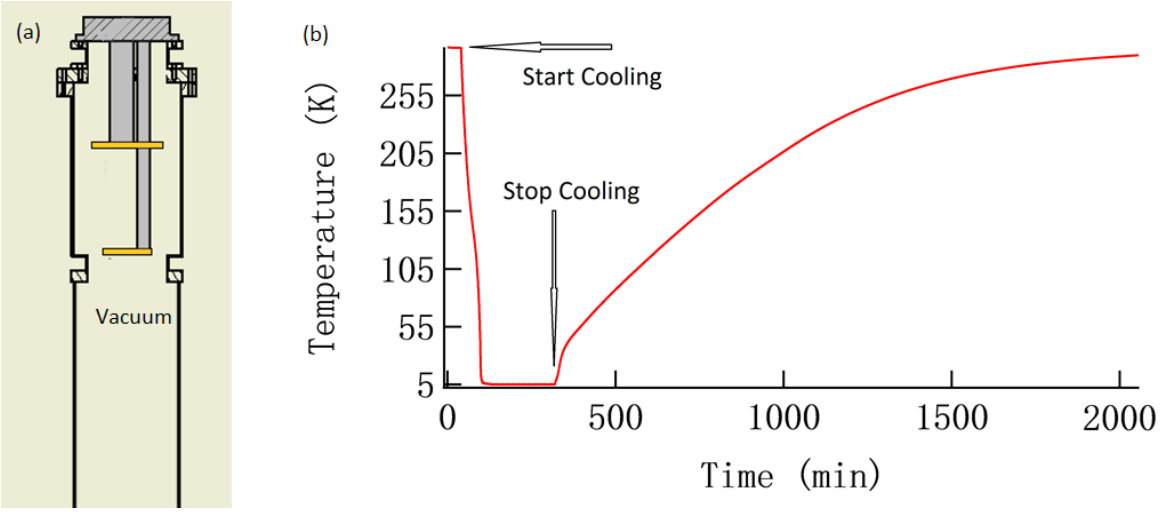

Figure 3.6 Test the cold head without any shielding. (a) Experiment setup. (b) Cooling curve.

A shielding layer is added between the outer wall and the PT-410 for the next test. A temperature sensor and a heater are attached to the second stage. We record the lowest temperature at the second stage to be 3 K when the heater is off. Then, the heater is turned on and the lowest temperature for the second stage is recorded for different heater powers. This is a good reference to know the total dissipation power for a given lowest temperature at the second stage. For example, the lowest temperature for the setup in Figure 3.6a is 5 K. It corresponds to a thermal dissipation power of 1.7 W in Figure 3.7.

During the last test, a cold finger is constructed according to the design in Figure 3.5a. To reduce thermal radiation from the outer cylinder, an extra layer of shielding is added between the inner and outer cylinders (See Figure 3.8a). Four temperature sensors are attached to the cold finger — one on the first stage, one on the second stage, one on the sample, and one on the extra shielding. Therefore, we can monitor the temperatures at different positions of the cold finger at the same time. Figure 3.8b shows the cooling curve of this setup. The

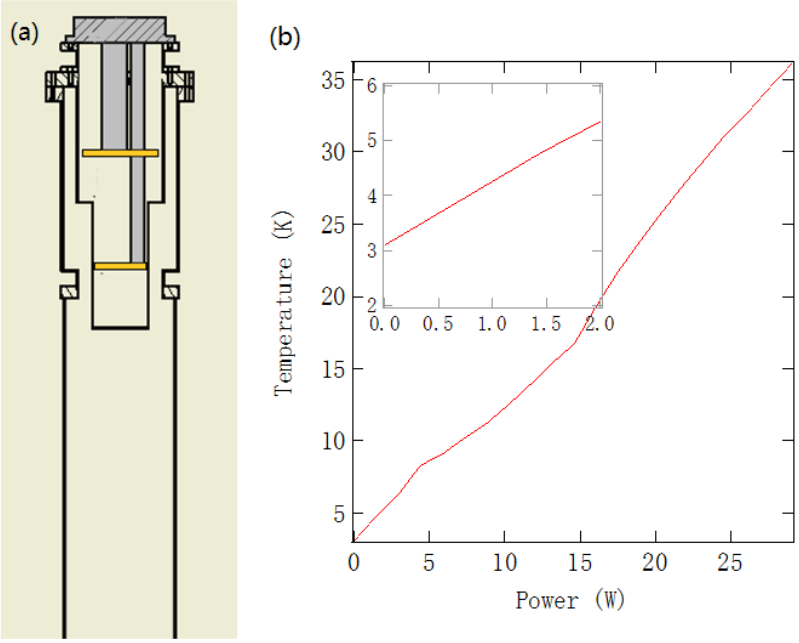

Figure 3.7 Test the cold head with shielding. (a) Experiment setup. (b) Temperature at the second stage vs power of a heater attached at the second stage. Insert: Zoom in of the 0 - 2 W heater power area.

lowest temperature on the sample is stable at ∼3.8 K, below the temperature of LHe, because second stage provides dribble of liquid He already cooled to 2.7 K. At the 250th minute of the test, we started pumping helium from the inner cylinder as shown in Figure 3.8b. The sample temperature went down to about 3 K and up again because the LHe at the bottom of the cold finger all evaporated after that time. At this point, we added more helium to the inner cylinder. After the temperature became stable, we started pumping again. This time the sample temperature went to 1.73 K. The temperatures at the second stage, first stage and extra shielding are 3.84, 37.01, 58.70 K, respectively. Pump cooling lasts for approximately 60 minutes. If we add sufficient helium gas to the inner cylinder before pumping or directly add LHe during pumping, we can produce sufficient amount of LHe to last throughout for one ARPES experiment, which is about one day.

The future work of the cold finger would be machining the sample holder from copper, because copper is a nonmagnetic material and has high thermal conductivity. The next step

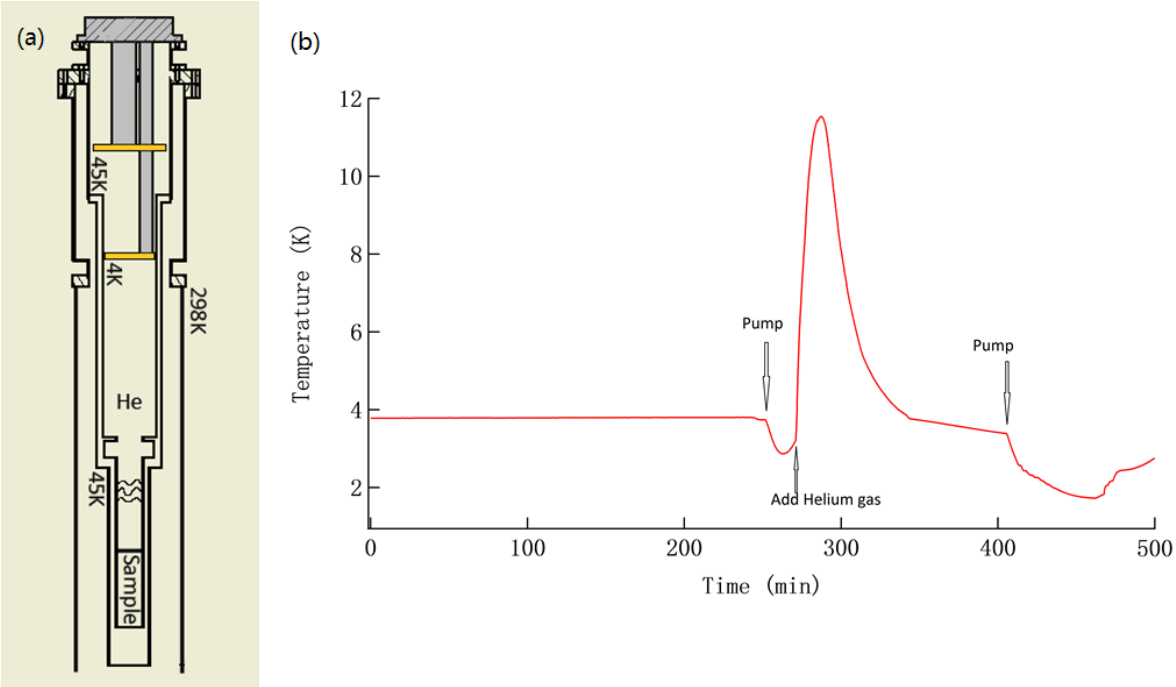

Figure 3.8 Test of the cold head. (a) Experiment setup. (b) Cooling curve.

would be testing the fully assembled cold finger and install it in the laser ARPES system. Figure 3.9 shows a sectional drawing of the sample holder.

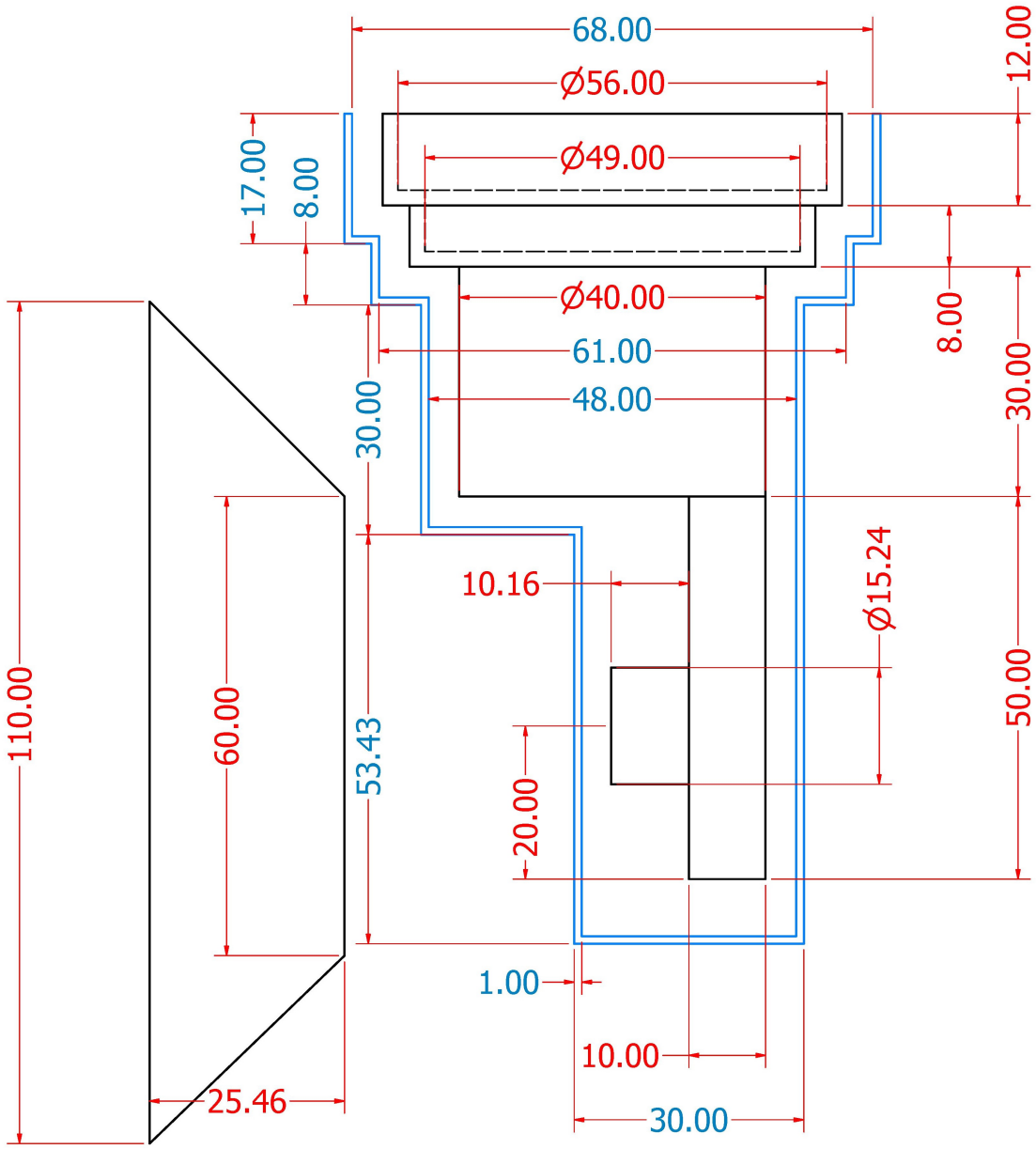

Figure 3.9 Sectional view of the sample holder at the bottom of the cold finger. The trapezoid on the left side is projection of the lens of the electron analyzer. Blue lines are the shielding for the holder.

CHAPTER 4. MAGNETIC NANO-DOMAINS IN NEODYMIUM IRON BORON

A paper published in *Physics Review B* [38]

L. Huang, V. Taufour, T. N. Lamichhane, B. Schrunk, S. L. Bud'ko, P. C. Canfield, and A. Kaminski

4.1 Introduction

In 1982, General Motors and Sumitomo Special Metals developed Neodymium iron boron ($Nd_2Fe_{14}B$). It is one of the most popular magnetic materials for advanced applications, such as a variety of devices ranging from actuators, high capacity hard drives, to lightweight, high efficiency electric motors for cars. $Nd_2Fe_{14}B$ is one of the strongest permanent magnets known. During the past three decades, significant research effort was devoted to study its properties. However, neodymium (Nd) is a rare earth element. In other words, it is dispersed and costly to extract from the earth's crust [39]. For security, environmental and economic reasons, more recent studies have typically focused on the development of materials with similar magnetic properties that do not require the use of rare earth elements. To accomplish this, one needs to fully understand the physical mechanisms that give rise to the unusually enhanced magnetic properties of this material. $Nd_2Fe_{14}B$ has a tetragonal lattice symmetry with 68 atoms per unit cell, as shown in Figure 4.1. The lattice constants are a = 8.80 Å, c = 12.20 Å. It has a Curie temperature of 565 K [12, 40] and a spin-reorientation temperature of T_{SR} = 135 K [41, 12]. Between these temperatures, its magnetic moment is aligned along the c-axis. Below 135 K the alignment depends on temperature. At 4 K, the magnetic moment has an angle of about 30 ° from the c-axis toward the [110] direction [12].

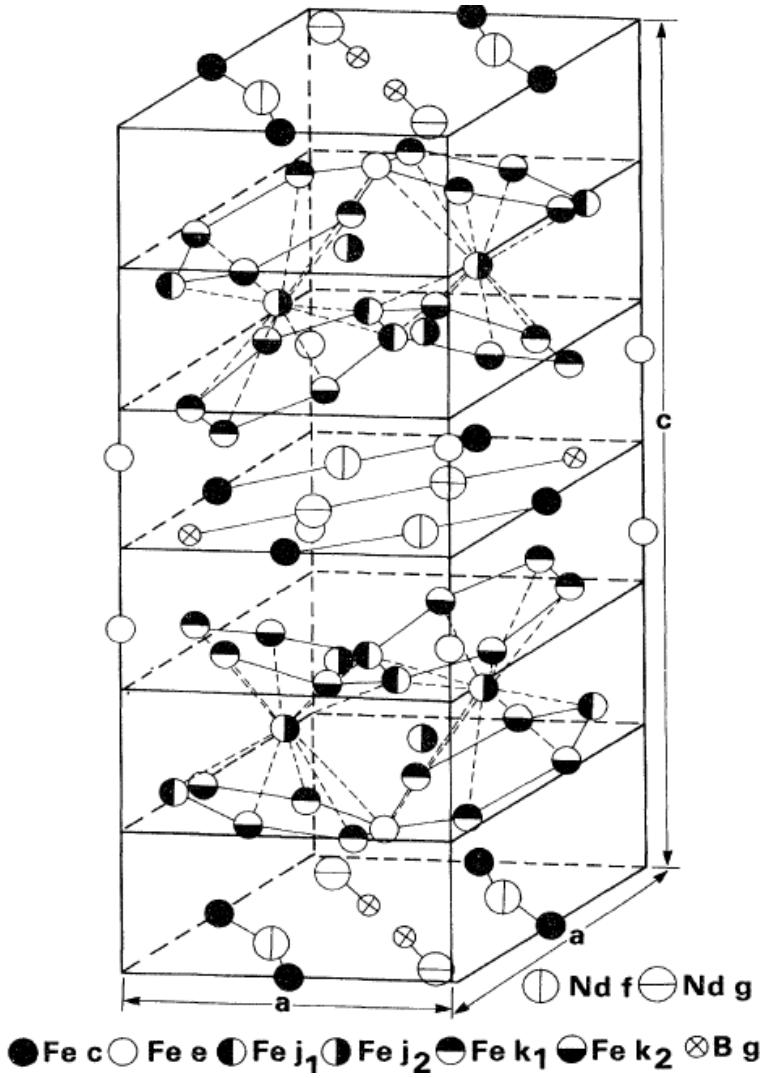

Figure 4.1 Tetragonal unit cell of $Nd_2Fe_{14}B$. The c/a ratio is exaggerated to emphasize the puckering of the hexagonal iron nets. [12]

The magnetic domain structure of $Nd_2Fe_{14}B$ has been studied by Lorentz transmission electron microscopy (TEM) and magnetic force microscopy (MFM) in thin film and polycrystalline samples [42, 43, 44, 45]. Electron microscopy [46, 47], Kerr optical microscopy, small angle neutron scattering [13] and MFM [48] studies have been completed also by using single crystals. These studies reveal the magnetic structure consists of intriguing fractal patterns that depend on sample treatment and temperature [13, 48, 49]. Previous MFM and small angle scattering studies indicated the presence of an even smaller, sub-domain magnetic structure with a typical length scale of 25–100 nm. At room temperature, the microscopic magnetic domains

form a star-like pattern, while at ∼100 K (well below T_{SR}), they become rectangular in shape as shown in Figure 4.2. In both temperature regimes, the magnetic domains are arranged in chains [13]. A detailed study of the magnetic domains in this material is interesting from a fundamental physics point view as well as practical applications. In Section 4.3, we discuss the morphology of the nano-domains in detail by using high resolution MFM. We find the star structure present at room temperature is formed from a complicated network of elongated domains with typical widths of 20 nm. The domain walls are even thinner with a width limited by our experimental resolution of 2 nm.

4.1.1 Magnetic domain theory

To explain the very large (∼1000 Gauss) magnetization of a ferromagnetic material acquired by applying a very small magnetic field (∼0.01 oersteds), French physicist Pierre-Ernest Weiss purposed the existence of magnetic domains in ferromagnetic materials [50]. A magnetic domain is a region where the magnetization is saturated. In other words, all magnetic moments of the atoms are aligned in the same direction in the magnetic domain. Different magnetic domains may have magnetization in different directions as shown in Figure 4.3 b and c. Strong magnets have most of their magnetic domains aligned in the same direction. Above a certain temperature (Curie temperature) ferromagnetic materials will lose their magnetism and domain structure, and become a paramagnet (Figure 4.3 a). The regions separating magnetic domains are called domain walls, where the direction of magnetization changes gradually from one magnetic domain to the other. The magnetic domain structure is responsible for the magnetic behavior of ferromagnetic and ferrimagnetic materials.

Magnetic domain structures are direct result of the minimization of total energy, including exchange, anisotropy, magnetoelastic, and magnetic energy of a ferromagnetic body. We will describe these energies qualitatively. Kittel [51] provides a detailed mathematical description of these energies. Exchange energy arises due to interaction between spins of two electrons, wavefunctions and Coulomb repulsion. Two electrons have the lowest exchange energy when their spins are aligned parallel, and they have the highest exchange energy when the spins are in opposite directions. Anisotropy energy is also called magnetocrystalline energy. It results from

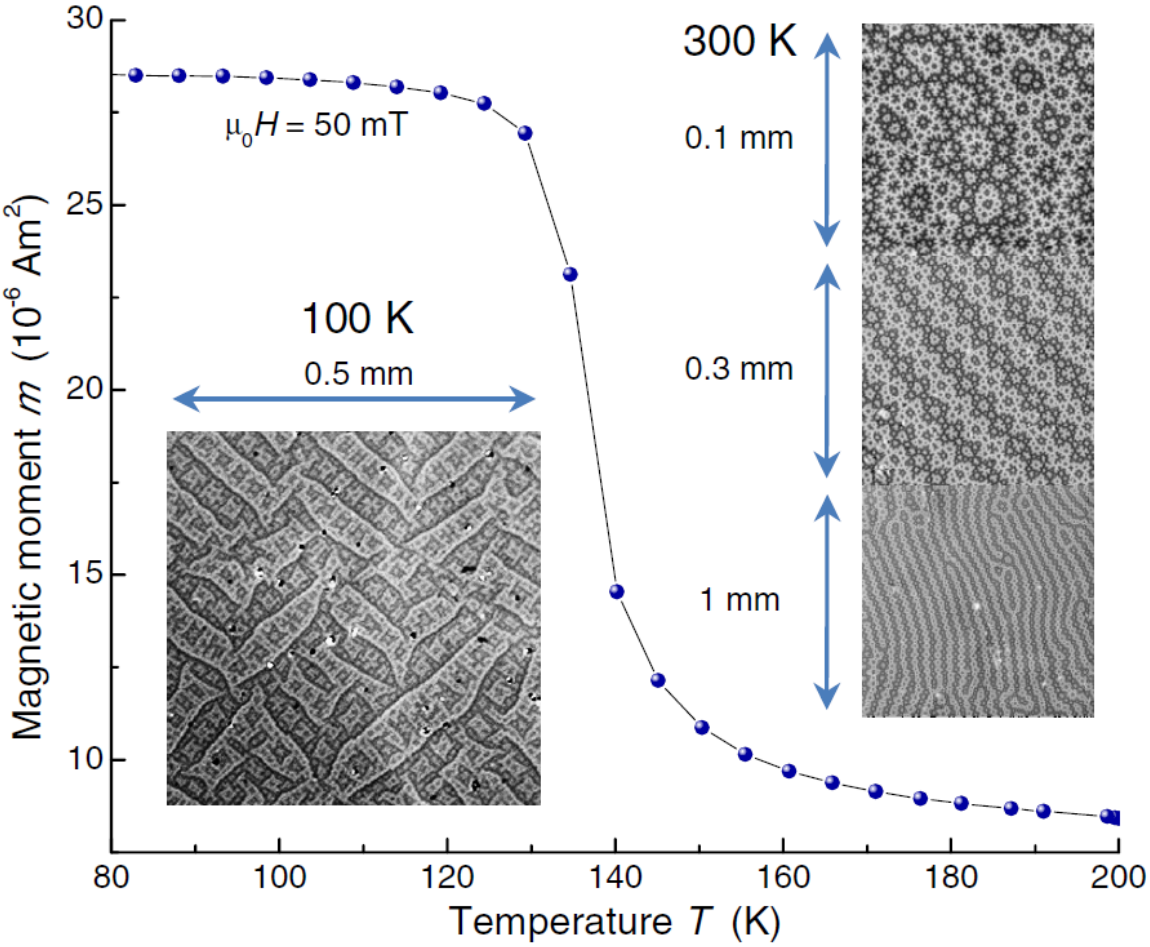

Figure 4.2 (color online). Temperature-dependence of the magnetization and the magnetic domain patterns in the $Nd_2Fe^{11}_{14}B$ single crystal. The magnetization was measured at μ_0H = 50 mT applied along the c-axis. The magnetic domain patterns were imaged exploiting the magneto-optical polar Kerr effect at a surface perpendicular to the c-direction and with the a-direction vertical. [13]

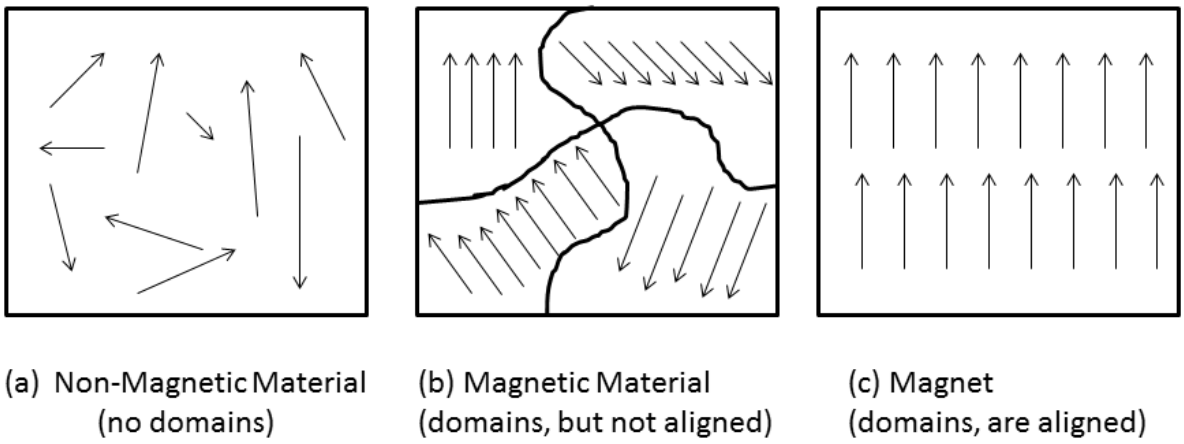

Figure 4.3 Magnetic domains.

the fact magnetization of certain crystal tends to align in a given direction (easy direction) and is more difficult to align in another direction (hard direction). The amount of energy required to align the magnetic moment in the hard direction is called anisotropy energy. The magnetoelastic energy results from the interactions between magnetization and mechanical strain of the crystal lattice. When the lattice is not deformed (no strain), the magnetoelastic energy is zero. Finally, the magnetostatic energy is the interaction between the magnet and magnetic field, including the external magnetic and its field. The magnitude of this energy is equal to the work required for the magnetic poles to exist counter to the external magnetic field if the material is not a strong magnetic or counter to the internal magnetic field (diamagnetic field), if the material is ferromagnetic.

There are two types of magnetic domain walls, Bloch wall and Nel wall. Both are an interface separating magnetic domains in which the magnetic moments change gradually from the direction of magnetization in one domain to another. The difference between these two types of walls is shown in Figure 4.4. In a Bloch wall, the magnetization rotates through the plane of the domain wall, while in a Nel wall it rotates within the plane of the domain wall. Bloch walls are the common magnetic domain wall type in bulk materials, while Nel walls appear mostly in thin film where the exchange length is very large compared to the thickness of the film. Lilley defines “very large” [52]. In our experiment we measure a sample thickness

of ∼1mm while the domain wall thickness is on the order of nanometers. Therefore, the walls are Bloch walls.

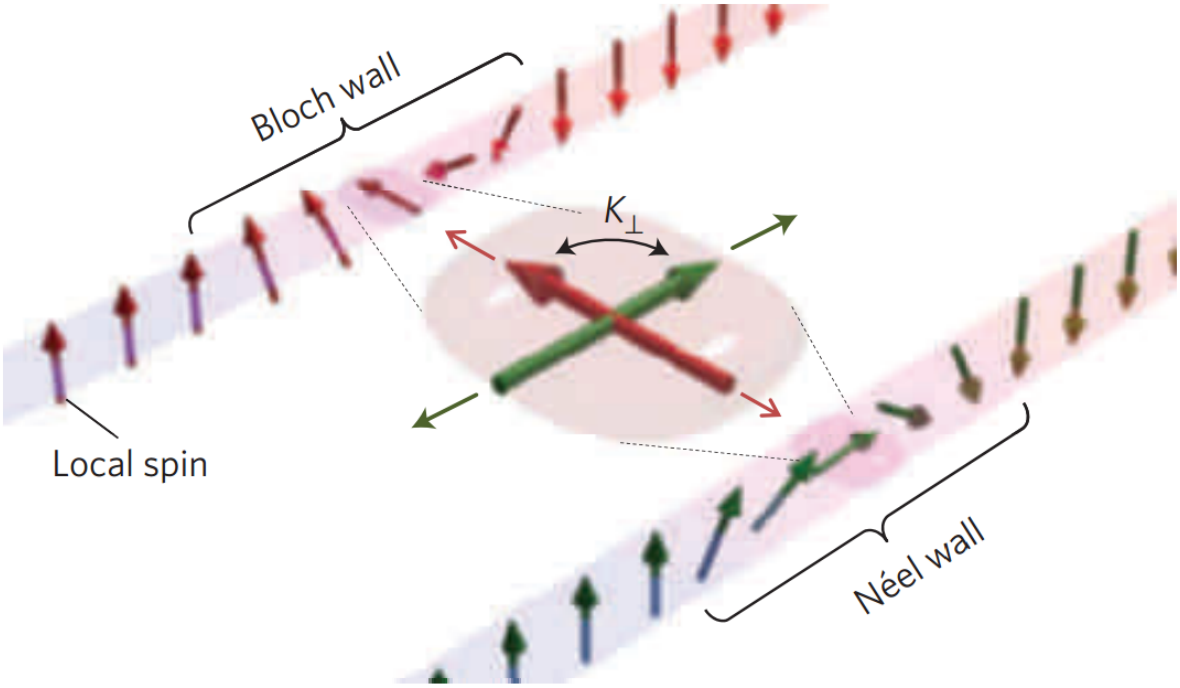

Figure 4.4 Schematic of the Bloch and Nel domain wall. [14]

4.1.2 Atomic force microscopy

Scanning probe microscopy (SPM) is a branch of microscopy that forms images of surfaces using a physical probe to scan the specimen. SPM, in general, has very high resolution, but varies from technique-to-technique. There are many types of SPMs. Among these, atomic force microscopy (AFM) and scanning tunneling microscopy (STM) are the most commonly used for measuring topology of a sample's surface. An AFM resolution could be better than an angstrom vertically [53], which allows people to distinguish a single atom on the surface of a given sample. The mechanism for an AFM is shown in Figure 4.5 a. The AFM tip is either in contact or very close to the sample's surface, located at the end of a bendable cantilever. The atomic force between tip and sample surface is determined by their distance and measured by the displacement of the cantilever (Figure 4.5 b). The cantilever displacement also changes

the direction of reflected laser beam that can be measured by position sensitive detector. By moving the tip across the area of interest on the sample's surface, one can obtain the surface topology of this area.

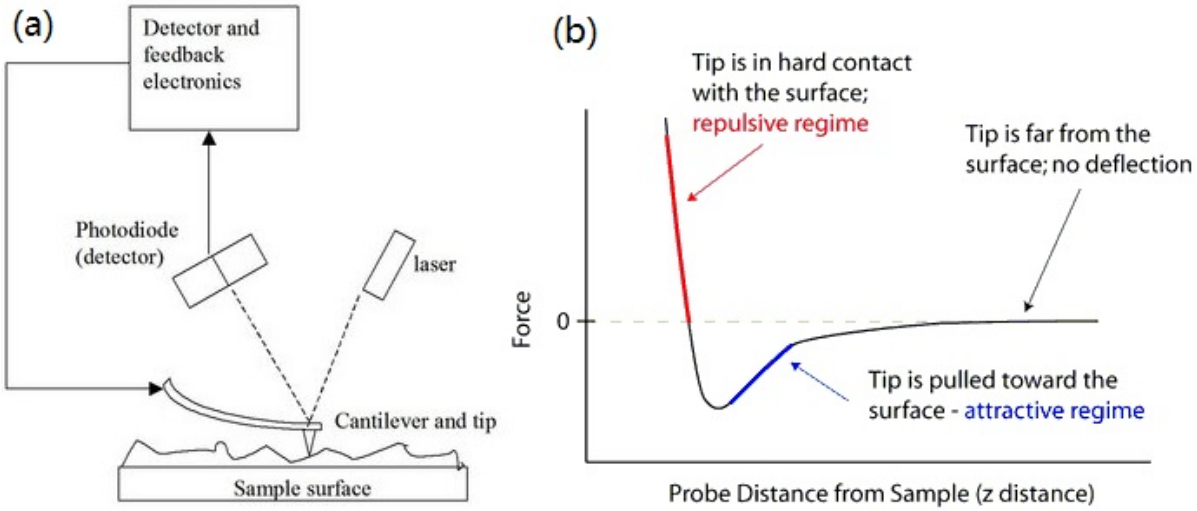

Figure 4.5 (a) Block diagram of atomic-force microscope using beam deflection detection [15]. (b) The relation between atomic force and distance between atoms [16].

The AFM can scan at constant force or constant height. If it scans at constant force, a feedback loop in the AFM is switched on to adjust the height of the tip to keep the force between tip and sample at constant value. Height of the tip is recorded to represent the sample's surface topology. The image is often referred to as a topographic image. When the feedback loop adjusts the tip height, its performance depends upon the amplitude of height change (called "feedback gain") and the scan speed. There is optimal value of the feedback gain that produces the best image. Either too large or too small gain results in an image not reflecting the topology of the sample. In worst case, this could damage the AFM tip. For scans at constant tip height, the z-position of the tip and sample are fixed. Instead of recording the z-position of the tip, the force between tip and sample surface, the displacement of the laser beam on the photodiode is recorded. This image is often referred to as constant height image. The advantage of constant height image is it does not depend on feedback loop performance. However, for samples not very flat, i.e., the sample surface height range covers more than the

entire red and blue area in Figure 4.5 b, the AFM tip often extends into the sample, and the force between sample and tip becomes too large to measure, sometimes even breaks the tip. Therefore, constant force scans are utilized more frequently.

There are various operation modes for AFM, such as contact, non-contact, dynamic force, force modulation, and phase imaging modes. In contact mode, the tip touches the sample during the scan and the scan is completed with constant force. Non-contact mode belongs to a family of AC modes — an oscillating cantilever is used in this mode. The tip of the cantilever is in attractive regime as shown in Figure 4.5 b. It is quite close to the sample, but not touching. The topology of the sample is measured, based on the changes of resonant frequency or amplitude of the cantilever. In our experiment, we only use these modes. Details of other operation modes are found in Emtsev et al. [16].

4.1.3 Magnetic force microscope

MFM is a variation of AFM technique. The main difference is the origin of the interaction between tip and sample. One is atomic force and the other is magnetic force. Instead of using a regular AFM tip, the MFM tip is magnetized. The magnetic force between tip and sample is [54]:

$$\vec{F} = \mu_0(\vec{m} \cdot \nabla)\vec{H}, \tag{4.1}$$

where $\mu_0 = 4\pi \cdot 10^{-7} N/A^2$ is the magnetic permeability in a vacuum, $\vec{m}$ is the magnetic moment of the tip and $\vec{H}$ is the magnetic stray field from the sample surface.

Of course, we could place the tip near the sample's surface and measure the displacement of the tip as we did for AFM. However, there is another, far more sensitive operation mode for measuring the magnetic field at the sample's surface — the dynamic mode. In this mode, the tip and cantilever vibrate at a resonant frequency given by

$$\omega_0 = \sqrt{\frac{k}{m}}, \tag{4.2}$$

where k is the force constant for the cantilever and m is the effective mass for the cantilever and tip. Under the magnetic force, $\vec{F}$, between tip and sample, this resonant frequency will shift [55]:

$$\omega = \omega_0 \sqrt{1 - \frac{1}{k}\frac{\partial F}{\partial z}}, \tag{4.3}$$

where z is a vertical position and also the same direction the cantilever is vibrating. Therefore, the shift in resonant frequency is provided by

$$\Delta f = f - f_0 \approx -\frac{f_0}{2k}\frac{\partial F}{\partial z}, f = \frac{\omega}{2\pi}. \tag{4.4}$$

A laser deflection sensor, like the one in AFM, detects this shift in frequency. From the change of this frequency, we can calculate the derivative of the magnetic force with respect to the z-direction and then calculate the gradient of the magnetic field at the sample's surface according to Eq. 4.1.

4.2 Methods

The $Nd_2Fe_{14}B$ crystals were grown out of a Nd-rich ternary melt as in ref [47, 13] using a 3-cap, Ta crucible [56]. The starting composition of $Nd_{53}Fe_{45}B_2$ was placed, in elemental form, in the crucible and heated to 1175 °C then it was cooled over 105 hours to 800 °C. At this stage, the excess liquid was separated from the plate-like single crystals.

The as-grown, single crystals have flat, shiny facets of nearly optical quality. However, a thin layer of flux binds small particulates with a significant surface density. These particulates interfere with the cantilever and often produce extrinsic magnetic gradients that obscure the MFM signal. To avoid this problem single crystals with a typical size of 5 - 10 mm were cut to 1 mm thin slices by a low speed diamond wheel. Their surfaces were carefully mechanically polished using powered alumina with decreasing grain size from 10 to 0.05 μm yielding a typical surface roughness that is better than 10 nm. After polishing the sample surface was cleaned with acetone and ethanol and mounted on the sample plate. The measurements were carried out using a Variable Temperature, UHV Scanning Probe Microscope made by Omicron. The

surface topography was measured using a non-magnetic AFM cantilever in non-contact mode with a force constant of 42 N/m, resonance frequency of 320 kHz and reference frequency of 511 kHz. The magnetic structure at the $Nd_2Fe_{14}B$ surface was measured using a super sharp silicone, high resolution MFM tip, which has a layer of hard magnetic coating with coercivity of approximately 125 Oe and a remanence magnetization of approximately 80 emu/cm^3 (SSS-QMFMR made by Nano-world). The tip has a force constant of 2.8 N/m and a radius that is less than 15 nm. The force that acts on the magnetized tip is detected as described in the MFM section. The change in frequency of the cantilever oscillation is therefore a measure of the magnetic field gradient at a given point.

To estimate the roughness of the surface, we imaged the topography of the sample surface using a non-magnetic tip in non-contact mode as shown in Figure 4.6. The measurement is performed with the tip traveling very close (a few angstroms) to the sample surface. The roughness of the surface after polishing is approximately 18 nm and all features are very irregular. Since the magnetic imaging is performed at a much larger tip to surface distance (100's of nanometers) this level of sample roughness does not significantly affect our measurements.

4.3 Results And Discussion

Figure 4.7 shows the magnetic domain structure of $Nd_2Fe_{14}B$ measured using the magnetic AFM tip in non-contact mode at a tip-surface distance of 300 nm. Several interesting features are clearly visible. There are fairly weak, long and wavy domain walls that have been reported by previous MFM experiments [48], indicated by arrows in Figure 4.7. The most pronounced features are star-like domains that are several μm across and these were previously observed via Kerr optical microscopy [13] (See Figure 4.2). With our enhanced resolution we can also see that the star shape object are not single domains. Instead, they consist of a very complex network of much smaller, elongated magnetic nano domains seen as a pattern of thin brown lines in the yellow background of Figure 4.7 top and a very sharp series of dips in the profile shown in Figure 4.7 bottom.

In Figure 4.8 we demonstrate how the imaging of the magnetic domains depends on the sample-tip distance (scan height). At hight separation (e.g. 500 nm), the magnetic field from a

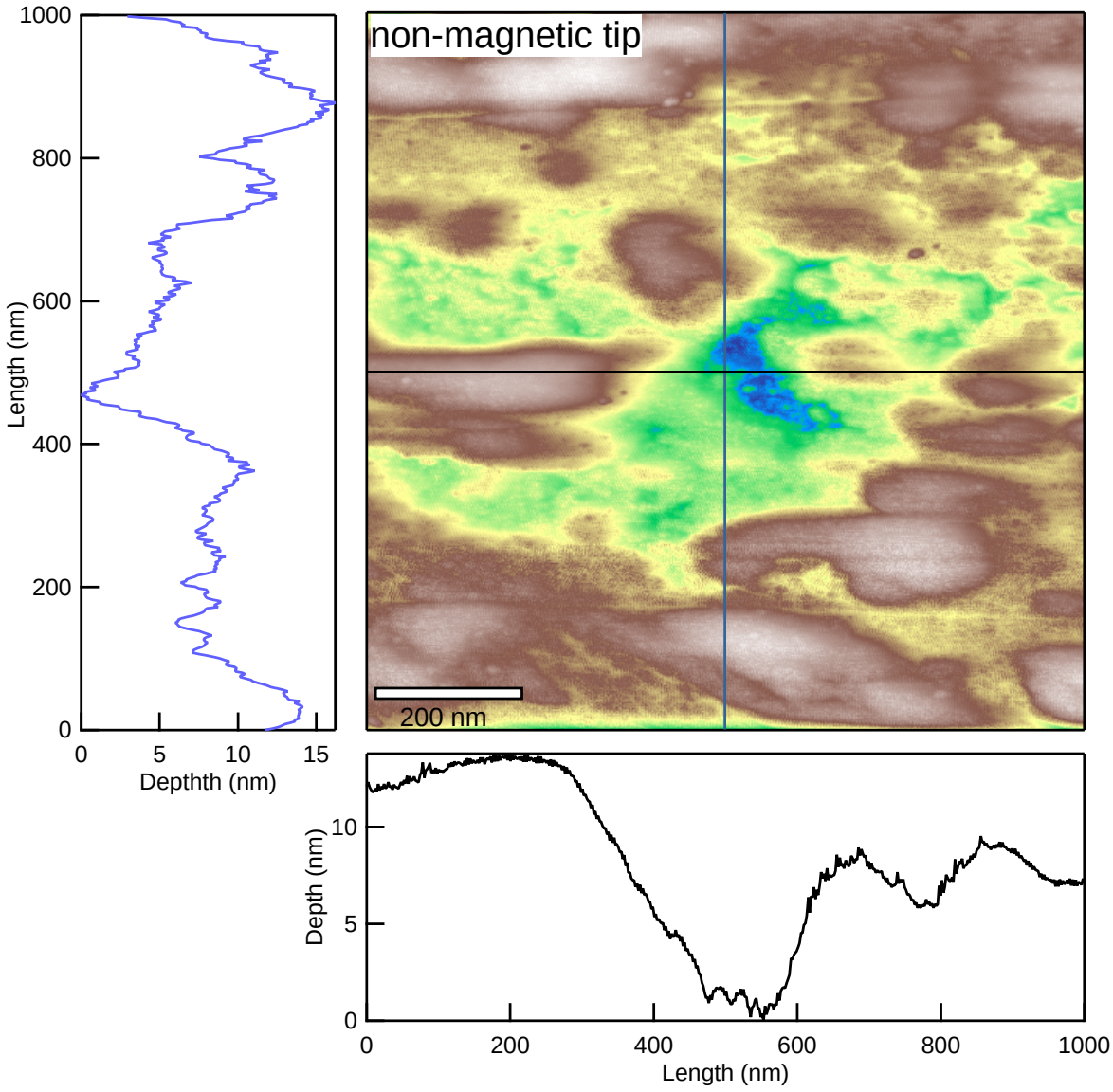

Figure 4.6 (color online). Main: The surface topographic image of $Nd_2Fe_{14}B$, non-magnetic signal scanned by the AFM Non-contact-tip, z mode. 1 μm $\times$ 1 μm scan, the z range is 18 nm. Left: The z-profile along the vertical line in main. Bottom: The z-profile along the horizontal line in main.

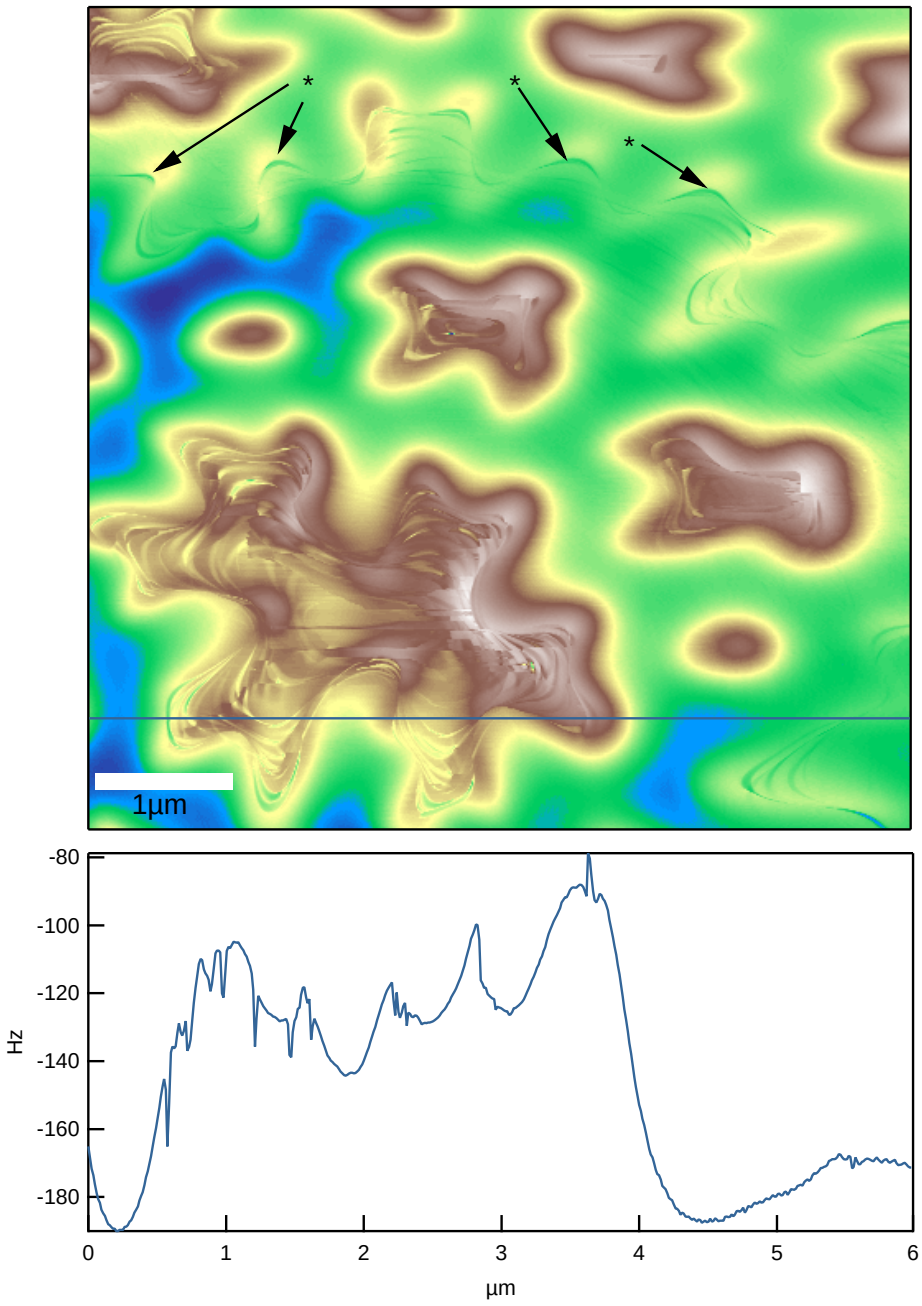

Figure 4.7 (color online). Top: A 6 μm $\times$ 6 μm magnetic frequency shift image of the surface of $Nd_2Fe_{14}B$. Bottom: The z-profile of the blue line in the top graph. Scan height: 300 nm.

large number of domains averages out, producing a smooth pattern of star-shaped objects that are a few μm across and similar to Kerr optical imaging in Figure 4.2. When the sample-tip distance is reduced, the magnetic field averaging effects are weaker and the tip begins to react to the presence of nano-size domains. This is best illustrated by following the evolution of the large domain in the upper left corner of each graph. 560 nm above the surface, this looks like a nice smooth single domain with round edges. At 410 nm, the tip begins to detect a variation of the magnetic field at the center of this object. At even smaller tip-surface separations (e.g. 220 nm), it is clear that this is not a single domain, instead it consists of fine network of nano-scale domains. This is shown in more detail in Figure 4.9, where we focus on smaller area of the sample and part of a single micro domain. We can see that the overall shape of the micro domain is roughly similar, but a smaller surface-tip distance reveals a larger number of nano-domains. While certain, large features are visible for all three sample-tip separation, such as the wavy, yellow-brown edges of the star-shaped domains, others only appear at smaller scan heights. We can confirm that all micro domains look smooth and uniform at large scan heights. The smooth appearance of the star-shaped domains at large scan heights is simply a result of an averaging of the magnetic field away from the sample surface. At smaller scan heights, more and more nano-domains are revealed. Another expected feature is observed by comparing the first two and last scans in Figure 4.9. At large tip-sample distances, all the features are reproducible. Closer distances reveal finer detail, but the existing features are not modified. This is in contrast with small scan heights, where at 200 nm, we observe that some features are significantly modified, while other remain unchanged. This is most likely a result of the magnetic field from the tip affecting the domain in the sample. This unwelcome phenomenon imposes a limit on the details that can be revealed by this technique. The impact of the movement of the magnetic tip on the scanned image is shown in Figure 4.10. The movement of the tip during data collection is marked in the left bottom corner of each image. The overall magnetic domains (the green and brown areas) are unchanged regardless the direction of the tip movement, while the positions of the nano-domains are slightly different. However, the size and shape of the nano domains remain the same.

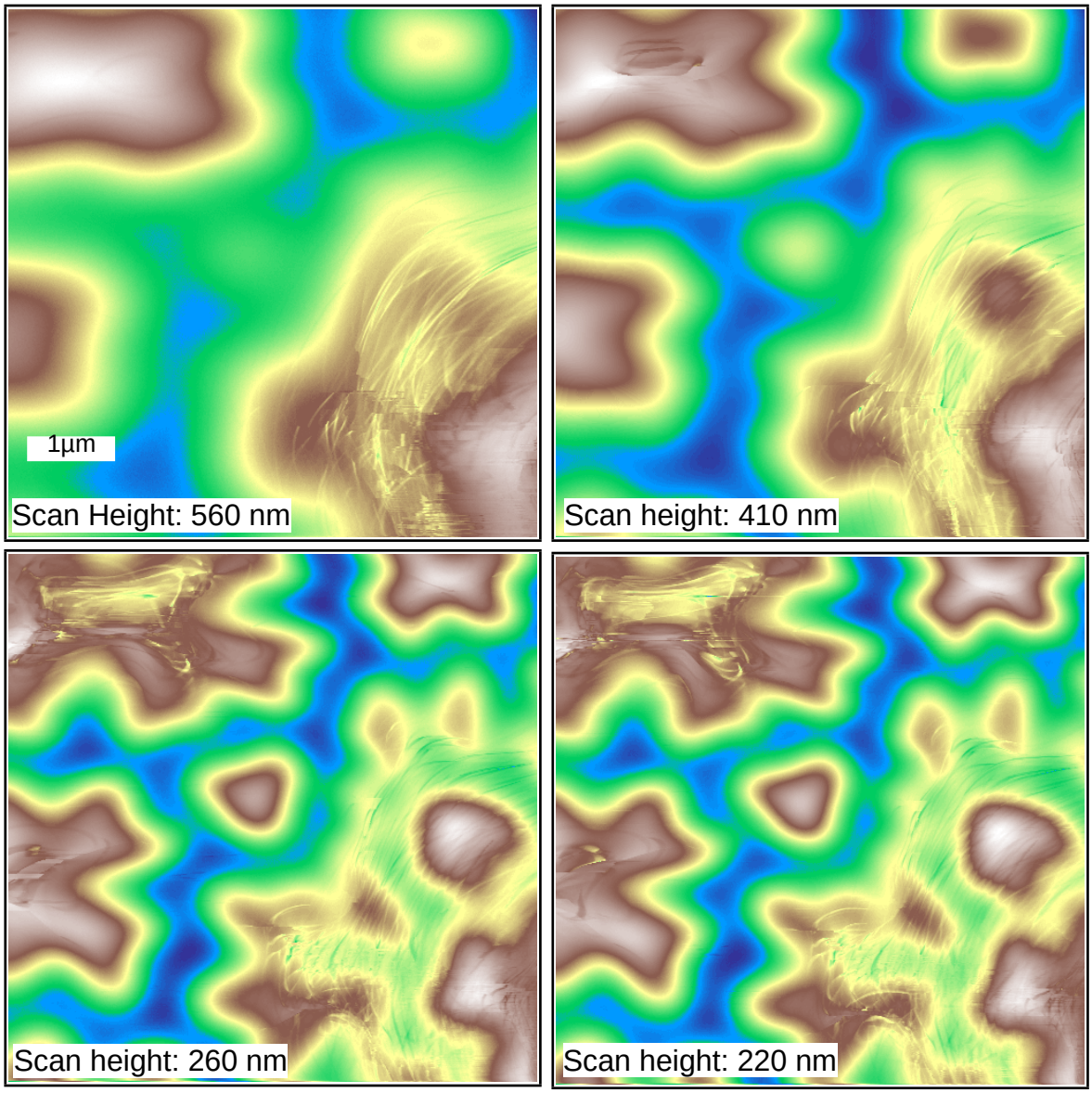

Figure 4.8 (color online). The same position on the sample is scanned at different tip-sample distances (6 μm $\times$ 6 μm; And scan heights are (From left top to right bottom) 560 nm, 410 nm, 260 nm and 220 nm, respectively).

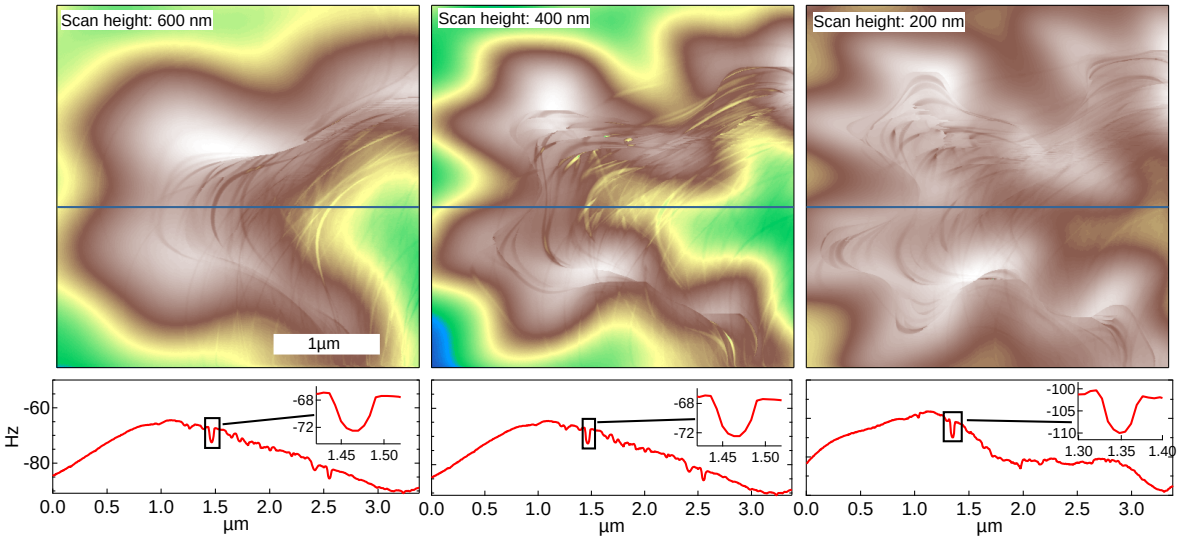

Figure 4.9 (color online). Top: The same position on the sample is scanned at a different tip-sample distance (6 μm $\times$ 6 μm). Bottom: The z-profile of the blue line in the upper graphs and a zoom-in of the boxed area in the profile. Scan heights: (From left to right) 600nm, 400nm, 200nm.

We now examine the properties of the nano domains in detail. In Figure 4.11 (a) we show the wide area scan of several star-shaped domains. We then focus on a smaller area that contains just a single object then we select a very small 200 nm $\times$ 200 nm area shown in Figure 4.11 (d). This shows three domains separated by areas of lower value of magnetic gradient seen as green / blue. Those features are very sharp even on tens of nanometers scale. We extract thress cuts and examine the spatial variation of the cantilever frequency as a function of position along direction perpendicular to the direction of the domain walls. Those profiles are shown in Figure 4.11 (e). The domain in the center is very narrow with width 10 nm. The low gradient areas separating the domains are slightly wider - about 20 nm across. To obtain information about the limits on the thickness of the domain walls we calculate the derivative of the profiles from Figure 4.11 (e) and plot these in panel (f). While the peaks do not have an exact Gaussian shape, an approximate fit yields widths of between 2 - 4 nm, which most likely reflects the spatial resolution of our instrument.

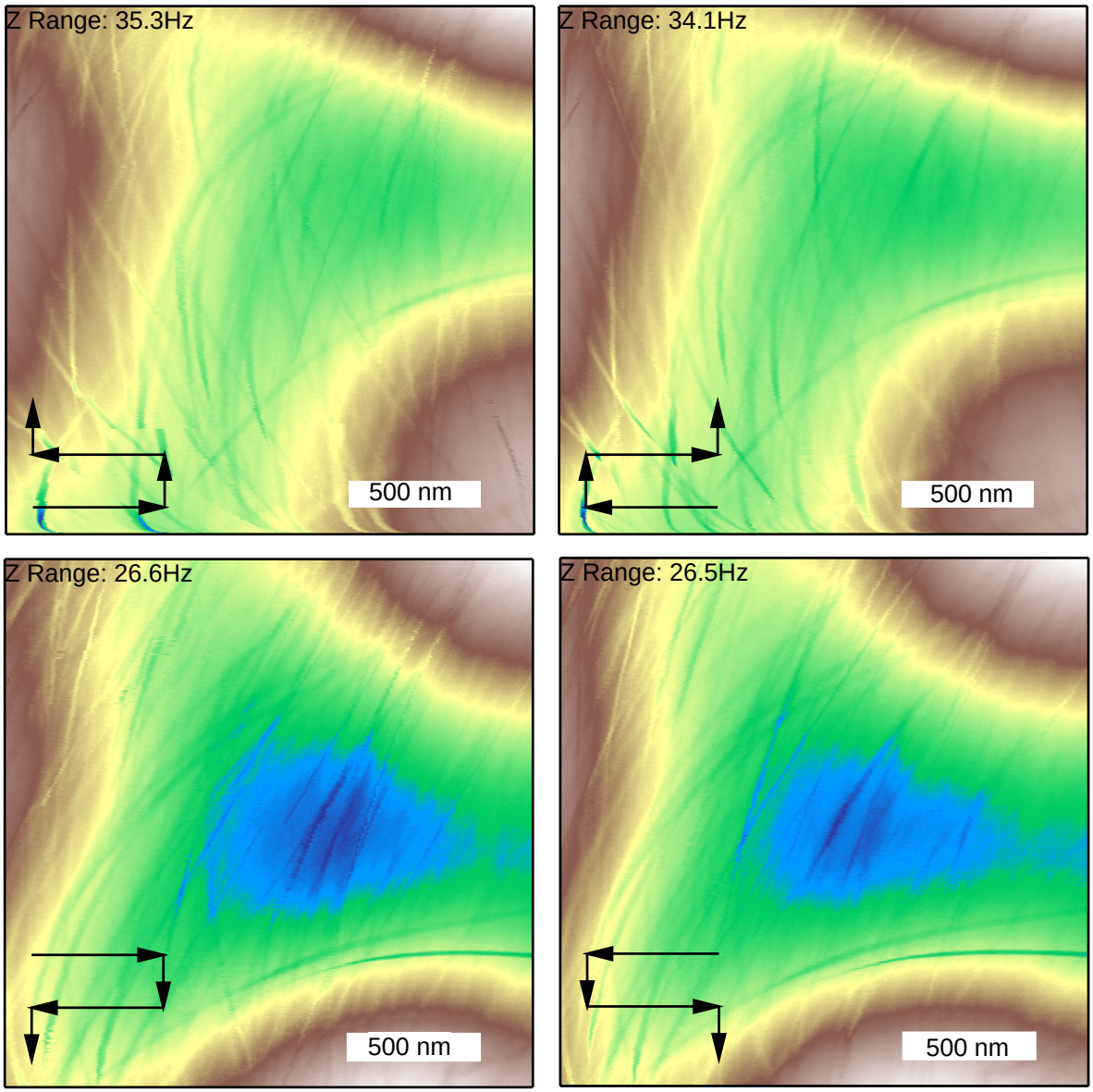

Figure 4.10 (color online). The 2μm $\times$ 2μm scans at the same position but different tip movements (marked in each graph). Scan Height: 500 nm.

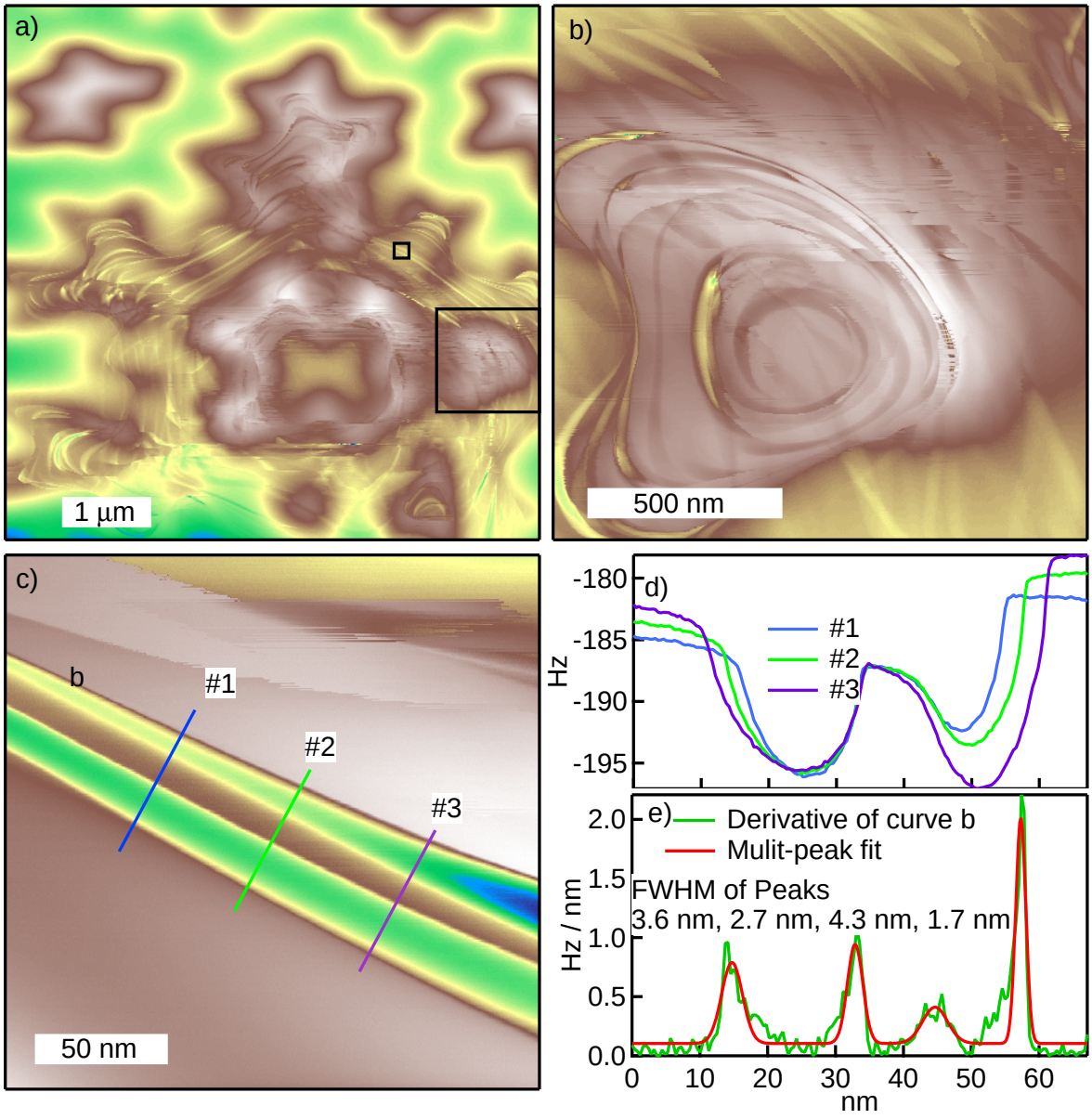

Figure 4.11 (color online). (a) A frequency shift image (6 μm $\times$ 5.5 μm) measured using magnetic tip 300 nm above the surface of $Nd_2Fe_{14}B$. (b) A zoom-in from the larger box area marked in (a) (scanned area 1.37 μm $\times$ 1.37 μm). (c) A zoom-in from the smaller box area marked in (a) (scanned area 200 nm $\times$ 200 nm). (d) The z-profile along the three cuts indicated in (c). (e) The derivative of the curve #2 in graph (d) and multi-peak fit.

The shape of the magnetic nano-domains and thickness of the domain walls are results from the minimizing of magnetic total energy, including wall energy, surface energy of closure, and magnetostatic energy [57]. The anisotropy energy of the main domain depends on the direction of its magnetic moment. And it is high when the magnetic moment is close to c direction while it is low when the magnetic moment is close to a or b direction. Larger anisotropy energy results in a thinner domain wall [51]. This is the reason to the fact that the domain walls between the main domains (i.e. domain walls between the brown and blue areas in Figure 4.8) are thicker and the domain walls between sub-domains in the star-shaped main domain are thinner. Since the direction of the nano-domain structures is parallel to edges of the star-shaped areas, its elongated shape must be a result of the shape of the star edges. This shape, which is also called a "branched state" [58], could significantly reduce the magnetostatic energy density very close to the surface [59]. However, the fundamental origin of the nano domains is still not clear and further theoretical analysis needs to be introduced.

4.4 Conclusions

We have studied the domain structure of $Nd_2Fe_{14}B$ using high resolution MFM. In addition to previously observed long, wavy nano-domains [48], we find that a star structure present at room temperature is formed from a complicated network of elongated (although much shorter) domains with typical widths of 20 nm and a resolution-limited domain wall that is thinner than 2 nm. We also found that most domains imaged at modest sample-tip distances are insensitive to the perturbation created by the magnetic tip. At smaller distances, however, a number of these domains change their appearance, which sets a limit on the experimental ability to measure their properties. Despite this, we show an excellent instrumental resolution (better than 2 nm) and an imaging of magnetic features that can be achieved even at moderate scan heights. The shape of the magnetic nano-domains and thickness of the domain walls are results from the minimizing of magnetic total energy, and detailed theoretical analysis is needed in the future.

This research was supported by the US Department of Energy, Office of Basic Energy Sciences, Division of Materials Sciences and Engineering (data acquisition and analysis). P. C.

C., T. N. L and V. T. acknowledge support from the Critical Materials Institute, an Energy Innovation Hub funded by the U.S. Department of Energy, Office of Energy Efficiency and Renewable Energy, Advanced Manufacturing Office (sample growth). Ames Laboratory is operated for the US Department of Energy by the Iowa State University under Contract No. DE-AC02-07CH11358.

CHAPTER 5. THE EFFECTS OF MOIRÉ LATTICE ON THE ELECTRONIC PROPERTIES OF GRAPHENE

A paper to be submitted to *Physics Review B*

L. Huang, Y. Wu, M. Hershberger, D. Mou, M. Tringides, M. Hupalo, and A. Kaminski

5.1 Introduction

Graphene is an allotrope of carbon in the form of a single layer, two-dimensional, hexagonal lattice in which one atom forms each vertex (see Figure 5.1). The lattice constants are $a_G = b_G = 2.4589$ Å. The electronic band structure of graphene could be calculated using tight banding approximation [60]:

$$c_n < \phi_n|\hat{H}|\phi_n > + \sum_m c_m < \phi_n|\hat{H}|\phi_m > e^{i\mathbf{k}\cdot\mathbf{R}} = Ec_n < \phi_n|\phi_n >, \tag{5.1}$$

where ϕ_n is the wave function at a given lattice point, m is the nearest neighbor of the point, $\mathbf{k} = (h, k, l)$ ranges through all values in the first Brillouin zone consistent with the Born-von Karman periodic boundary condition, and c is a coefficient determined later by the Schrödinger equation. For graphene, each carbon atom has three nearest neighbors located at $a_1 = (1, 0)\frac{|a_G|}{\sqrt{3}}$, $a_2 = (-\frac{1}{2}, \frac{\sqrt{3}}{2})\frac{|a_G|}{\sqrt{3}}$ and $a_3 = (-\frac{1}{2}, -\frac{\sqrt{3}}{2})\frac{|a_G|}{\sqrt{3}}$, where $|a_G| = 2.46$ Å, is the primitive lattice vector of graphene. Equation 5.1 is written as

$$\begin{aligned} c_1 < \phi_1|\hat{H}|\phi_1 > + c_2 < \phi_1|\hat{H}|\phi_2 > (e^{i\mathbf{k}a_1} + e^{i\mathbf{k}a_2} + e^{i\mathbf{k}a_3}) = Ec_1 \\ c_2 < \phi_2|\hat{H}|\phi_2 > + c_1 < \phi_2|\hat{H}|\phi_1 > (e^{i\mathbf{k}a_1} + e^{i\mathbf{k}a_2} + e^{i\mathbf{k}a_3}) = Ec_2 \end{aligned} . \tag{5.2}$$

The solution to Eqs. 5.2 is

$$E = \epsilon \pm t\sqrt{1 + 4cos(\frac{\sqrt{3}k_x a}{2})cos(\frac{k_y a}{2}) + 4cos^2(\frac{k_y a}{2})}, \tag{5.3}$$

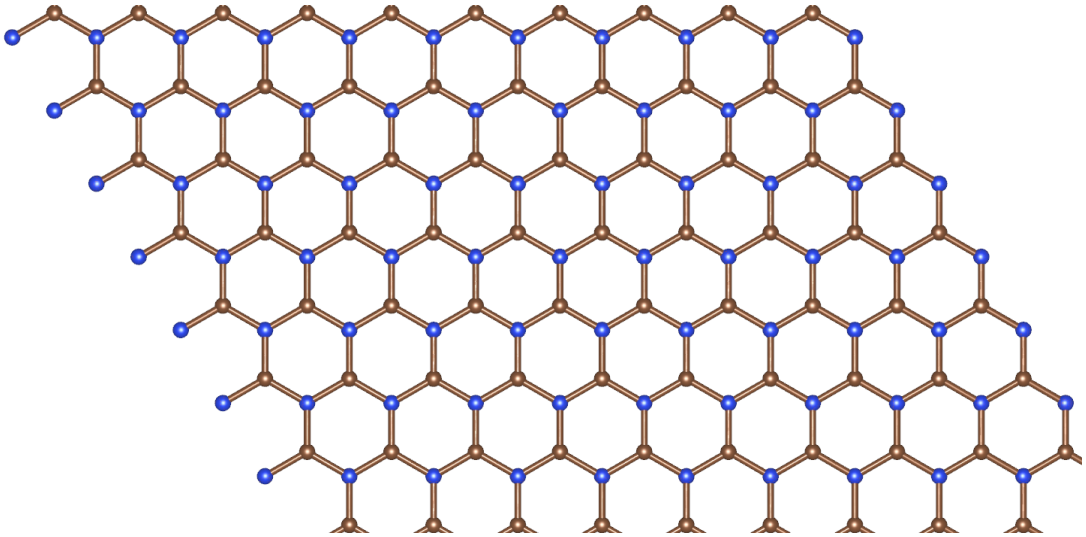

Figure 5.1 Triangular sublattices of graphene. Blue and brown atoms belong to two sublattices. Each atom in one sublattice has three nearest neighbors in the sublattice.

where $\epsilon =< \phi_1|\hat{H}|\phi_1 >=< \phi_2|\hat{H}|\phi_2 >$, and $t =< \phi_2|\hat{H}|\phi_1 >=< \phi_1|\hat{H}|\phi_2 >$, $|\phi_1$ and $|\phi_2$ are symmetric because the blue and brown atoms in Figure 5.1 are symmetric. The band dispersion relation 5.3 can be simplified to

$$E = \epsilon \pm t(1 + \pi - k_y a), \tag{5.4}$$

at $(k_x, k_y) = (0, \pi/a)$ and its six symmetric k positions in the Brillouin zone. The 2D band structure is shown in Figure 5.2. At each K point in first Brillouin zone the band dispersion is linear.

Novoselov et al. first produced graphene in the lab in 2003 [61]. They successfully prepared graphene by mechanical exfoliation of small mesas of highly oriented pyrolytic graphite. In the recent decade, graphene has become a topic of intense research because of its unique structural and electronic properties such as presence of Dirac dispersion, which leads to high thermal conductivity [62], ballistic transport [63], and ultrahigh electron mobility [64]. Graphene can be readily grown on large area insulating, semiconducting and metallic substrates. Lattice mismatch at the interface leads to formation of moiré patterns (superlattice) with longer periodicity than lattice constant. In fact this is a natural way to obtain weak periodic potentials

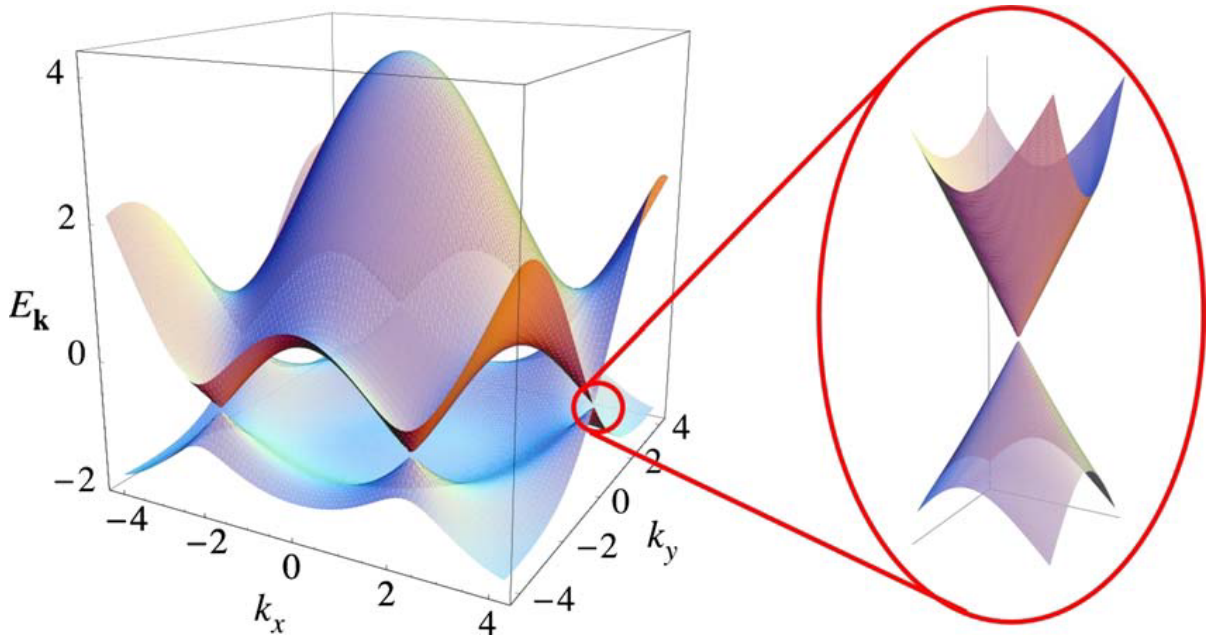

Figure 5.2 Electronic dispersion in the honeycomb lattice. Right: zoom in of the energy bands close to one of the Dirac points. [17]

with characteristic length scales of several nanometers. This effect is one of important ways to tune the graphene electronic structure and properties [65, 66, 67, 68]. Recently, tuning the size of superlattice of graphene on boron nitride substrate and measuring its fractional quantum Hall resistance lead to engineering of energy spectrum of Hofstadter butterfly [69, 70, 71, 72, 73].

Silicone carbide (SiC) is the most commonly used substrate because of its hexagonal crystal structure with lattice constant $a_{SiC} = b_{SiC} = 3.073$ Å, c = 10.053 Å. Epitaxial graphene grown by thermal annealing of SiC has been studied extensively with several complementary techniques to reveal its structural and electronic properties. These studies helped to better understand many aspects of graphene layer on SiC (ionic position, thickness uniformity, stacking, relative layer orientation and variation of the band structure with number of graphene leyers) [74, 75, 76, 77, 78, 79, 80]. However, a number of questions still remain open about the nature of the graphene-substrate interface and how it affects Dirac fermions. The layer at the interface is referred to as the buffer or zero layer graphene and shown to have no π-bands. This layer increases the carrier concentration and shifts the Femi level, without modifying the shape of the

Dirac cones [81]. Structurally, the buffer layer was represented in terms of the two coincidence lattices, which form two distinct diffraction patterns: (1) 6×6 (oriented along the SiC unit cell measured in terms of a_{SiC}) and (2) $6\sqrt{3} \times 6\sqrt{3}$ rotated 30˙ from the 6×6 unit cell, equivalent to a 13×13 unit cell (along graphene measured in terms of a_G). A new type of buffer layer was grown with linear π-bands separated by a measurable gap [82]. This study motivates the need to perform new experiments to correlate structural to electronic information, to understand and control the properties of graphene. The surface reconstruction has been studied by several techniques in the past, including LEED [74, 76, 75], Auger electron spectroscopy [74, 75], scanning tunneling microscope [75, 79] and ARPES [80, 83, 84, 85, 86, 87, 88, 89, 90, 91, 92]. Except one study [92], most of them are reporting $\sqrt{3} \times \sqrt{3}$ R30° and $6\sqrt{3} \times 6\sqrt{3}$ R30° surface reconstructions.

In this paper we report discovery of new features in the electronic structure of graphene grown on SiC substrate, namely additional replicas of the Dirac cones. The photoelectron intensity of these objects does not decrease with increasing number of graphene layers demonstrating their intrinsic origin, rather than simple photoelectron diffraction. In fact, the pattern of the band dispersion within these replica features, proves that they arise due to weak modulation of electronic potential of graphene caused by interplay of lattice periodicities, i. e. formation of moiré pattern. This explains several recent transport results and provides pathway for understanding and controlling properties of this very important material.

5.1.1 Low energy electron diffraction

We use low energy electron diffraction (LEED) to determine the super-structure of graphene grown on a SiC surface. In LEED, a collimated beam of low energy electrons (20 - 200 eV) [93] is bombarded on a single crystal (SiC-graphene) sample. The diffracted electrons are collected on a fluorescent screen as shown in Figure 5.3. LEED is an ideal tool to measure the surface structure of a well-ordered sample (single crystal). Typically, the sample is prepared in the same way as prepared for ARPES measurement. The high surface sensitivity results from the small mean free path of electrons traveling inside a material as shown in Eq. 1.29.

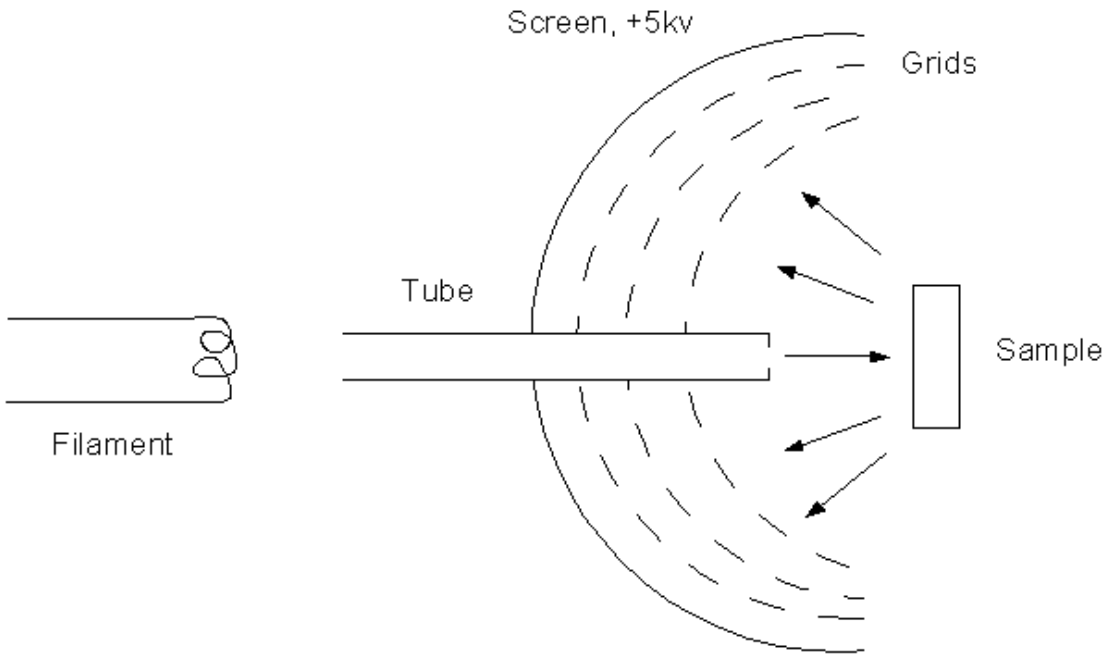

Figure 5.3 Schematic diagram of a typical LEED instrument.

In 1923, de Broglie proposed all matter can exhibit wave-like behavior [94], including electrons. Electrons have wavelength

$$\lambda_0 = \frac{h}{p_0} = \sqrt{\frac{1.5eV}{E_{kin}}}(nm), \tag{5.5}$$

and wave vector with length

$$k_0 = \frac{2\pi}{\lambda_0} = (\frac{2\pi}{h})m_e v, \tag{5.6}$$

where h is Planck's constant, m_e is electron mass, and v is electron velocity. For electrons with energy 100 eV, their wavelength is 1.2 Å, which is the same order of magnitude as crystal unit cell size. Therefore, it is ideal to probe the single crystal structure.

According to the Laue condition, the wave vector, k, of scattered electrons at constructive interference is

$$\mathbf{k} - \mathbf{k}_0 = \mathbf{G}_{hkl}, \tag{5.7}$$

where G_{hkl} is a vector of the reciprocal lattice. And, $|\mathbf{k}| = |\mathbf{k}_0|$, since we only consider elastic scattering in LEED. Also, the mean free path for low energy electrons in a crystal is on the order of angstroms, which means only the first few surface layers contribute to the diffraction. There are no diffraction conditions in the direction perpendicular to the sample's surface. In this case Eq. 5.7 can be reduced to

$$\mathbf{k}^{\|} - \mathbf{k}_0^{\|} = \mathbf{G}_{hk}, \tag{5.8}$$

where $\mathbf{k}^{\|}$ and $\mathbf{k}_0^{\|}$ are the parallel components to sample's surface of the reflected and incident wave vectors. For a normal incident beam of electrons, as shown in Figure 5.3, $\mathbf{k}_0^{\|} = 0$ and $\mathbf{k}^{\|} = \mathbf{G}_{hk}$ is independent of the incident electron energy. Each constructive interference point on the screen represents a reciprocal lattice point of the sample's surface. In the elastic back scattering process, the total energy of an electron is conserved. We derive the perpendicular component of $\mathbf{k}$ from energy conservation:

$$\mathbf{k}_z = \sqrt{\frac{2m_e E_{kin}}{h^2} - (\mathbf{k}^{\|})^2}, \tag{5.9}$$

Although their parallel wave vector component $\mathbf{k}^{\|}$ is not changing when the energy of incident electrons is increased, for electrons corresponding to a give reciprocal lattice point, $\mathbf{G}_{hk}$, their perpendicular wave vector component will increase as E_{kin} increases (Figure 5.4). $\mathbf{k}_1$ and $\mathbf{k}_2$ are both due to the same reciprocal lattice point, $\mathbf{G}$. Their incident electron energies are E_1 and E_2. As we increase the incident beam energy (from E_1 to E_2), the patterns on the screen shrink and we are able to observe diffraction patterns corresponding to larger $\mathbf{G}$ vectors.

Superstructures formed by adsorbate or rearrangement of surface atoms have a periodicity greater than normal bulk lattice vectors, $\mathbf{a}_1$ and $\mathbf{a}_2$. Suppose the superlattice vectors are $\mathbf{b}_1$ and $\mathbf{b}_2$. They are related to the normal lattice vectors by

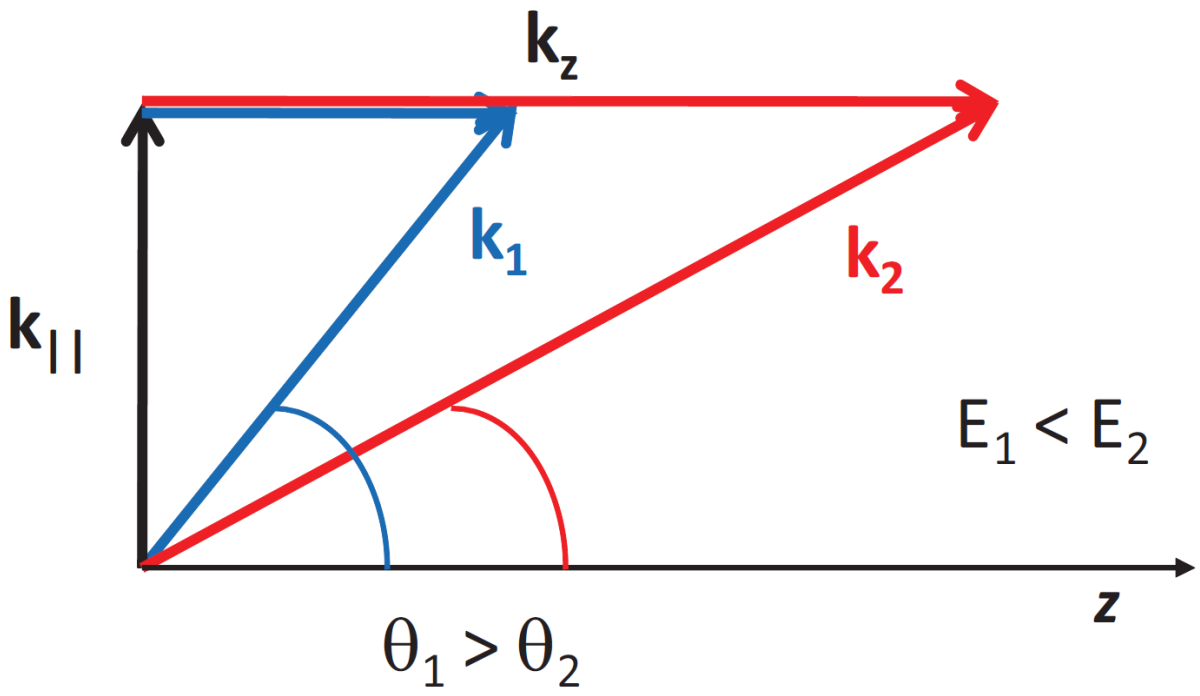

Figure 5.4 Relationship between k_z, $k^{\|}$ and the emission angle for a diffracted electron wave at two different energies. [18]

$$\begin{aligned} \mathbf{b}_1 &= m_{11}\mathbf{a}_1 + m_{12}\mathbf{b}_2 \\ \mathbf{b}_2 &= m_{21}\mathbf{a}_1 + m_{22}\mathbf{b}_2, \end{aligned} \quad , \tag{5.10}$$

where m_{ij} are integers. The reciprocal vectors, $\mathbf{b}_1^*$ and $\mathbf{b}_2^*$ can be derived from $\mathbf{b}_1$ and $\mathbf{b}_2$ in the same way as one obtains $\mathbf{a}_1^*$ and $\mathbf{a}_2^*$ from $\mathbf{a}_1$ and $\mathbf{a}_2$. They will determine the positions of extra bright points on a LEED signal screen. LEED data for a layer of graphene grown on SiC is shown in Figure 5.5.

This LEED image shows clearly the dark points corresponding to the reciprocal lattice and superstructure of the sample. However, the darkness of these black points does not show the intensity of electrons hitting this spot. Therefore, we have neither information on how many electrons are diffracted in a certain direction, nor the ratio of number of electrons diffracted in two different directions. Another defect of LEED is the huge shadow (white) area in the middle of the image and the crack shaped shadow connecting the middle and outside of the image. These shadows are from electron gun and block part of the signal. One way to solve

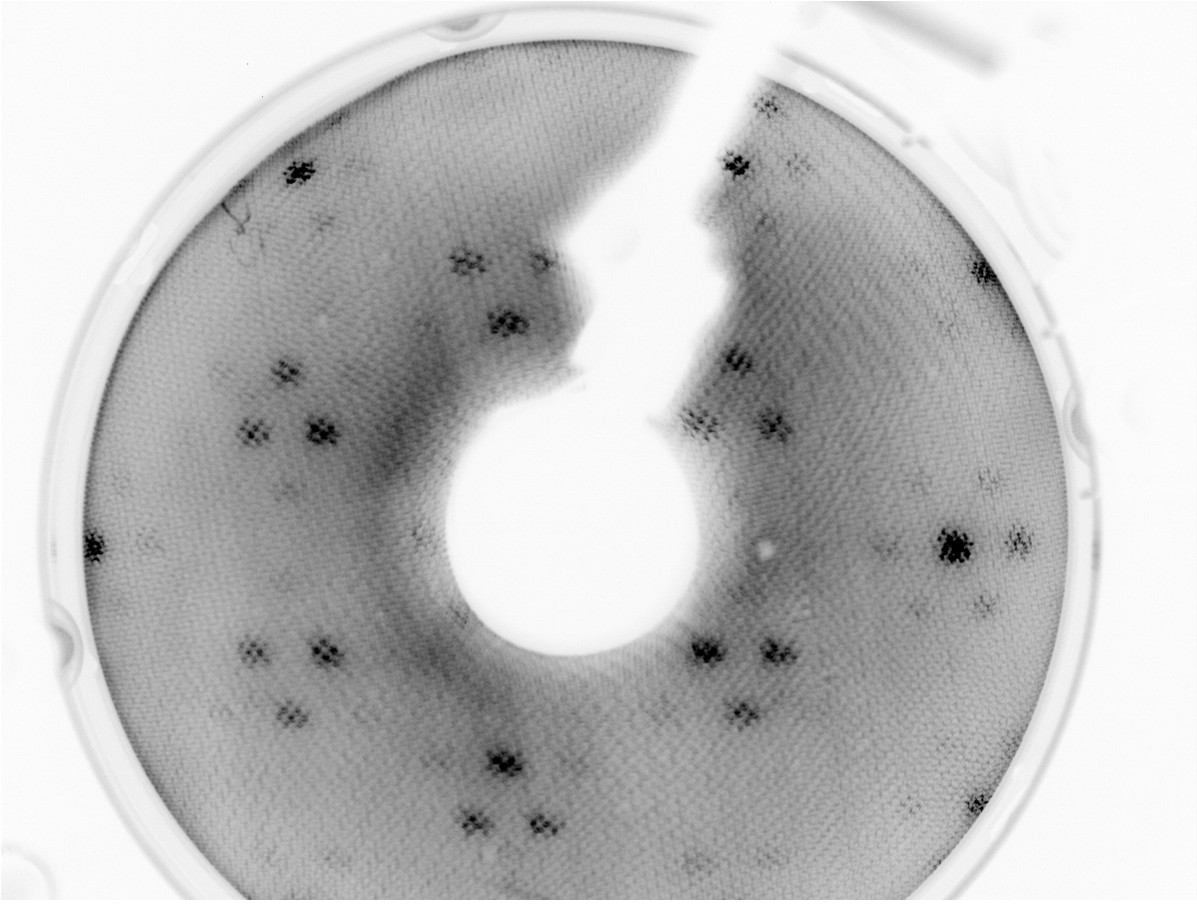

Figure 5.5 LEED image of single-layer graphene on SiC, measured by 95.1 eV electrons.

these problems is to use a spot profile analysis LEED (SPA-LEED). The SPA-LEED device is shown in Figure 5.6. It uses a channeltron detector to count the electrons diffracted to a certain direction. The octopole plates are utilized to tune the directions of the incident and outcoming electrons. By changing the static electric field produced by the octopole plates, we can measure the number of electrons diffracted to different angles. Also, SPA-LEED has a wavevector resolution $\sim$10 times better than that for a conventional LEED and a strongly reduced beam current. The SPA-LEED for the same type of sample is shown in Figure 5.7 c. We can tell very clearly the dark points are sharper and the signal is unblocked.

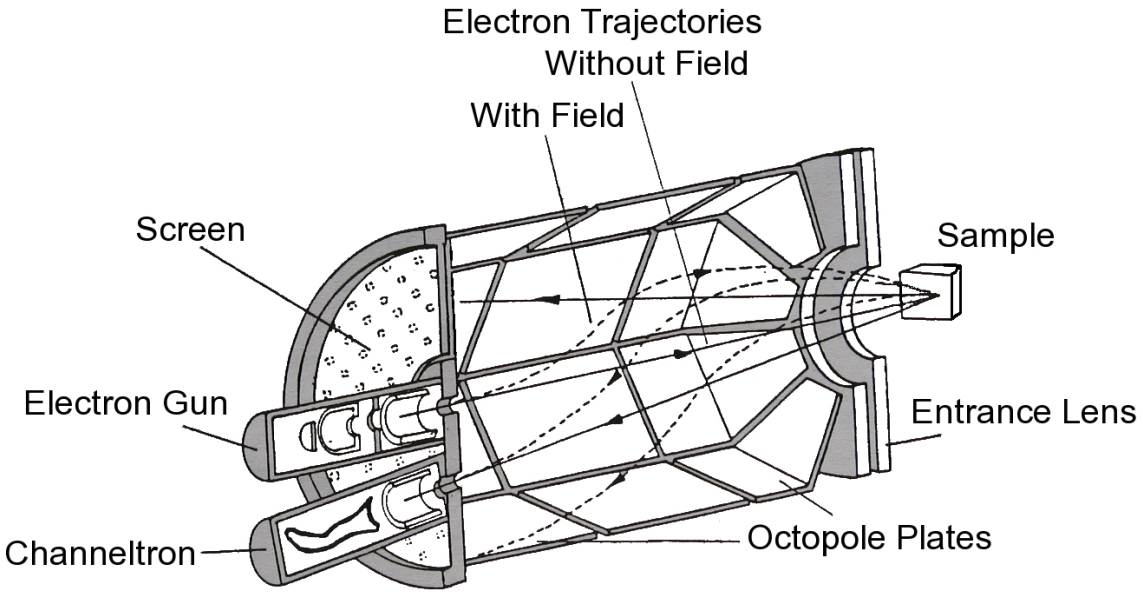

Figure 5.6 SPA-LEED Diagram.

5.2 Methods

We use a commercial 6H-SiC substrate to grow graphene. We first anneal the 2×12 mm substrate at 600 °C for 3 hours to clean its surface by running a current of 0.8 A. Then we increase the current to 1.1 A that heats the SiC to 1200 °C for 10 minutes. This procedure results in a growth of a single layer of graphene, as confirmed by STM, LEED and ARPES. Three-layer graphene is grown by heating up the same sample for another 10 minutes at 1200 °C. ARPES measurements were performed at Ames Laboratory using a high precision ARPES spectrometer that consists of a Scienta SES2002 electron analyzer and GammaData Helium UV lamp equipped with custom designed refocusing optics. All data were acquired using the HeI line with a photon energy of 21.2 eV. The angular resolution was 0.13° and $\sim$ 0.5° along and perpendicular to the direction of the analyzer slits, respectively. The energy corresponding to the chemical potential was determined from the Fermi edge of a polycrystalline Au reference in electrical contact with the sample. The energy resolution was set at $\sim$20meV - confirmed by measuring the energy width between 90% and 10% of the Fermi edge from the same Au reference. The data were measured using several samples yielding consistent results.

5.3 Results And Discussion

Figure 5.7a shows the topology of graphene layer measured by STM. A clear moiré pattern is visible as periodic "checkerboard"-like arrangement of brighter and darker areas. The variation of the intensity is due to combination of periodic changes of height of the layer and electronic densities. A small rhombus is used to outline the 6 × 6 "quasi cell". Figure 5.7b shows the Fourier transform of 5.7a, the bright points in white circles are due to the $6\sqrt{3} \times 6\sqrt{3}$ lattice modulation while other weaker points are due to the 6 × 6 lattice modulation. This data is consistent with the result of SPA-LEED shown in Figure 5.7c. The zero order spot is at the center of the image. It is surrounded by six "6 × 6" spots. The first order diffraction peaks from SiC are surrounding the center peak wirh smaller radius. The graphene first order peaks are further away and rotated by 30° from the SiC pattern. Each of the diffraction peaks is surrounded by six "6 × 6" spots as expected. The ratio of position of graphene and SiC first diffraction spots is about 5:4, the same as their ratio of the reciprocal lattice constant (3.08 : 2.46). In between zeroth and first order diffraction peaks of graphene there are four additional, weaker peaks due to the $6\sqrt{3} \times 6\sqrt{3}$ lattice modulation. A schematic drawing of all observed diffraction peaks is shown in Figure 5.7d based on data in panels (b) and (c). Vector S_1 and S_2 are pointing to SiC reciprocal points, while vector G_1 and G_2 are vectors of graphene layer. All other points arise due to combinations of the S and G vectors. For example, vector v_1 is obtained as $G_1 + G_2 - 2S_1$ and points to one of the six satellite peaks around center. In defining the five vectors v_1, v_2, v_3, v_4, v_5 it is important to define the lattice constants of the two unit cells of the 6 × 6 and $6\sqrt{3} \times \sqrt{3}$ coincidence lattices. If we use the graphene BZ (BZ = $\frac{2\pi}{a_G}$) as 100% then the 6 × 6 reciprocal space unit cell has magnitude $\alpha = 13.3\%$ BZ and the $6\sqrt{3} \times 6\sqrt{3}$ reciprocal space unit cell has magnitude $\beta = 7.7\%$ BZ. Peaks v_1, v_2, v_3 in the diffraction pattern of Figure 5.7d can be written in terms of vectors along the 6 × 6 reciprocal lattice directions which are multiples of α, added to fundamental spots. Point v_1 is separated by a vector of magnitude α from (0, 0), point v_2 is separated by a vector of magnitude 6α from fundamental spot $G_1 - G_2$ and point v_3 is separated by 6α from fundamental spot G_2. On the other hand the points v_4, v_5 belong to the reciprocal lattice of the $6\sqrt{3} \times 6\sqrt{3}$ coincidence lattice at positions 5β

(for v_4) and 8β (for v_5) measured from (0, 0). The origin of the v_4, v_5 points has been debated in the literature over long time (both in the more recent case of graphene and the older literature discussing thermal annealing of SiC to form graphite in terms of being incommensurate spots or as spots originating only from multiple scattering). Our recent high resolution SPA-LEED measurements has identified them to be the strongest spots of the coincidence $6\sqrt{3}$ lattice. These spots are present only when the buffer layer and first layer graphene form, but they fade away as single layer graphene is completed covering the buffer layer. On the other hand the spots corresponding to vectors v_1, v_2, v_3 are still present even when multilayer graphene is grown, although they decrease considerably in intensity beyond trilayer graphene.

The replicas of the main Dirac cones expected in ARPES data described by a set of vectors described above is shown in 5.7e. The three replica cones originate from the three vectors v_1, v_2, v_3 measured from the corner of the BZ K_2. They are related to the corresponding wavevectors of the LEED pattern in fig. 5.7d if the LEED vectors are translated by the vector ΓK_4. The side of the BZ is 57% BZ (or 4.33α). The three vectors are separated by α (the v_1 vector), by 1.666α (v_2) and by 2.666α (v_3) measured from K_2. The vectors v_2 and v_3 are symmetrically located from the midpoint of the side $K_2\Gamma$ and their separation is α. When they are compared to the experimental ratios seen in fig. 5.8 (a) and in table 5.1 (normalized to the length of $K_2\Gamma$, 4.33α) they result in ratios 0.23 for v_1, 0.384 for v_2 and 0.615 for v_3, which are in excellent agreement with the measured values 0.24 for v_1, 0.390 for v_2 and 0.619 for v_3. Furthermore if the vectors v_2 and v_3 are measured from the opposite corner K_5 of K_2 (by adding 4.33α) they correspond to vectors 6α ($4.33\alpha + 1.66\alpha$) and 7α ($4.33\alpha + 2.66\alpha$). All wavevectors for the three replicas seen in the current experiments are the same as the replicas seen in ref. [92] (the first replica closest to the BZ was measured from the original corner K_3 so it corresponds to separation α). In ref. [92] only the buffer layer was grown but the current work shows that they are the relevant vectors, even for much thicker graphene.

The plot of ARPES intensity at E_F for single layer graphene grown on SiC is shown in Figure 5.8a and is based on measurement over one sixth of the Brillouin zone and symmetrization. In addition to "main" Dirac cones at the corners of the BZ, there are several additional spots visible that are due to replicas of the main Dirac cones shifted by set of vectors. Namely,

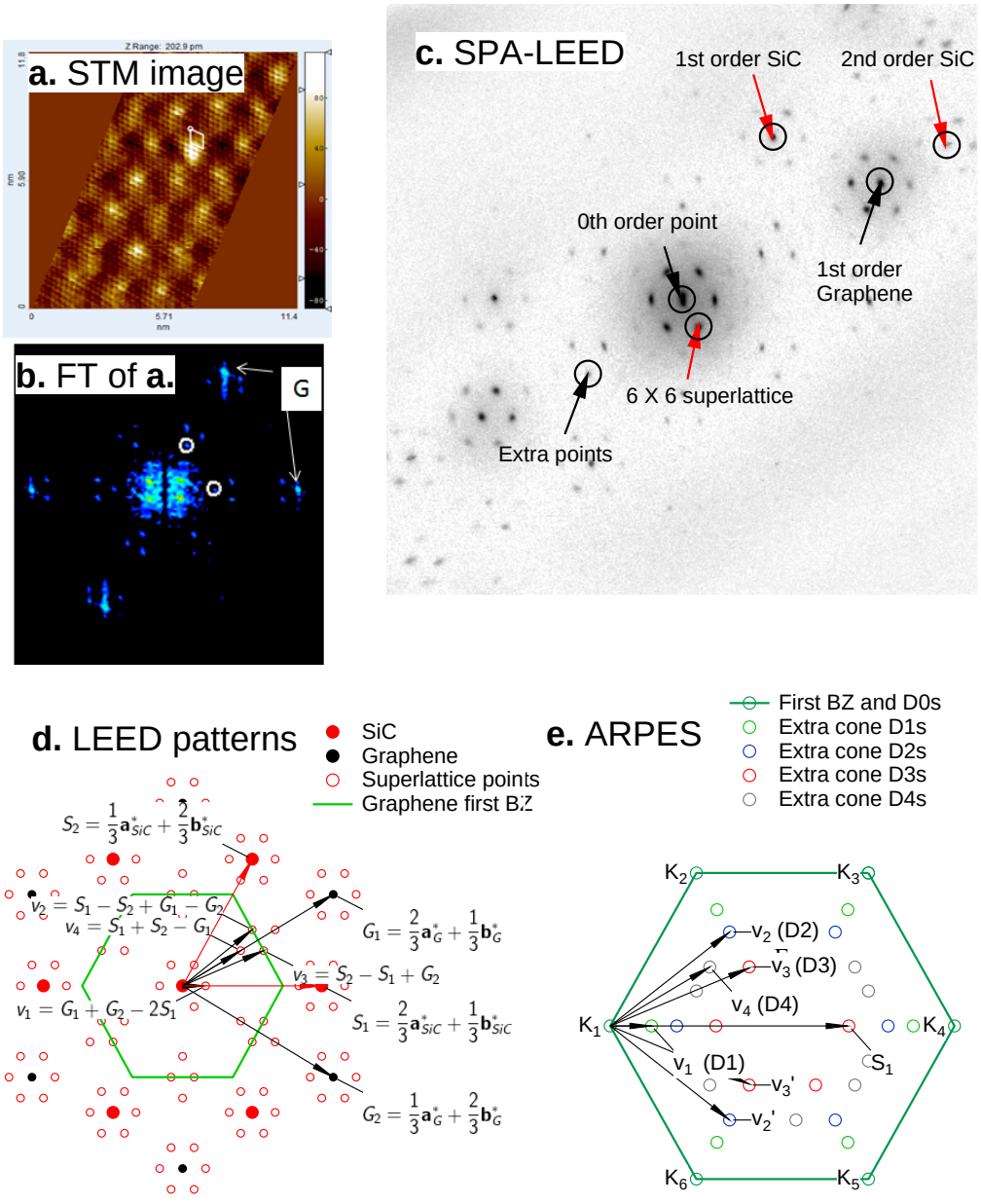

Figure 5.7 a. STM image of graphene grown on 6H-SiC substrate. b. Fourier transform of date from a showing presence of moiré peaks. c. SPA-LEED pattern from single layer graphene sample. d. sketch of diffraction patterns extracted from c. The relevant vectors of SiC, graphene lattice and superlattice are marked by arrows. e. Sketch of expected locations of Dirac cones based on d. a^*_{SiC}, b^*_{SiC} are the reciprocal primitive vectors of SiC and a^*_G, b^*_G are the reciprocal primitive vectors of graphene.

Table 5.1 Calculated positions of the Dirac cones, compare to the measured positions.

	D1	D2	D3
Calculated position (in unit of ΓK)	0.230	0.384	0.615
Measured position	0.240	0.390	0.619
Error (%)	4.8	1.0	0.8

there are three replicas along each symmetry line connecting the center and corners of the BZ and are located at 0.240, 0.390, 0.619 $|a_{\Gamma-K}|$ from K point. The $|a_{\Gamma-K}| = \frac{4\pi}{3\sqrt{3}a_G} = 0.983$ Å^{-1} is the distance between Γ point and K point in the graphene's first Brillouin zone. The location of each of the replicas peaks can be constructed as a combination of the main vector of the graphene and SiC lattices as explained in 5.7e. Therefore, each main Dirac cone D0 is surrounded by three sets of 6 replica Dirac cones. Taking Dirac cone D0 at K_1 as an example, it has one replica at D1s (D1 and its 6-fold symmetry points) (vector v_1), two replica at D2s (vector v_2 and v_2'), and three replica at D3s (vector v_3, v_3' and S_1) within first BZ. Obvious mechanism for observing such objects in ARPES is photoelectron diffraction. The evidence will show that this is not the case here. Instead, what we observe is effect of modulation of the ionic potential "felt" by the electrons in the graphene layer. This is of critical importance, as it must have effect on the transport properties of graphene films grown on solid substrates.

The band dispersion along the Γ - K symmetry direction is shown in Figure 5.8b. Figure 5.8c-f shows the band dispersion along cuts perpendicular to the symmetry axis (marked in panel (a)). The data for the main Dirac cone (panel (c)) was obteined by single scan, while data fro replicas was measured using 30 scans. The main Dirac cone is marked by very sharp contrast from the background and consists of a single band a clear signature of a single-layer graphene [80]. The intensity of the dispersion at each Dirac replica is significantly weaker but still clearly visible on top of the usual ARPES background with D3 being strongest and D2 weakest. The shape of replica dispersion D1 - D3 are identical to D0. The momentum distribution curves (MDC's) at the E_F and -0.8 eV are shown in panels (g) and (h) respectively. The separation of the MDC peaks at E_F is very similar demonstrating close relation between main cone and replicas.

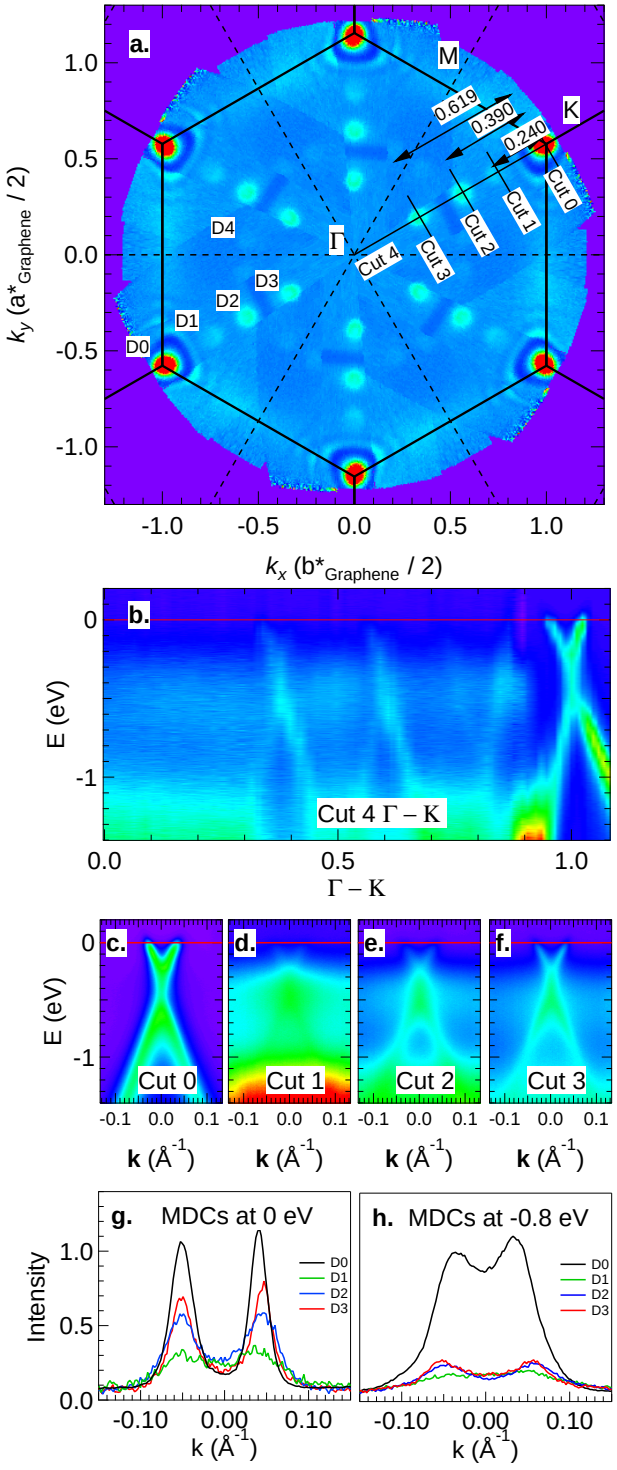

Figure 5.8 a. Fermi surface of single-layer graphene grown on 6H-SiC substrate. b. Energy dispersion along Γ - K direction. c - f. Energy dispersion of Dirac cones D0, D1, D2 and D3 (along directions marked as Cut 0 - 3 in a). g. MDCs at fermi energy (0 eV) in c - f. The height of D0, D1, D2 and D3 peaks are 1.20, 0.25, 0.50 and 0.68, respectively. h. MDCs at 0.8 eV below fermi energy in c - f.

Figure 5.9a shows the Fermi surface of a three-layer graphene grown on SiC substrate. The extra Dirac cones are at the same positions as in single-layer graphene. They can be now seen as circles due to additional sheets of FS originating from three atomic layers of graphene. 5.9b shows constant energy contours at 0.8 eV below Fermi surface for main Dirac cone and three replicas. The main Dirac cone and D1 at this energy have an oval crossection with long axis being horizontal. This is because the vector connecting them is parallel to Γ - K symmetry direction. D2 and D3 cones have also oval shape, but oriented along vertical direction. This is because they are connected with translation vector to adjacent main Dirac cone that perpendicular to the Γ - K direction confirming our model shown in 5.7e. The band dispersion for each cut along perpendicular direction to Γ - K is shown in 5.9c - 5.9f. There are three bands clearly visible below Dirac point consistent with sample being three-layer graphene sheet [80]. The intensity of the Dirac cone replicas are similar to ones in single layer graphene, signifying that they are not due to a photoelectron diffraction. If that would be the case, one would expect the signal to be much weaker, as the corrugation in three layer graphene is much weaker and should not affect photoelectrons emitted from top layer. Definitive evidence for intrinsic origin of the Dirac cones can be directly seen in the relative intensities of the three bands. In each of the dispersion data shown in 5.9c - 5.9f, the pattern of the intensities of each band is different. In D0, the inner and outermost bands are more intense below Dirac point and there is very strong intensity above that point. D1 has very weak intensity above Dirac point and weaker inner band below that point. D2 is similar to D1, but here two inner bands below Dirac points are strongest. D3 on the other hand has strong intensity above Dirac point and below that point the middle band is most visible. If the replicas of the Dirac cone would originate from photoelectron diffraction, the pattern of the intensities would exactly match the one seen in the main Dirac cone. The observed differences demonstrate that the Dirac cone replicas we report are due to small modulation of the ionic potential in the graphene caused by the moiré pattern that forms at the interface of the SiC substrate, carbon rich buffer/wetting layer and graphene.

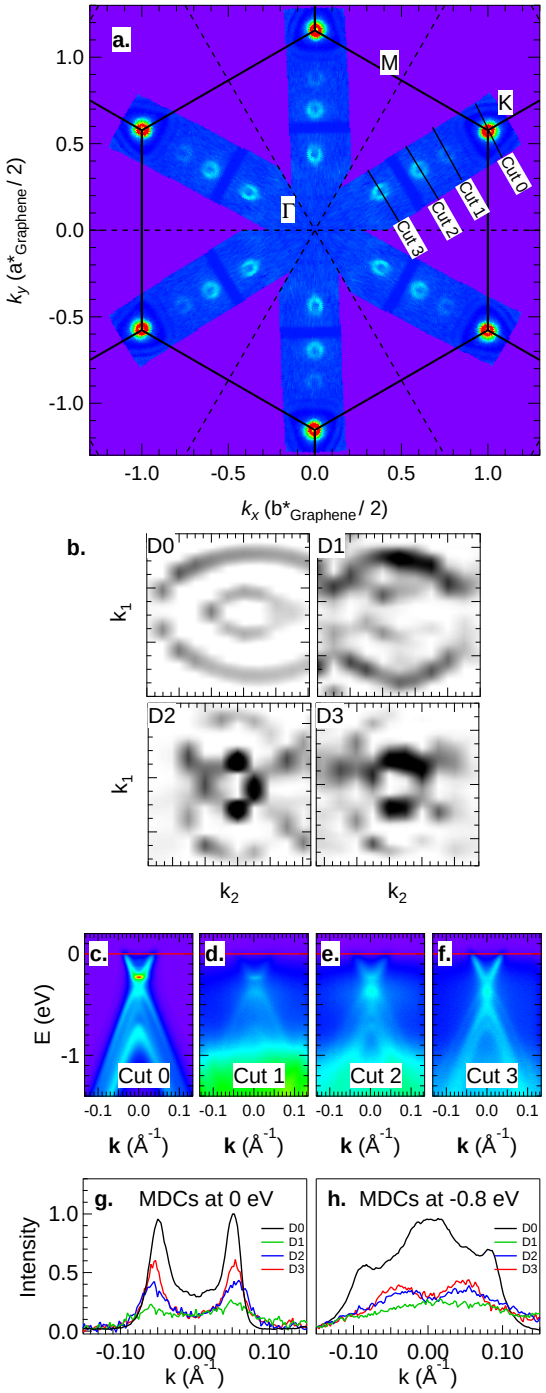

Figure 5.9 a. Fermi surface of three-layer graphene grown on 6H-SiC substrate. b. Constant energy contour after MDC second order differentiate at E = 0.8 eV below Fermi level of Dirac cones D0, D1, D2 and D3. k_1 is perpendicular to Γ - K direction. c - f. Energy dispersion at Dirac cones D0, D1, D2. D3 in the direction perpendicular to Γ - K. The height of D0, D1, D2 and D3 peaks are 1.17, 0.21, 0.40 and 0.60, respectively. g. MDCs at Fermi level in c - f. h. MDCs at 0.8 eV below Fermi level in c - f.

5.4 Conclusions

In summary, we report presence of additional feature in the electronic structure of graphene grown on SiC substrate. Namely there are three sets of replicas of the main Dirac cones at points connected with set of vectors that are linear combinations of the reciprocal vectors of graphene and SiC substrate. We have also demonstrated that these features are intrinsic rather than due to photoelectron diffraction process because they exists in single and tri-layer graphene and the pattern of intensities is very distinct from the ones present in the main Dirac cone. Presence of these features therefore is important to understand several of recent transport measurements.

CHAPTER 6. INTRODUCTION TO WEYL SEMIMETALS

6.1 Weyl Fermions

In 1928, Dirac proposed a linear version of Schrödinger's equation — the Dirac equation [95]:

$$(i\gamma^{\mu}\partial_{\mu} - m)\Psi = 0, \tag{6.1}$$

where γ^{μ} denotes a set of Dirac 4×4 matrices that satisfy following conditions:

$$\{\gamma^{\mu}, \gamma^{\nu}\} = 2g^{\mu\nu} \tag{6.2}$$

$$\gamma_0\gamma_\mu\gamma_0 = \gamma_\mu^{\dagger}. \tag{6.3}$$

This equation is consistent with both the principles of quantum mechanics and special relativity. It successfully describes free electrons and predicts the existence of positrons. Eigenvalues for Eq. 6.1 are $E = \pm\sqrt{\mathbf{p}^2 + m^2}$, where the positive energy solution corresponds to a particle and negative energy solution corresponds to an anti-particle. If the Dirac Hamiltonian was realized in solids, one would think of having an energy band structure, $E_{\pm}(\mathbf{k})$, and the mass term would contribute to an energy gap as shown in Figure 6.1. The eigenfunctions for Eq. 6.1 can be expressed in spinors:

$$u(\mathbf{p}, s) = \sqrt{E+m}\begin{bmatrix} \Phi^{(s)} \\ \frac{\sigma\cdot\mathbf{p}}{E+m}\Phi^{(s)} \end{bmatrix} (particle) \tag{6.4}$$

$$v(\mathbf{p}, s) = \sqrt{E+m}\begin{bmatrix} \frac{\sigma\cdot\mathbf{p}}{E+m}\chi^{(s)} \\ \chi^{(s)} \end{bmatrix} (anti-particle), \tag{6.5}$$

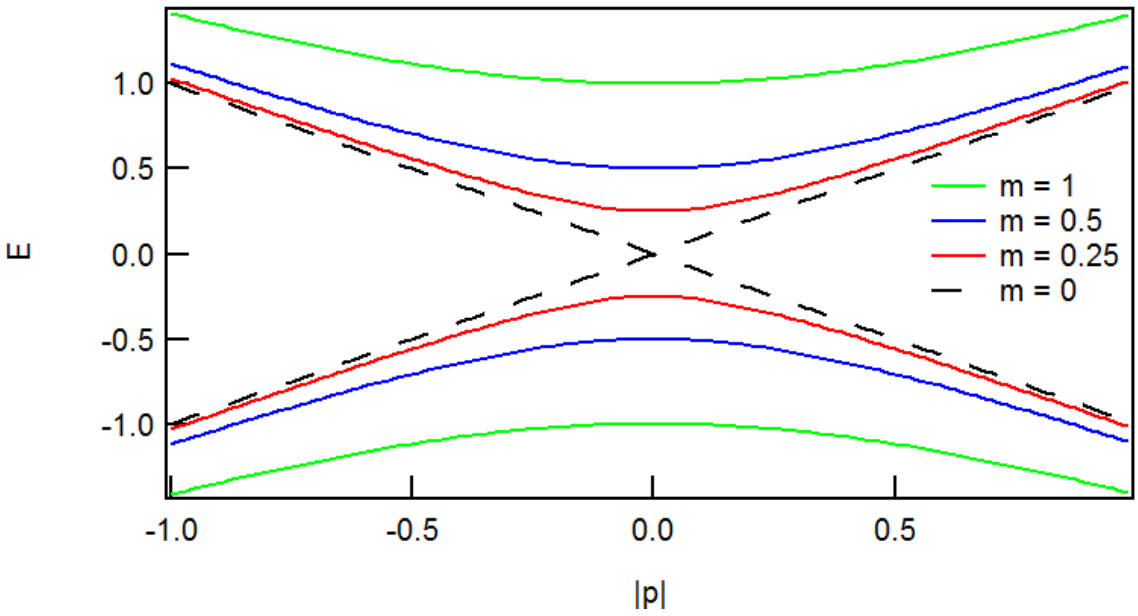

Figure 6.1 Energy dispersion for various solutions of the Dirac's equation. Different colors represent different mass values.

where σ is the Pauli matrices and s = 1 or 2, representing spin up or down. Explicitly,

$$\Phi^{(1)} = \chi^{(2)} = \begin{bmatrix} 1 \\ 0 \end{bmatrix}, \; and \; \Phi^{(2)} = \chi^{(1)} = \begin{bmatrix} 0 \\ 1 \end{bmatrix}. \tag{6.6}$$

Dirac's equation 6.1 and its variations give rise to three types of fermions, Dirac fermion, Majorana fermion, and Weyl fermion. Dirac fermions are subatomic particles that are not their own antiparticle. They satisfy the solution 6.4 of Dirac's equation. The Majorana equation includes the charge conjugate Ψ_c of a spinor Ψ:

$$i\gamma^{\mu}\partial_{\mu}\Psi - m\Psi_c = 0, \tag{6.7}$$

where $\Psi_c = i\Psi^*$. Majorana fermions satisfy solution to the Majorana equation 6.7, and they are their own antiparticles because solutions to Equation 6.7 must be real. In 1929, one year after Dirac's paper was published, Weyl [96] showed that for massless fermions, Dirac equation can be written as Weyl equation

$$i\gamma^{\mu}\partial_{\mu}\Psi = 0. \tag{6.8}$$

Instead of the four components solution to Dirac equation, the solution to Weyl equation 6.8 could be reduced to two components for which the energy eigenvalues are:

$$E = \pm|\mathbf{p}|, \tag{6.9}$$

The Weyl eigenfunctions satisfy following conditions:

$$\begin{aligned} \sigma \cdot \mathbf{p}\phi_L &= -E\phi_L \\ \sigma \cdot \mathbf{p}\phi_R &= E\phi_R \end{aligned}. \tag{6.10}$$

We use labels L and R to denote the helicity of Weyl fermions.

6.2 Handness

A Weyl fermion is called "left-handed" or "right-handed". There are two different definitions of handness for Weyl fermions: helicity and chirality. The helicity of any particle that has momentum and spin is often defined as

$$\chi = \frac{\mathbf{p} \cdot \mathbf{s}}{|\mathbf{p}||\mathbf{s}|}. \tag{6.11}$$

Particles with positive χ, i.e., their momentum and spins have the same direction, are called "right-handed" particles. Those particles with negative χ or their spin is pointing in opposite direction to the momentum are called "left-handed" particles. See Figure 6.2.

From definition 6.11 we see immediately that the helicity is an invariant under rotations. Two observers at two different rotated spatial coordinates will observe the same value of helicity for the same particle. However, helicity is not an invariant under motion. Suppose one observer sees the particle has momentum, $\mathbf{p}$, and spin, $\mathbf{s}$, in the visual frame and another observer moves in the same direction, but with a speed faster than the particle in the same visual frame. The second observer will see the particle move in the opposite direction, and the spin direction is

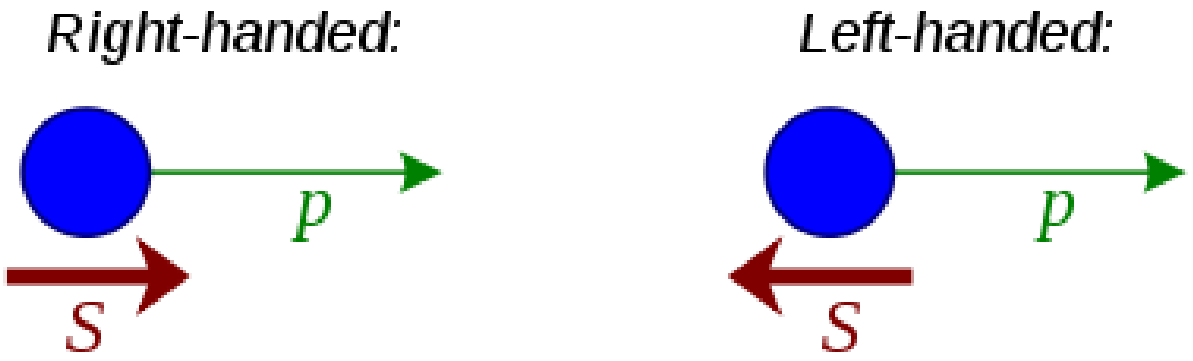

Figure 6.2 Diagram showing the 'handness' of a particle.

unchanged. Therefore, the helicity observed by these two observers will have different signs. The particle appears to have opposite handness for the two observers.

For a massless Weyl fermion moving at the speed of light, its speed is unchanged regardless which visual frame an observer chooses. We write the helicity in Eq. 6.11 as operator:

$$\hat{\chi} = \frac{\mathbf{p} \cdot \sigma}{|\mathbf{p}|}. \tag{6.12}$$

The $\hat{\chi}$ operator commutes with Weyl Hamiltonian H $\propto \mathbf{p} \cdot \sigma$, which means helicity is a conserved quantity. Each Weyl fermion is left-handed or right-handed regardless how it is observed. The eighenvalues for the helicity operator are $\pm$ 1, where +1 means the Weyl fermion's momentum and spin vector is are the same direction (right-handed), while -1 means they are in the opposite directions (left-handed).

Chirality is the other definition of handness. It is related to the matrix, γ_5, defined by other Dirac matrices:

$$\gamma_5 = i\gamma^0\gamma^1\gamma^2\gamma^3, \tag{6.13}$$

which has the following properties:

$$\begin{aligned} \{\gamma_5, \gamma_\mu\} &= 0, \forall \mu \\ \gamma_5^\dagger &= \gamma_5 \\ \gamma_5^2 &= 1 \end{aligned} \quad . \tag{6.14}$$

The left and right chirality operators, L and R, respectively, are

$$\begin{aligned} L &= \tfrac{1}{2}(1 - \gamma_5) \\ R &= \tfrac{1}{2}(1 + \gamma_5) \end{aligned} \quad . \tag{6.15}$$

They can break any Dirac eigenfunction, Ψ, into a left or right chiral component:

$$\Psi = \Psi_L + \Psi_R = L\Psi + R\Psi. \tag{6.16}$$

Equation 6.16 shows that the left- and right-handed chiralities are projection matrices on fermion fields and spinors. Unlike helicity, the chirality is Lorentz invariant, but not conserved for a free particle. Neither of the two definitions is appropriate to describe a massive fermion because for such case, neither is conserved under motion and rotation. However, since γ_5 and $\hat{\chi}$ both commute with Weyl Hamiltonian, a massless Weyl fermion will be either left- or right-handed without any ambiguity. In this case, the helicity and chirality have the same properties.

6.3 Properties of Weyl Semimetals

Although their existence have been predicted since 1929, Weyl fermions have never been observed as an elementary particle. People once thought neutrinos might be Weyl fermions, but later the neutrinos are confirmed to have mass [97]. However, it was determined these elementary particles can emerge as quasiparticles in crystalline solids. For example, graphene has an electron band structure i. e. dispersion relation similar to Dirac fermions [17]. This inspired theorists to look for Weyl fermions in crystalline solids.

Weyl fermions are described by Weyl Hamiltonian

$$H = \mathbf{p} \cdot \sigma. \tag{6.17}$$

If we compare this Hamiltonian with the helicity operator, $\hat{\chi}$, in Eq. 6.11, we find they are proportional:

$$H = E\hat{\chi}. \tag{6.18}$$

A Weyl semimetal is a material whose low energy excitations are Weyl fermions. This enables the realization of Weyl fermion state, which has never been discovered as an elementary particle. The band structure for Weyl fermions would have two linear bands crossing each other, as the dotted lines shown in Figure 6.1. The crossing point is called a Weyl node. The eigen states of $\hat{\chi}$ could also be the solutions to Eq. 6.17. As discussed below demonstrated by Eq. 6.18, the spin vectors in the proximity of a weyl node are either pointing towards the weyl node or in the opposite direction. As a result, in momentum space the Weyl node looks like a hedgehog or a magnetic monopole as shown in Figure 6.3. Similar to the Dirac node in graphene, in the proximity of a Weyl node, the energy bands disperse linearly in momentum space. However, the Weyl nodes always come in pairs, one is left-handed (left chirality) and the other is right-handed (right chirality), like a magnetic source and sink. Another fascinating feature of a Weyl semimetal, shown in Figure 6.3, is presence of Fermi arcs at the surfaces of the sample predicted by theorists [98]. It is a new surface state, connecting the projections of a pair of Weyl nodes on a Fermi surface. The Fermi arcs on opposite planes, i.e., the top and bottom green planes (k_zk_y planes) in Figure 6.3, form a closed loop. If we look at the k_xk_y planes, the two Weyl nodes with opposite chirality will annihilate and no Femi arcs are formed on these planes.

One may think the Weyl node is fragile because normally a small perturbation (doping, crystal defects, etc.) would open a gap, separate the electron and hole bands, and remove the Weyl node. However, small perturbations can not open a gap because the gap in a Weyl semimetal is protected by its topological phase. Next we will discuss some basics for the topological phase and have a better understanding on the protection of gapless modes in Weyl semimetals.

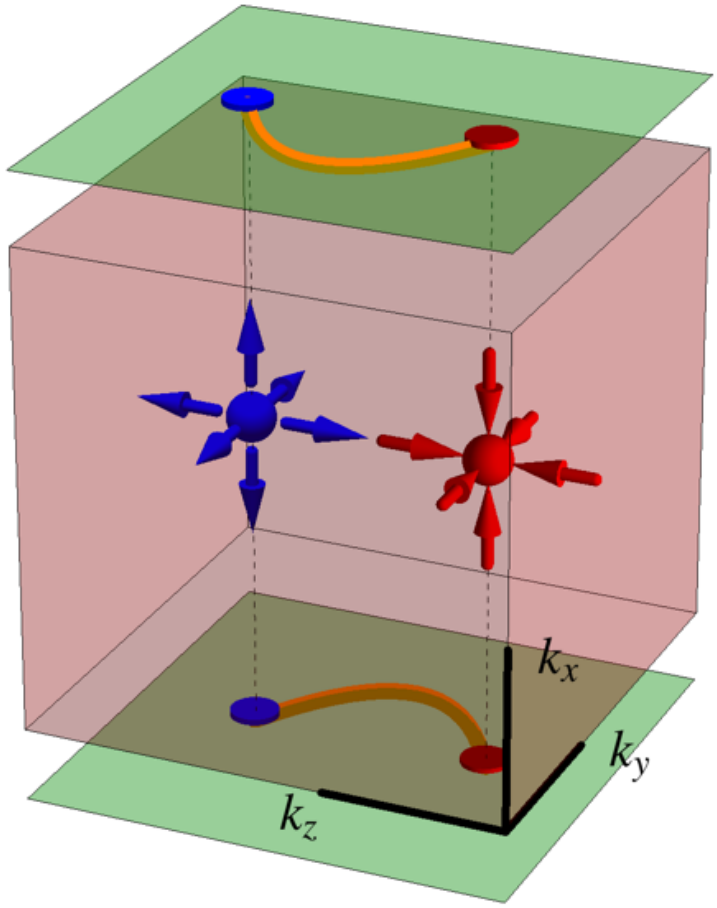

Figure 6.3 Basic features of a Weyl semimetal in momentum space. Two Weyl nodes (red and blue) act as monopoles. The top plane (green) shows the two-dimensional projection, which has a Fermi arc (yellow) that connects the nodes and can be observed in photoemission experiments. [19]

6.4 Topological Phases

Before the discovery of Quantum Hall insulators [23], all phase changes were thought to follow the Landau symmetry-breaking theory, where a phase transition occurs when a system changes from one equilibrium state to another as the expectation value of one parameter changes. This parameter could be temperature, pressure, magnetic field, etc. However, the quantum hall insulators, are characterized by the topological order and do not follow Landau's theory. The general mechanism for topological insulators is band inversion, where the conduc-

tion band and valence band are inverted in a dispersion picture by spin-orbit coupling. We will start with band inversion, then discuss different topological phases, from quantum hall insulators to topological insulators.

6.4.1 Band inversion

According to band theory, for insulators the electrons in the valence band are separated by a large gap from the conduction band as shown in Figure 6.4 b. The valence band is filled with electrons and the conduction band is empty. Therefore, it takes a finite energy, E_G, to excite an electron from the valence band to the conduction band. As a result, an ideal insulator can not have electrons in its conduction band at zero temperature and does not conduct an electric current.

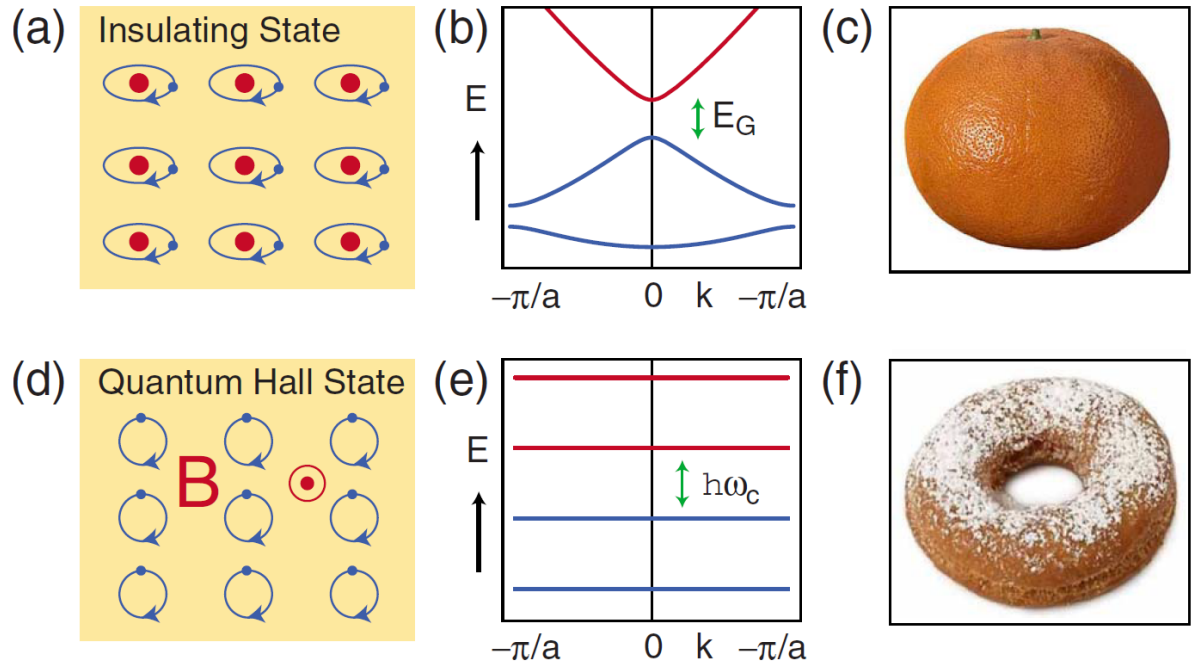

Figure 6.4 Basic states of quantum insulators. (a) - (c) The insulating state. (a) An atomic insulator. (b) A simple model insulating band structure. (d) - (f) The quantum Hall state. (d) The cyclotron motion of electrons. (e) The Landau levels, which may be viewed as a band structure. (c) and (f) Two surfaces which differ in their genus, g. (c) g=0 for the sphere and (f) g=1 for the donut. The Chern number n that distinguishes the two states is a topological invariant similar to the genus. [20]

Conventional insulators and semiconductors have different band gap energy due to their different structures and elemental properties. However, one can always tune the Hamiltonian of these materials continuously, so their bands can transform from one to another without closing of the energy gap. For example, solid argon is an insulator. One can tune its Hamiltonian by increasing its lattice constant. When the lattice constant is increased sufficiently, the solid argon becomes a set of argon atoms. During this process, the filled valence band of solid argon forms the filled $3p^6$ orbitals in argon atoms, while the empty conduction band of solid argon forms the empty 4s orbit in argon atoms. Moreover, the conduction band (4s orbit) and valence band ($3p^6$ orbit) have always different energies. This process defines the topology equivalence between two different insulating states (solid argon and argon atoms, or vacuum). According to the definition, all traditional insulators are topologically equivalent and they are also equivalent to vacuum [20]. We see this in Figure 6.1. The conduction band (positive mass) and valence band (negative mass) are separated by an energy gap because of the mass term in Eq. 6.1.

Not all insulating states are equivalent to a vacuum. These insulating states not equivalent to a vacuum are topological nontrivial phases. These nontrivial phases can be constructed by a band inversion. In a band inversion the relative energies of conduction and valence bands in solid are inverted with respect to a single atom of this solid. For example, "mercury telluride quantum well" is a HgTe layer sandwiched in CdTe layers. There is a critical thickness for the HgTe layer, below which the sandwich is in a normal band state and above it is in a band inverted state (Figure 6.5). In the normal state, conduction band is formed from electron bands in CdTe, which is topologically equivalent to vacuum. If we gradually increase the lattice constant of CdTe to infinity, the conduction and valence bands will transform to the atomic energy levels for Cd and Te. In the whole process, these two bands are always separated, never touching each other. On other hand, because of the strong spin-orbit coupling in HgTe, its conduction band and valence band are inverted. Therefore, if we gradually increase the lattice constant for HgTe to infinity, its conduction and valence bands will transform from an inverted state to a normal state. During this transform, these two bands must touch each other and close the band gap. This results in a quantum phase transition and makes the HgTe be topologically inequivalent to the vacuum.

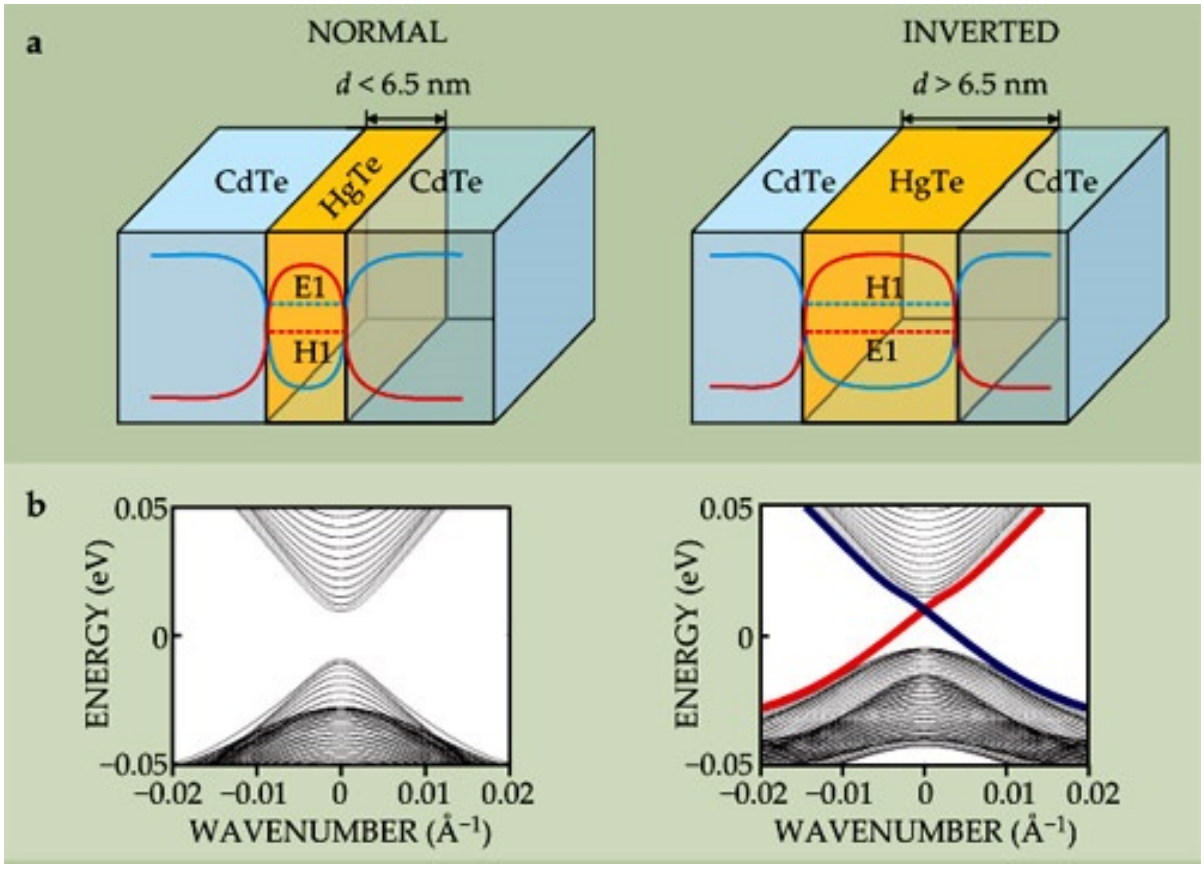

Figure 6.5 HgTe quantum wells are two-dimensional topological insulators. (a) The behavior of a HgTe / CdTe quantum well depends on the thickness d of the HgTe layer. Here, the blue curve shows the potential-energy of the well experienced by electrons in the conduction band; the red curve is the barrier for holes in the valence band. Electrons and holes are trapped laterally by these potentials, but are free in the other two dimensions. For quantum wells thinner than a critical thickness, $d_c \simeq$ 6.5nm, the energy for the lowest energy conduction subband, labeled E1, is higher than for the highest-energy valence band, labeled H1. But, for d $>$ d_c, these electron and hole bands are inverted. (b) The energy spectra for the quantum wells. The thin quantum well has an insulating energy gap, but inside the gap in the thick quantum well, there are edge states present, as shown by red and blue lines. [21]

We need to point out that the band inversion is a necessary, but not sufficient, condition for topological phases. There is a topological number, which defines a topological phase. For example, the Chern invariant is related to the Berry phase in the Brillouin zone.

$$n_m = \frac{1}{2\pi} \int d^2\mathbf{k} \mathcal{F}_m, \tag{6.19}$$

where $\mathcal{F} = \nabla \times \mathcal{A}_m$ is the Berry flux and the Berry phase, $\mathcal{A}_m$, is defined as a function of Bloch wave functions, $|u_m >$:

$$\mathcal{A}_m = i < u_m | \nabla_k | u_m > . \tag{6.20}$$

The Chern number $n = \sum_{m=1}^{N} n_m$ is a sum of Chern invariant for all bands. It is an invariant and does not change when the Hamiltonian changes smoothly, i.e., as we gradually increase the lattice constant for HgTe. Therefore, different Chern numbers define different topological phases of matter. This is in analogy to a genus, g, that classifies 2D surfaces, as shown in Figure 6.4 c and f.

However, calculating the Chern number in general is usually difficult in practice. It is much easier to calculate and measure band inversion for a real sample. In most cases, band inversion is very helpful in terms of identifying new topological states and understanding of the topological nature of various topological materials.

6.4.2 Hall effect

In 1879, Edwin H. Hall discovered the Hall effect (HE) [99]. Namely, generation of voltage (Hall voltage) across an electrical conductor (transverse to an electric current) when an external magnetic field is applied perpendicular to the current, as shown in Figure 6.6. The Hall voltage is given by

$$V_H = -\frac{IB_z}{nde}, \tag{6.21}$$

where I is the current in x-direction, B_z is the magnetic field, n is the charge carrier density, d is the thickness of the plate sample, and e is the charge of an electron.

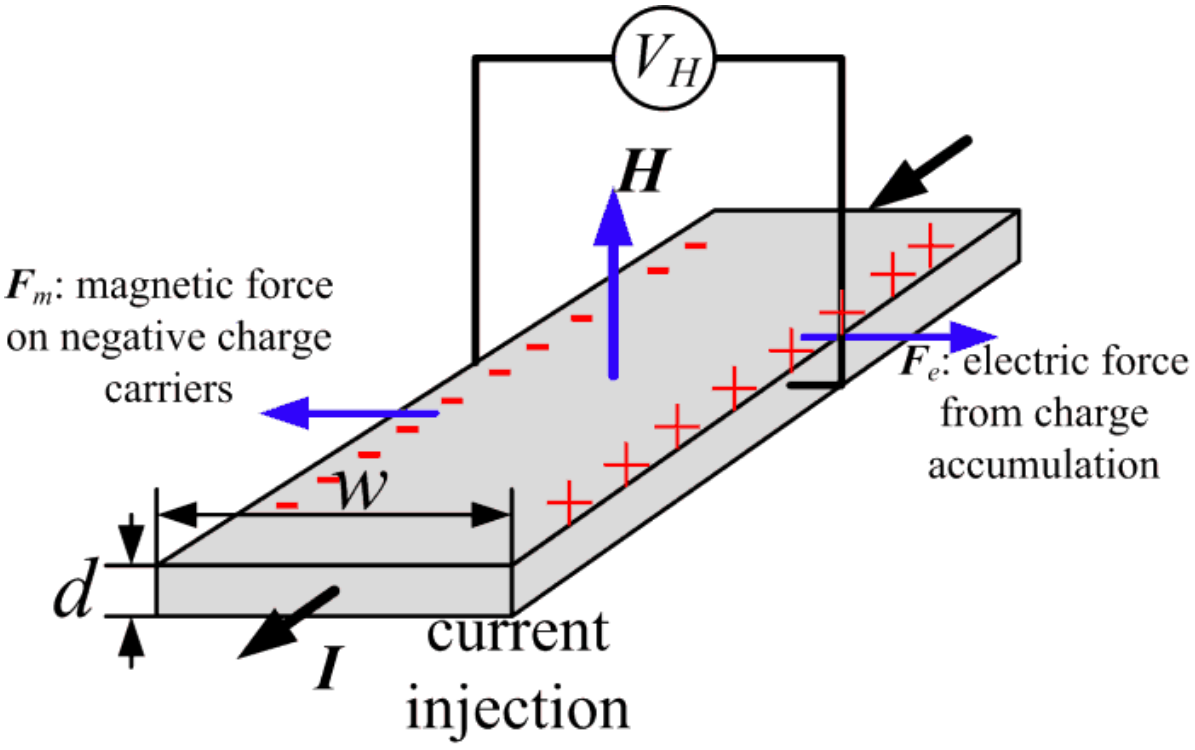

Figure 6.6 Hall effect. A conductor with current applied along its length. An external magnetic field, H, is applied in z-direction and an electric field, ξ_x, is applied in x-direction in the conductor. As electrons move in the -x direction, they will be deflected by the magnetic field because of the Lorentz force. Therefore, a Hall voltage, V_H, is generated across the conductor. [22]

Since the electric field, ξ_y, produced by V_H is perpendicular to the current, Hall resistivity, ρ_{xy}, and conductivity, σ_{xy}, will be a second-order tensor with non-zero off-diagonal elements:

$$\rho_{xy} = \frac{1}{\sigma_{xy}} = \frac{\xi_y}{j_x} = -\frac{B_z}{ne}. \tag{6.22}$$

The HE is a fundamental phenomenon in condensed matter physics and has various applications. For example, it could be used frequently to determine the charge carrier type, density, or external magnetic field.

In 1980, K. v. Klitzing, G. Dorda, and M. Pepper discovered the Quantum Hall Effect (QHE) [23]. They found that a Hall conductivity of a two-dimensional electron gas is an integer times a fixed value e^2/h as shown in Figure 6.7.

$$\sigma_{xy} = Ne^2/h. \tag{6.23}$$

Hall conductivity is insensitive to the geometry of the device, and is related to the topological order and Berry connection. The QHE can be explained semi-classically by quantized Landau levels (Figure 6.4 e) with energy $\epsilon_m = \hbar\omega_c(m + 1/2)$, where $\omega_c = eB/m$ is the cyclotron frequency. In the presence of an external magnetic field, Landau levels can be viewed as a band structure. The energy bands are independent circular orbits. For each Landau level, the number of independent orbits equals the number of flux quanta, $N_B \equiv Be(Area)/h$. The Landau level filling factor is defined as $f = N_e/N_B$. If f is an integer, then an energy gap separates the filled and empty bands like an insulator. However, a QHE device will have its cyclotron orbits to drift under an electric field. Therefore the QHE device is not actually insulating. In 1982, Thouless, Kohmoto, Nightingale and Nijis explained the difference between normal insulator and the QHE device [100]. They calculated the Hall conductivity from the Berry connection using Kubo's formula:

$$\sigma_{xy} = \frac{e^2}{h}n, \tag{6.24}$$

where n is the winding number or Chern number. It is identical to N in Eq. 6.23 and is a topological invariant, so it does not change when the Hamiltonian varies smoothly. For a trivial insulator, the winding number is equal to zero. Therefore, if we define topological insulator as those insulators with a non-zero winding number, the QHE device would be the first discovered topological insulator.

6.4.3 Topological insulators

QHE is a non-trivial topological phase because its time-reversal symmetry is broken by a magnetic field. In the real world, there are more materials that have time-reversal symmetry broken than those that do not. This leads to the question: Is there a non-trivial topological phase with time-reversal symmetry preserved? The answer is 'yes'. It is a new type of topological insulator — quantum spin Hall (QSH) insulator [101]. In a QSH insulator, the bulk is

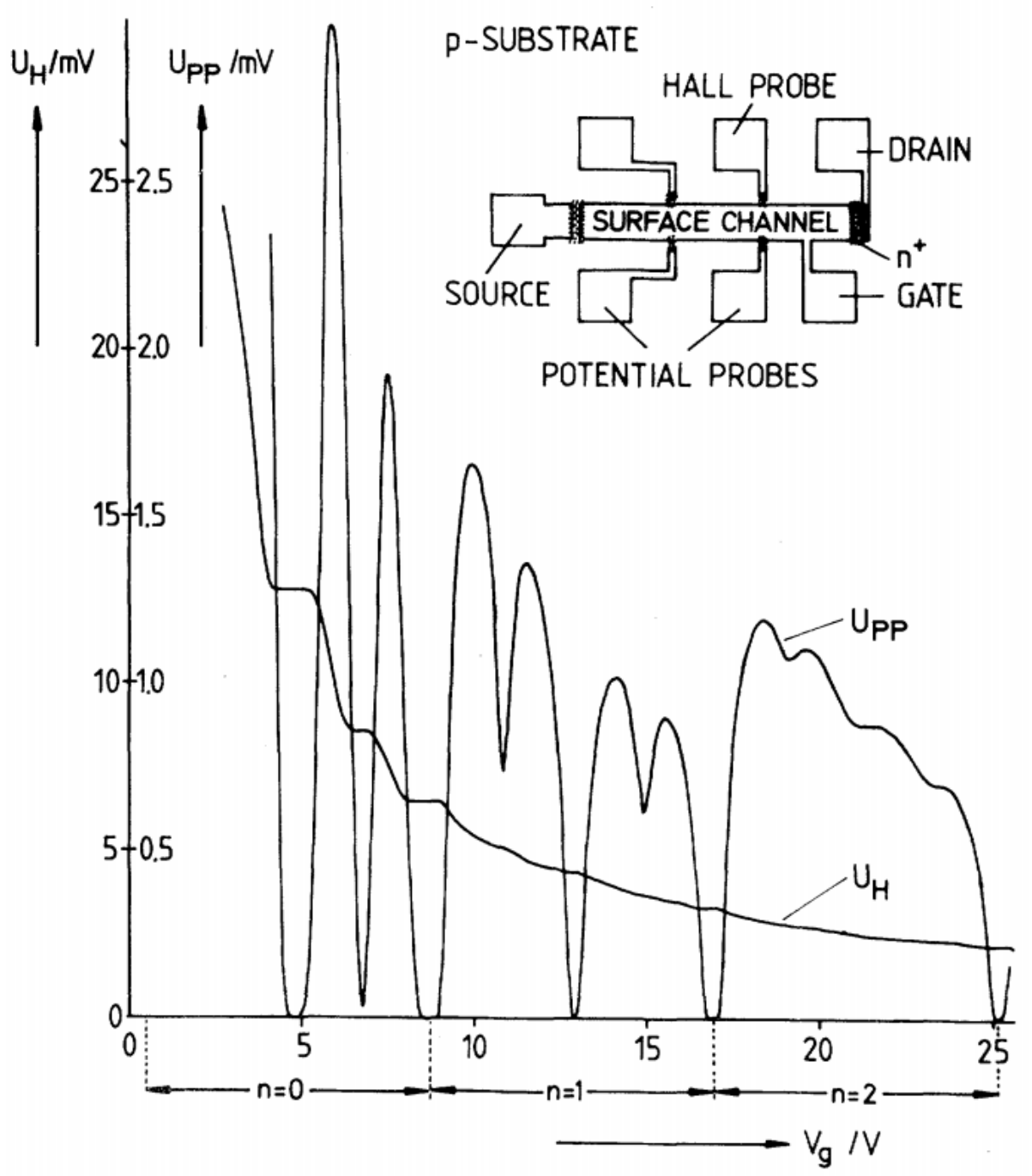

Figure 6.7 Recordings for the Hall voltage, U_H and the voltage drop between the potential probes, U_{pp}, as a function of the gate voltage, V, at T = 1.5 K. The constant magnetic field (B) is 18 T and the source drain current, I, is 1 μA. The inset shows a top view of the device with a length of L = 400 μm, a width of W = 50 μm, and a distance between the potential probes of L_{pp} = 130 μm. [23]

insulating and edges have a pair of edgestates propagating in opposite directions. See Figure 6.8b. We could build a QSH insulator from two QHE insulators. As shown in Figure 6.8a, QHE insulators with edge states propagating to the right has a Chern number n = +1, due to a magnetic field perpendicular to the paper plane. Thus, in the energy dispersion figure, a linear chiral state connects the valence band with the conduction band. Under time-reversal operation $\mathcal{T}$, the eigenstate of the QHE insulator in Figure 6.8a will propagate left and the Chern number becomes -1. Additionally, the magnetic field also must change its sign, pointing in an opposite direction. In the energy dispersion picture, the edge state connecting the valence band with the conduction band will flip about the k = 0 vertical line. Now, if we combine this state with the original state in Figure 6.8a, we obtain a system that preserves time-reversal symmetry. In this new system, the total magnetization will be zero and there will be two edge states propagating in opposite directions in real space. In the band dispersion picture, the two edge states connect the valence and conduction bands as shown in Figure 6.8b (right). Each edge state is associated with one spin state, either spin-up or spin-down. Since the whole system preserves the time-reversal symmetry, its two edge modes must merge at a given k point (i.e., k = 0).

Normally when two bands cross, they will hybridize and open a gap. However, for the two edge state, they have opposite quantum numbers. For example, +k and spin up vs -k and spin down. Those are lined by the $\mathcal{T}$ operator. According to Kramer's theorem, the crossing point must be doubly degenerate because the band crossing is protected by time-reversal symmetry, forming the QSH insulator. QSH insulator is topologically different from a vacuum because it is not possible to remove the two edge modes from the band gap as long as the time-reversal symmetry is preserved. On the other hand, the QSH insulators are also topologically different from the QHE insulators because the reason for band inversion is different. For the QHE insulator, it is the magnetic field, while for the QSH insulator, it is the spin-orbit interaction.

The QSH phase is characterized by a new topological number, called Z_2 invariant (ν). ν can be either 0 or 1, where $\nu = 0$ means topologically trivial and $\nu = 1$ means non-trivial. There are many ways to calculate ν [102, 101, 103, 104]. One method [105] is to write the invariant, ν, as

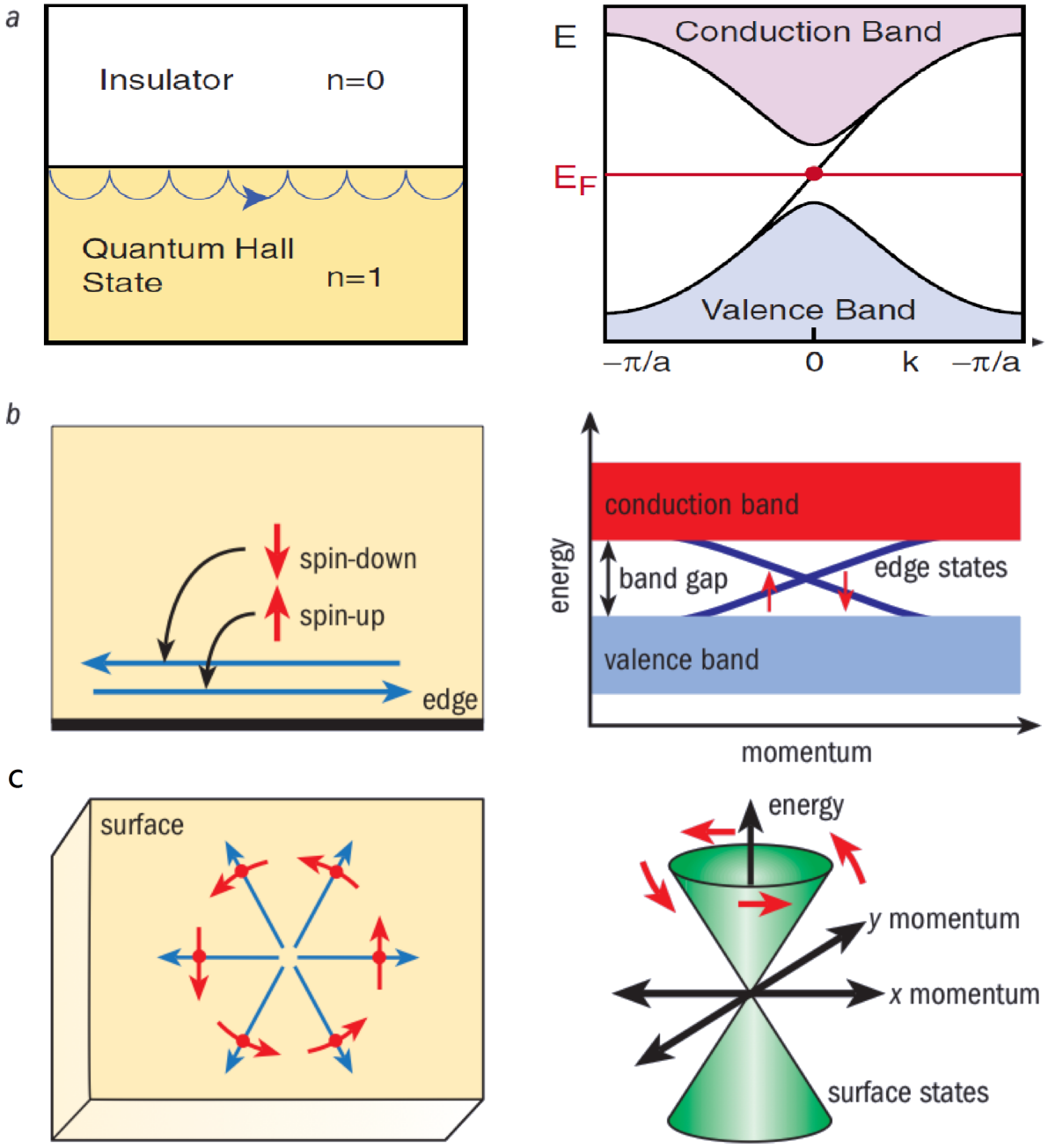

Figure 6.8 (a) (left) The interface between a QHE state and an insulator. (right) The electronic structure of a semi-infinite strip as in left [20]. (b) QSH insulator and its surface and bulk band structure. (c) 3D topological insulator with Dirac cone and helical surface state. [24]

$$(-1)^{\nu} = \prod_{i=1}^{4} \frac{\sqrt{det[w(\Gamma_i)]}}{Pf[w(\Gamma_i)]}, \tag{6.25}$$

where Γ_i are four high symmetric points in the 2D Brillouin zone, $w_{mn}(\mathbf{k}) =< u_m(\mathbf{k})|\mathcal{T}|u_n(-\mathbf{k}) >$ is a unitary matrix defined by the time-reversal operator and Bloch states. The time-reversal operator is antiunitary and $\mathcal{T}^2$ = -1, $w^T(\mathbf{k}) = -w(-\mathbf{k})$. Pf is the Pfaffian of a matrix, Pf(A)^2 = det(A). Therefore, $\delta_i = \frac{\sqrt{det[w(\Gamma_i)]}}{Pf[w(\Gamma_i)]} = \pm 1$. This formula could be generalized to a 3D case and involves eight high symmetry points in the 3D Brillouin zone [103]:

$$\begin{array}{c} (-1)^{\nu_0} = \prod_{i=1}^{8} \delta_i \\ (-1)^{\nu_k} = \prod_{n_k=1;n_{j\neq k}=0,1} \delta_{i=(n_1 n_2 n_3)} \end{array}, \tag{6.26}$$

where $\delta_{i=(n_1 n_2 n_3)} = \pm 1$ is defined for the wavevector $\mathbf{k_i} = \frac{1}{2}(n_1\mathbf{b}_1 + n_2\mathbf{b}_2 + n_3\mathbf{b}_3)$ $(n_i = 1, 2, 3)$ and $\mathbf{b}_k$ are the primitive vectors of the reciprocal lattice. These eight wavevectors satisfy $\mathbf{k_i} = -\mathbf{k}_i(mod\mathbf{G})$. There is a total number of 4 Z_2 invariants in 3D (ν_0, ν_1, ν_2, ν_3).

6.4.4 Weyl semimetal

We know that the QSH insulator ($\nu = 1$) is topologically different from an ordinary insulator ($\nu = 0$). But, how does the topological phase change from one to another? How does the Z_2 invariant change from 0 in a normal insulator to 1 in the QSH insulator? Theorists studied the phase transition between QSH and normal insulators in detail [106, 25]. They found that during the phase transition, the band gap is closed (band inverted) in different ways for systems with and without inversion symmetry. Also, in 3D inversion-asymmetric systems, there is a stable, gapless phase produced in the middle of the transition, while such phase does not exist in the 2D case.

Beginning with the 2D case, the effective Hamiltonian in the vicinity of the phase transition can be written as

$$\mathcal{H} = E_0(m, k_x, k_y) \pm (m - m_0)\sigma_z + (k_x - k_{x0})\sigma_x + (k_y - k_{y0})\sigma_y, \tag{6.27}$$

where m is an external parameter that controls the phase transition. As we gradually increase m from m $< m_0$ to m $> m_0$, the 2D system will change from a normal insulator phase to

the QSH phase. During this phase transition, band inversion occurs at (m, k_x, k_y) = (m_0, k_{x0}, k_{y0}). The band inversion in inversion-symmetric (I-symmetric) and inversion asymmetric (I-asymmetric) systems are different. As shown in Figure 6.9, for the I-asymmetric case, the band inversion occurs at two points, $\mathbf{k} = \mathbf{G}/2 \pm \mathbf{k}_0$. Because of time-reversal symmetry, the band crossing at these two points occurs simultaneously at m = m_0. For the I-symmetric case, the band inversion occurs at $\mathbf{k} = \mathbf{G}/2$, when m = m_0. Note, the band crossing in Figure 6.9 is the bulk band. It is different from the band crossing in Figure 6.8b, which are edge modes.

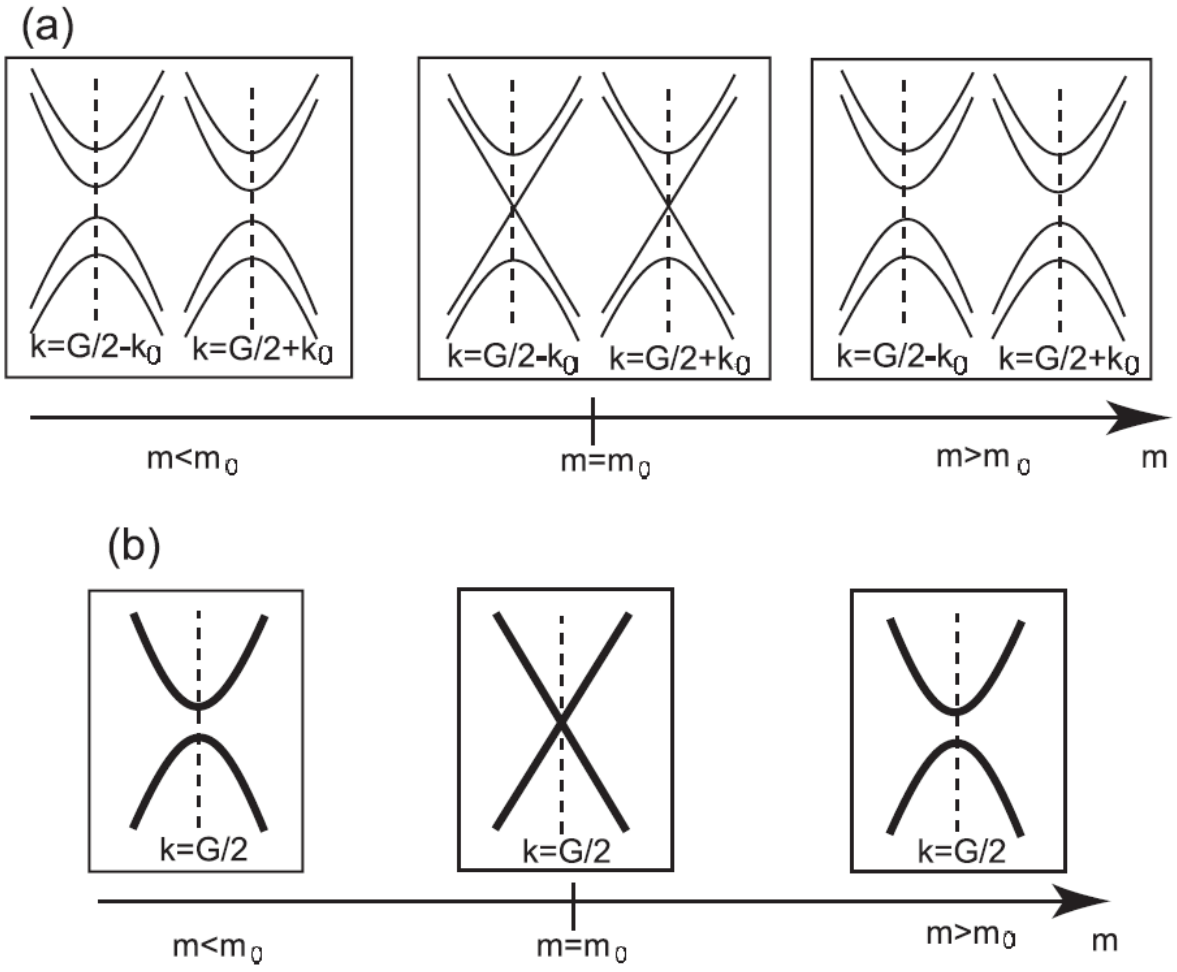

Figure 6.9 Phase transition in 2D between the QSH and insulating phases for (a) I-asymmetric and (b) I-symmetric cases. [25]

The 3D I-symmetric case is similar to its corresponding 2D case. There is a single transition point, m_0, where band crossing and phase transition occur. However, the I-asymmetric case

is quite different. This phase transition does not occur at a single transition point. Instead, there are two key points, m_1 and m_2. In the region $m_1 < m < m_2$, there is a new gapless topological phase. This phase is shown in Figures 6.10 and 6.11. When m $< m_1$, the system is in a normal insulating state and a band gap is present. At m $= m_1$, the conduction and insulating bands begin to touch each other at $\mathbf{k} = \mathbf{G}/2$. This point is doubly degenerate. As m continues to increase, the band crossing point splits into two points in momentum space at $\mathbf{k} = \mathbf{G}/2 \pm k_0$. The pair of points is regarded as monopole and anti-monopole in k space [107, 108]. The positions for the two monopoles in momentum space are a function of the phase transition parameter, m, shown in Figure 6.10a. The red arc consists of the positions of a monopole and the green arc consists of the positions of an anti-monopole. When m increases to m_2, the two monopoles return to the same position and annihilate at this position. By then, the band inversion completes and the 3D I-asymmetric system changes to a QSH state.

We would like to note that the breaking of the inversion symmetry is not the only way to obtain the new topological phase in the middle of the transition between QSH and normal insulator. If we retain the inversion symmetry, but break time-reversal symmetry, the same results would be expected [109]. This new topological phase can be understood as Weyl semimetal [110]. The two monopoles are Weyl nodes with opposite chirality. The energy dispersion is linear near the Weyl nodes. At the Fermi surface, there are two surface states connecting the projection of the two Weyl nodes, as shown in Figure 6.3. Therefore, Weyl semimetal is a new topological phase of matter.

6.5 Experimental Discovery Of Weyl Semimetals

The experimental discovery of topological materials is progressing rapidly in last several years. The HgTe quantum wall structure in Figure 6.5 is the first time the QSH insulator was observed experimentally [111]. In 2008, the first 3D topological insulator was identified in semiconducting alloy of $Bi_{1-x}Sb_x$ [112]. However, its Fermi surface structure is very complicated and the band gap is small. Xia et al. identified another 3D topological insulator with a single Dirac cone only and a large band gap in Bi_2Se_3 [113]. Bi_2Se_3 has protected topological states in ordinary crystal at room temperature and zero magnetic field.

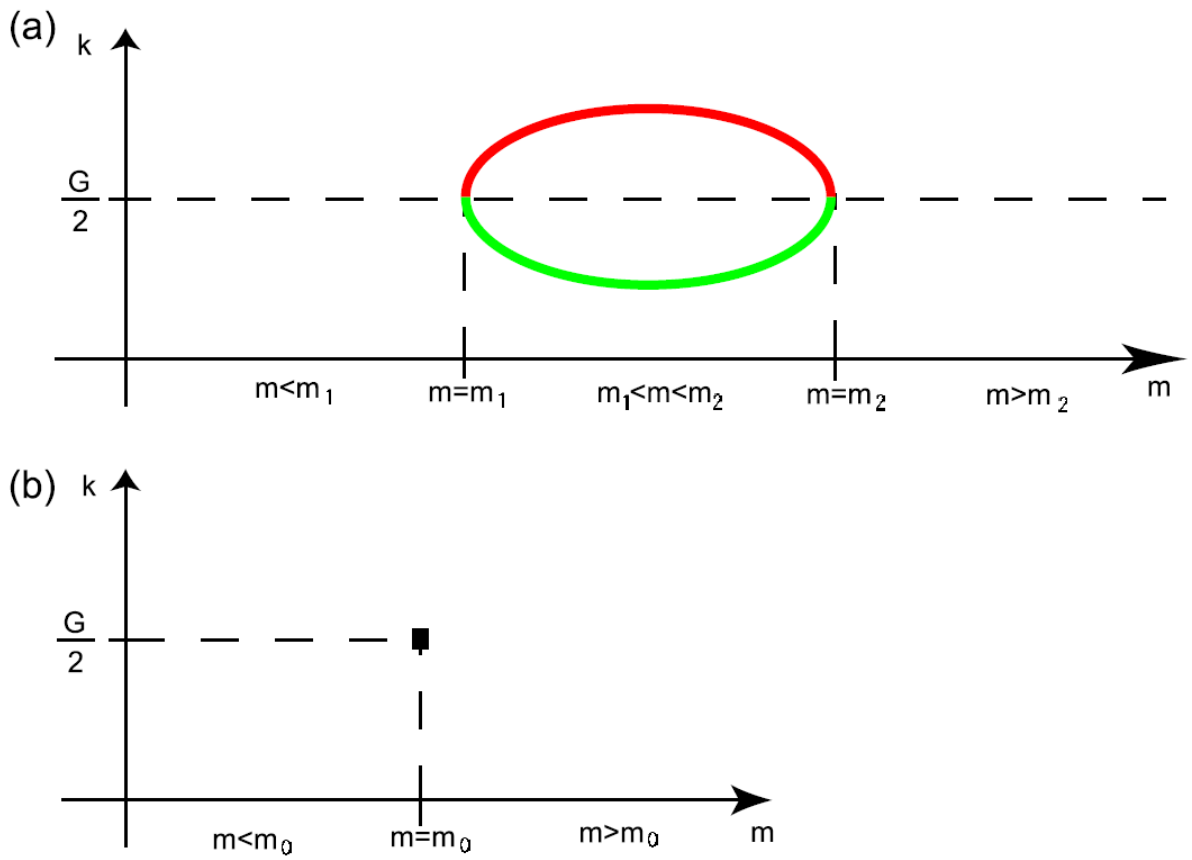

Figure 6.10 Location of the gapless points by changing the external parameter m in (a) I-asymmetric systems and (b) I-symmetric systems. [25]

In 2015, a Weyl semimetal was experimentally identified in TaAs by ARPES measurements [114, 115]. The Weyl semimetallic state is characterized by several pairs of Weyl nodes and Fermi arcs connecting the Weyl nodes on the Fermi surface. Adjacent to the Weyl nodes, the dispersion is linear and forms a Dirac cone structure in energy vs (k_x,k_y) plot, similar to the 2D Dirac cones in graphene [116], the three-dimensional Dirac cones in Na_3Bi and Cd_3As_2 [117, 118] and the two-dimensional Dirac cone surface states for Bi_2Se_3 [113]. However, in Weyl semimetal, time-reversal or inversion symmetry is broken. Therefore, the degeneracy associated with a Weyl node depends only on the translation symmetry of the crystal lattice, which mean the unique properties associated with this electron band structure are more robust [110]. During the same year of 2015, other transition metal monopnictide compounds are discovered to be Weyl semimetal, such as NbAs [119], NbP [26] and TaP [120]. It was also

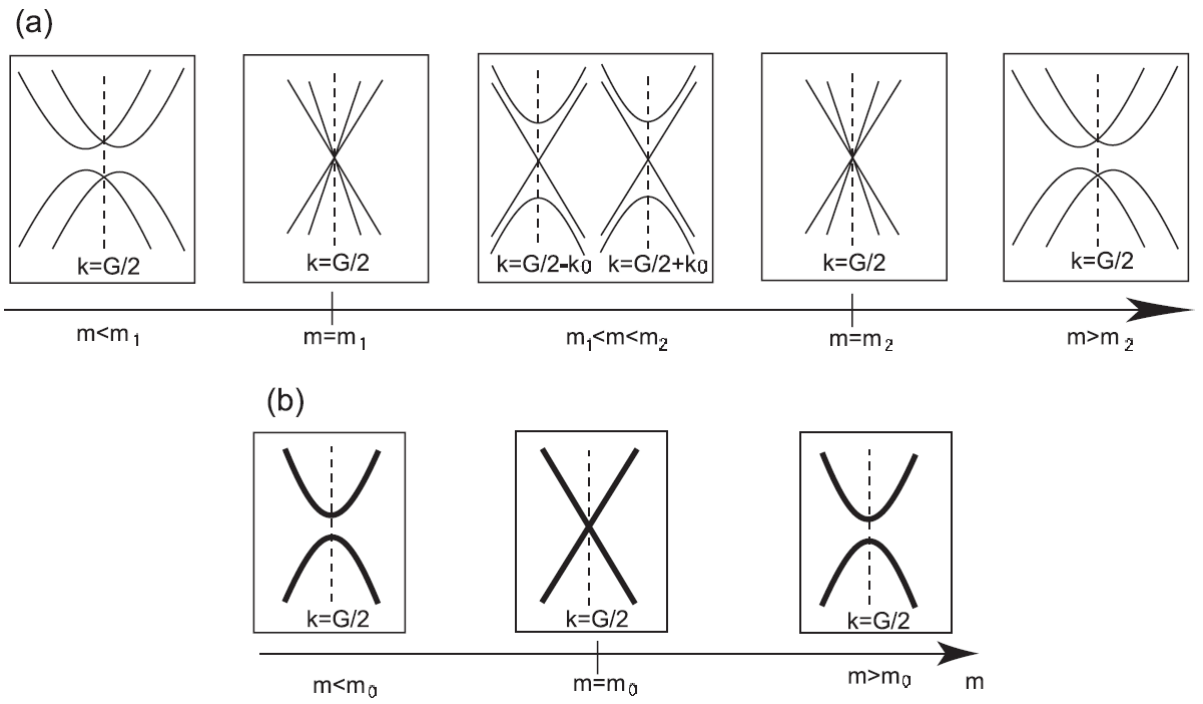

Figure 6.11 Phase transition in 3D between the QSH and insulating phases for (a) I-asymmetric and (b) I-symmetric cases. [25]

found that the separation of a pair of Weyl points is proportional to the spin-orbit coupling (SOC) strength of the material, as shown in Figure 6.12. Because of the unique properties of Weyl semimetals [121, 122, 123, 124, 125, 126, 127, 128, 129, 130] and their possible wide application in new generation of electronics, the studies of Weyl semimetals have attracted a lot of attention.

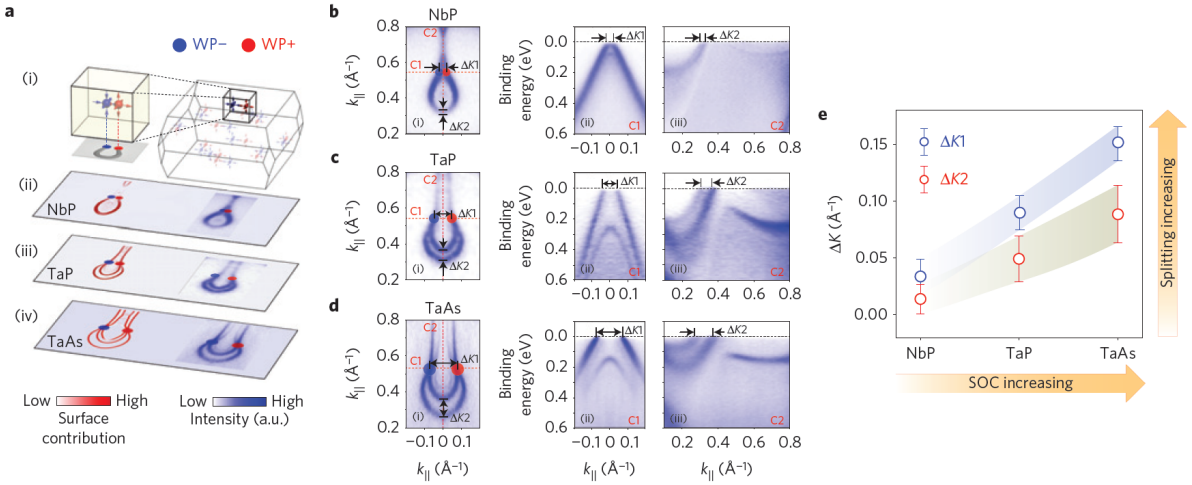

Figure 6.12 Evolution of the band structure with SOC. a, (i) Schematic plot shows a pair of Weyl points projected to the (001) surface BZ and the Fermi arc (grey curves) connecting them. (iiiv) Comparison of the calculated (left) and ARPES measurement (right) of the spoon-like FSs, showing good agreement. Red/blue dots denote theWeyl points of opposite chirality (labelled as WPC and WP). bd, High--resolution ARPES measurements on the spoon-like FS (i) and associated band dispersions (ii,iii) for NbP, TaP and TaAs, respectively. The positions of the band dispersions presented in (ii,iii) are indicated by the red dotted lines in (i). 1K1 and 1K2 represent the separation between theWeyl points and Fermi arcs, respectively. e, Summary of the extracted 1K1 and 1K2 (from bd) from the three compounds, plotted against the SOC strength. Error bars of 1K1 and 1K2 are estimated from the uncertainty in the fitting of the momentum distribution curves at EF. [26]

CHAPTER 7. SPECTROSCOPIC EVIDENCE FOR TYPE II WEYL SEMI-METAL STATE IN MOLYBDENUM DITELLURIDE

A paper submitted to *Natural Materials* [131]

L. Huang, T. McCormick, M. Ochi, Z. Zhao, M. Suzuki, R. Arita, Y. Wu, D. Mou, H. Cao, J. Yan, N. Trivedi, and A. Kaminski

7.1 Introduction

It is quite surprising and yet exhilarating that non-interacting or quadratic Hamiltonians can continue to provide so much richness from graphene, to topological insulators and topological superconductors. This list was recently expanded by discovery of topological Weyl semimetals (TWS), the relatively robust three-dimensional analogs of graphene. With all three Pauli matrices involved in the Hamiltonian, perturbations only shift the position of the node in momentum space but do not open a gap.

While the massless solution to the Dirac equation [96] was first proposed by Hermann Weyl in 1929, there are no known examples of Weyl fermions in particle physics. Quantum materials' analogs have been proposed in various classes of topological Dirac [112, 125, 117] and Weyl semi-metals where a pair of Dirac nodes can be separated into two Weyl points (WPs) by breaking either inversion or time reversal invariance. The topological nature of a TWS is reflected in the Berry fluxes of opposite chirality circulating around the WPs and the presence of a Fermi arc formed between the projections of the two Weyl points on a surface at which the bulk is truncated.

Recently, two types of TWS have been identified: Type I TWS can be understood as the limiting point of a semiconductor with a direct band gap that closes linearly at a set of

isolated points. As a consequence, there is zero density of states if the chemical potential is tuned to the energy of the WPs. Type I TWS have been predicted and observed in the TaAs family (TaAs, NbAs and TaP) [132, 114, 133, 134, 120, 135, 26], and also predicted to occur in pyrochlore iridates [136, 98] and carbon allotropes[137]. Type II TWS, on the other hand, can be understood as the limiting point of an indirect gap semiconductor that evolves into a compensated semi-metal with electron and hole pockets that touch at a set of isolated points with a finite density of states at the chemical potential. The two WPs connected by a Fermi arc need not occur at the same energy. $MoTe_2$, WTe_2 and $SrSi_2$ are predicted to be such a type II TWS [138, 139, 140]. The calculations based on precisely determined lattice parameters points to presence of quadruplet of WPs and presence of line nodes[141]. The line nodes are very interesting topological objects that form closed contours of 1D Fermi surfaces in the momentum space [142, 143] that are yet to be observed experimentally. Strong spin orbit coupling can, in principle, break them in to arcs, presence of which was recently reported in extreme high magnetoresistive $PtSn_4$ [144]. There are some signatures of Type II TWS state in mixed compound $Mo_{0.45}W_{0.55}Te_2$[145]. Here we present the first evidence for such state in the stochiometric, low scattering material $MoTe_2$.

One of the most exciting properties of a TWS is the existence of gapless Fermi arcs on the surface. A Fermi surface, defined as the locus of gapless excitations, is typically a closed contour that separates filled states from empty states at zero temperature. In view of that, a chopped up Fermi surface with the two pieces on opposite surfaces is a novel state of matter. Surface sensitive probes such as ARPES have a decided advantage in investigating the structure of arcs, connectivity of electron and hole pockets and locations of Weyl points, which is the topic of our paper.

The crystal structure of $MoTe_2$ is shown in Figure 7.1. It is a semimetal that crystallizes in a orthorhombic lattice. The Fermi surface of $MoTe_2$ also has two 2-fold symmetry axes, along Γ - X and Γ - Y directions. The lattice constants are a = 6.33 Å, b = 3.469 Å. Due to breaking of the inversion symmetry there are two different possible terminations of the cleaved sample surface, referred to as termination "A" and "B" respectively (See Figure 7.1). The two different terminations also have different surface band structures as seen by laser-based ARPES

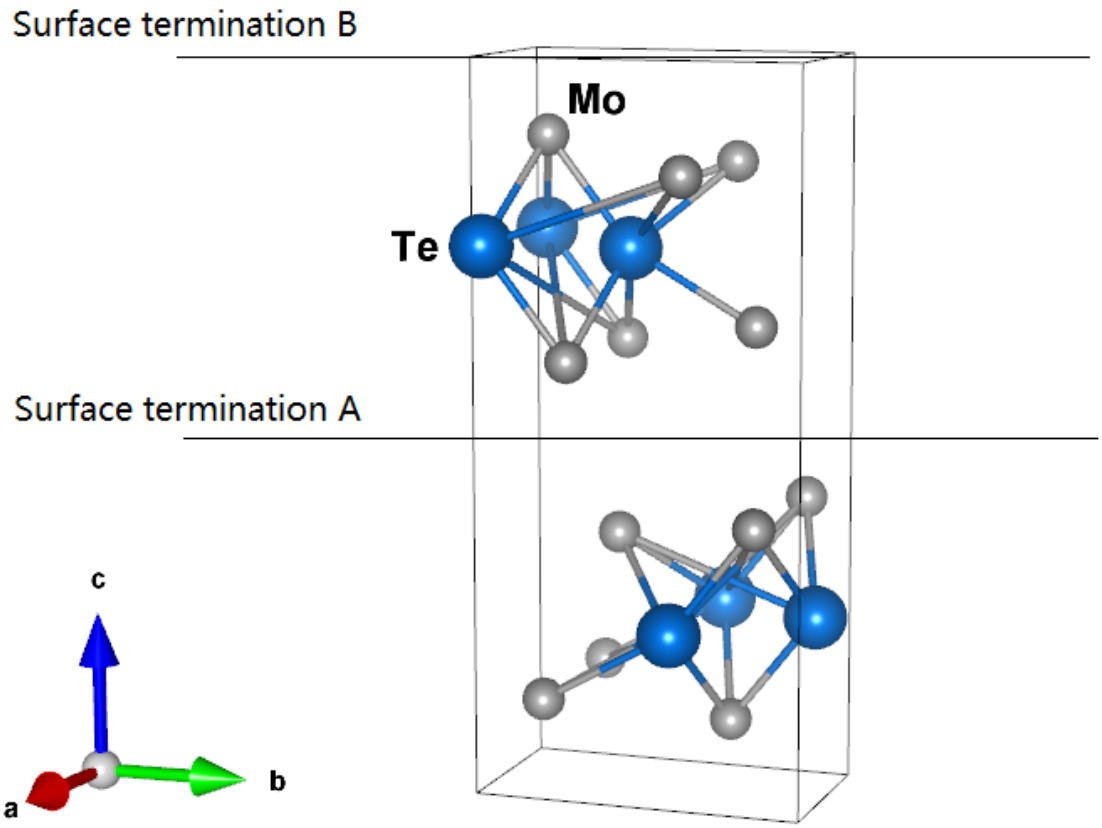

Figure 7.1 $MoTe_2$ crystal structure and two different surface terminations.

and corroborated by density functional theory (DFT) calculations.

7.2 Methods

7.2.1 Sample growth

MoTe2 single crystals were grown out of a Te-rich binary melt using a Canfield crucible set(CCS) [146]. Mo and Te shots in a ratio of 1:9 were loaded into a 5ml CCS and sealed in a quartz tube under vacuum. The quartz ampoule was heated up to 1000C and kept at this temperature for a week. MoTe2 single crystals were isolated from Te flux by centrifuging. Different from most flux growths in which crystals precipitate while cooling from the homogenizing temperature, our growth was performed at a fixed temperature. Single crystals grown

in this strategy have an RRR 500 and MR 40,000% at 2 K in an applied magnetic field of 100 kOe.

7.2.2 Measurements

ARPES measurements were carried out using a laboratory-based system consisting of a Scienta R8000 electron analyzer and a a tunable VUV laser light source [147]. The data were acquired using a tunable VUV laser ARPES system, consisting of a Scienta R8000 electron analyzer, picosecond Ti:Sapphire oscillator and fourth harmonic generator. Angular resolution was set at $\sim 0.05^\circ$ and 0.5° (0.005 Å^{-1} and 0.05 Å^{-1}) along and perpendicular to the direction of the analyzer slit (and thus cut in the momentum space), respectively; and energy resolution was set at 1 meV. The size of the photon beam on the sample was $\sim$30 μm. Samples were cleaved *in situ* at a base pressure lower than 1×10^{-10} Torr. Samples were cooled using a closed cycle He-refrigerator and the sample temperature was measured using a silicon-diode sensor mounted on the sample holder. The energy corresponding to the chemical potential was determined from the Fermi edge of a polycrystalline Au reference in electrical contact with the sample.

7.2.3 DFT calculations

We first performed first-principles band structure calculations for bulk using the Perdew-Burke-Ernzerhof parametrization of the generalized gradient approximation [148] and the full-potential (linearized) augmented plane-wave plus local orbitals (FP-(L)APW+lo) method including the spin-orbit coupling as implemented in the WIEN2K code [149]. We employed the crystal structure determined by our experiment. The muffin-tin radii for Mo and Te atoms, r_{Mo} and r_{Te}, were set to 2.50 and 2.33 a.u., respectively. The maximum modulus for the reciprocal lattice vectors K_{max} was chosen so that $r_{\text{Te}}K_{\text{max}} = 8.00$. Next we constructed a tight-binding model consisting of Mo $4d$ and Te $5p$ orbitals, the parameters in which were extracted from the calculated band structure using the Wannier functions [150, 151, 152] without the maximal localization procedure. Then we made the slab tight-binding model of finite layers, and obtained the band structures and Fermi surfaces. The Mo and Te states on the top or bottom

two layers, i.e. the unit cells of surface A or B, are emphasized in each figure. To identify the position of the Weyl points, we also calculated the Berry curvature for bulk structure using the tight-binding model obtained above. The dominant contribution for the divergence of the Berry curvature ($\Omega^{DD}_{n,yz}, \Omega^{DD}_{n,zx}$) presented in Eq. (30) by X. Wang etc. [153] was calculated and shown in the figure.

7.3 Results And Discussion

7.3.1 Model for type II TWS

To set the stage for interpretation of the experimental results, we investigate a two-band lattice model which breaks inversion symmetry but is invariant under time-reversal symmetry. The main lessons learned by examining this model are shown in Figure 7.2 and summarized here:

(1) The minimum number of four Weyl nodes in this type II TWS occur at E = 0 at the touching point of electron and hole pockets in contrast with a type I TWS that has a zero density of states at E = 0. The touching of electron and hole bands in our model is similar to the touching of the electron and hole bands in the experimental data shown in Figure 7.3a and 7.3b.

(2) For a slab geometry, constant energy cuts at E = 0 show Fermi arcs on surface termination A and B that connect Weyl points of opposite chirality. In addition there are what we term "track states" that exist on the surface and pass through the WPs but, unlike Fermi arcs, form closed loops. For $E < 0$, the projections of the WPs are within the hole pocket, and at the surface the arc states connect the two hole pockets and the track states loop around the electron pockets. The opposite is true for $E > 0$.

(3) The energy dispersion clearly shows a surface state dispersing separately from the bulk bands and merging with the bulk bands close to the WP in Figure 7.2d. This is corroborated by the experimental data around the Weyl nodes in Figures 7.3i and 7.4n where the arc merges with the bulk states.

We consider the following Hamiltonian for a two-band lattice model which breaks inversion symmetry and is invariant under time-reversal:

$$\hat{H}_{Inv} = \sum_{\mathbf{k}} \hat{c}^{\dagger}_{\mathbf{k}\alpha}(\hat{H}(\mathbf{k}))_{\alpha\beta}\hat{c}_{\mathbf{k}\beta}, \tag{7.1}$$

where $\hat{c}^{(\dagger)}_{\mathbf{k}\alpha}$ annihilates (creates) an electron at momentum $\mathbf{k}$ in orbital α and

$$\begin{aligned}\hat{H}(\mathbf{k}) &= \gamma(cos(2k_x) - cos(k_0))(cos(k_z) - cos(k_0))\hat{\sigma}_0 - 2t\ cos(k_z)\hat{\sigma}_3 - 2t\ sin(k_y)\hat{\sigma}_2 \\ &+(m(1 - cos^2(k_z) - cos(k_y)) + 2t_x(cos(k_x) - cos(k_0)))\hat{\sigma}_1.\end{aligned} \tag{7.2}$$

Here $\hat{\sigma}_i$ is the i-th Pauli matrix for $i = 1, 2, 3$ and $\hat{\sigma}_0$ is the 2×2 identity matrix. This model has four Weyl nodes located at $E = 0$ and $\mathbf{k} = (\pm k_0, 0, \pm\pi/2)$ The term in $\hat{H}(\mathbf{k})$ proportional to $\hat{\sigma}_0$ produces a uniform shift in both energy bands. Such a momentum-dependent shift will result in a non-vanishing density of states from electron and hole pockets which touch at the Weyl node and a tilt of the Weyl nodes characteristic of a type II TWS. Henceforth, we set the parameters $m = 2t$, $t_x = t/2$, $k_0 = \pi/2$, and $\gamma = 2.4t$. The bulk band structure for this parameter choice can be seen in Figure 7.2a which shows hole and electron pockets touching at the Weyl nodes as well as pockets disconnected from the nodes. Similar Fermiology is also present in the $MoTe_2$ system and we can gain insight into this and other related materials by taking advantage of the lattice model's simplicity and tunability.

We examine the structure of the surface state configuration by considering the model in Eq. (7.1) in a slab geometry finite in the y-direction with L layers but infinite in the x- and z-directions. We label the states as "surface termination B" ("surface termination A") if they are exponentially localized at $\langle y\rangle = 1$ ($\langle y\rangle = L$). Figure 7.2 also shows the surface states at $\mu = \pm0.1t$ overlaid on the bulk band structure.

We show constant energy cuts through the band structure of the slab geometry in Figures 7.2b and 7.2c for $\mu = \pm0.1t$. When $\mu < 0$, the projections of the Weyl nodes (shown by green dots) are enclosed by hole pockets. Each of these hole pockets are connected to another pocket containing a node of opposite chirality by one Fermi arc on surface A (B) shown as a thick light red (blue) line. When $\mu > 0$, the projections of the Weyl nodes are enclosed by electron pockets

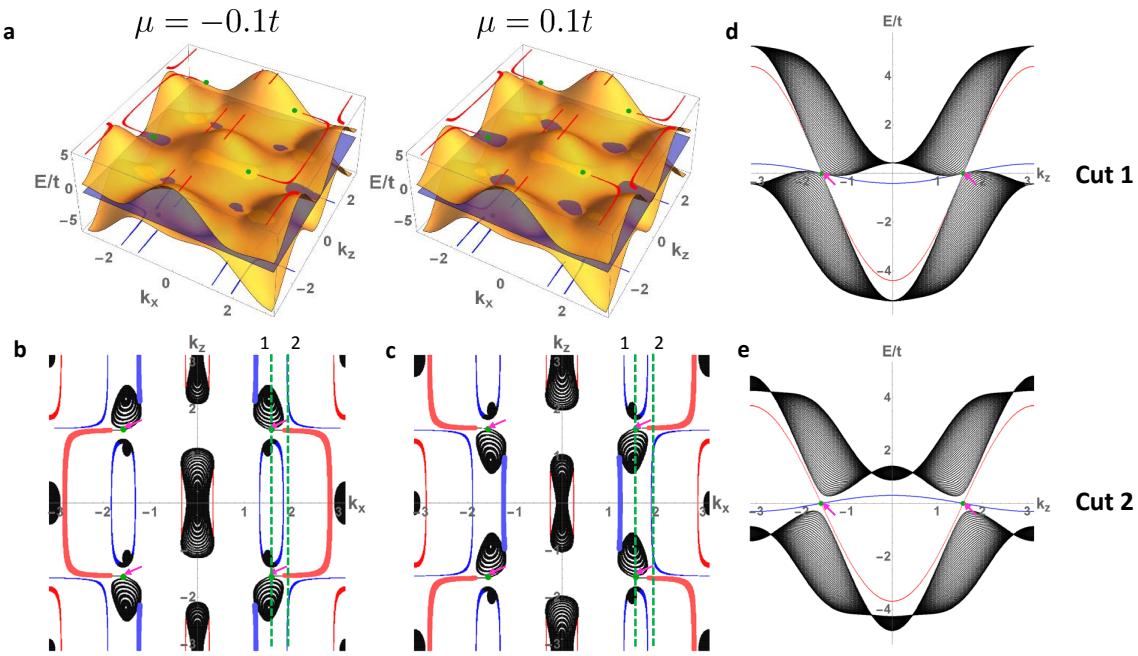

Figure 7.2 Simple model of type II Weyl semimetal described by a two band model given by Eq. 7.2 which exhibits four Weyl nodes. **a** Electronic band structure for $\mu = \pm 0.1t$ indicated by the blue translucent plane. **b,c** The topological surface states and Fermi arcs on surface A (in red) and B (in blue) are calculated for a slab geometry confined along the y-direction. The bulk bands are shown in black. When $\mu = 0$ exactly, the electron and hole pockets touch and the arcs terminate on the node (green dot) itself. For Fermi energy below (above) the nodal energy, arcs of surface states connect the Fermi hole (electron) pockets surrounding a node rather than terminating on a node. **d,e** Energy dispersion along k_z at fixed k_x as shown by cuts in panels (b, c). Cut 1 along $k_x = \pi/2$ shows the bulk electron and hole bands touching at the node and the merging of surface states into the bulk *away* from the Weyl node. Cut 2 along $k_x = 0.63\ \pi$ shows a gap between the bulk bands and a surface state that disperses with opposite velocities at the projections of the two WPs. The WPs are located at $(k_x, k_z) = (\pm\pi/2, \pm\pi/2)$ indicated by pink arrows pointing to green dots.

which are similarly connected by Fermi arcs on the surfaces. At precisely $\mu = 0$, because all of the nodes lie at $E = 0$, all Fermi arcs terminate on the nodes themselves as in a type I TWS.

The slab configuration energy dispersion for fixed k_x is shown in Figures 7.2d and 7.2e. These cuts are shown as green dashed lines labeled cut 1 and cut 2 respectively. We can see that at the Weyl nodes, the red surface bands in Figure 7.2d disappear into the bulk. As we move past the Weyl points in Figure 7.2e, we see that these two red bands combine into a single continuous band.

7.3.2 ARPES Results

We identify electron and hole bands in the spectroscopic data shown in Figures 7.3 and 7.4. The hole bands at the center of the Brillouin zone have a "butterfly" shape. The electron pockets shaped like ovals are located on each side of the butterfly. There are also two banana like hole pockets partially overlapping the oval electron pockets. The configuration of these pockets can be seen at the Fermi energy in Figure 7.3a and 10 meV above the Fermi energy in Figure 7.3b and their electron or hole character is easily identified because hole (electron) pockets shrink (expand) with increasing energy. A simplified sketch of constant energy contours of electron and hole bands is shown in Figure 7.3c.

The central hole pocket touches the electron pockets at four Weyl points shown as red dots in Figure 7.3a-c which we label as W_2. The outer banana shaped hole pockets also touch the oval electron pockets at two other Weyl points labeled as W_3. At surface termination A, Figure 7.3b, those two types of Weyl points are connected by topological arcs seen as white-gray high intensity areas. For this surface termination there is no strong evidence for arcs connecting positive and negative chirality W_2 nor positive and negative chirality W_3 points. The situation for surface termination B is more complicated as shown in Figure 7.3d. There seems to be a sharp contour connecting both sets of W_2 and W_3 points. Most likely this is a track state discussed above. The examination of constant energy plot at energy of 30 meV below E_F (Figure 7.3e), reveals that there are actually two bands present. In addition to the track state, there is also an arc present that connects positive and negative chirality W_2 points. Although present data does not allow us to definitely demonstrate a connection between positive and

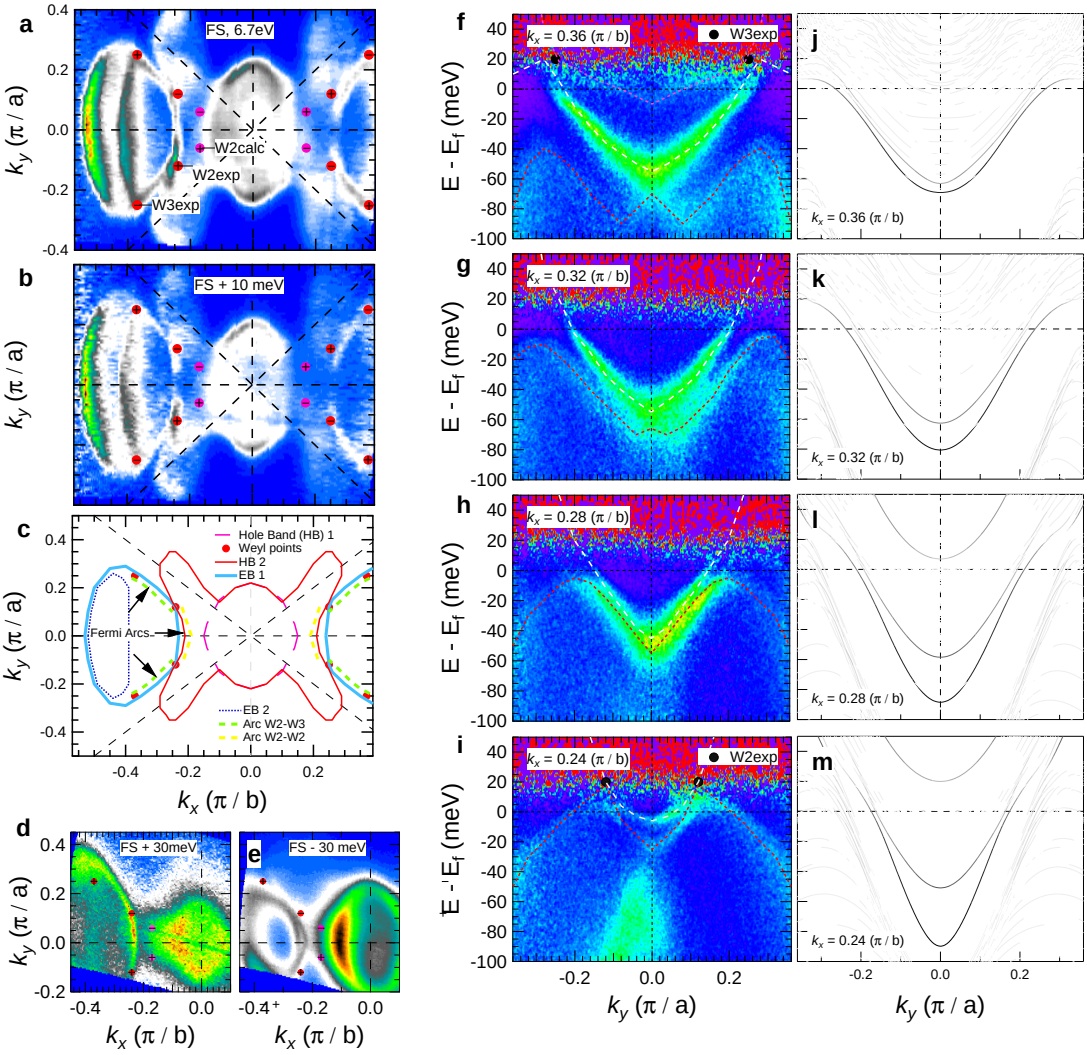

Figure 7.3 Experimental Fermi surface and band structure of $MoTe_2$. **a** Constant energy intensity plot measured at E_F using 6.7 eV photons for a sample with termination A. The calculated (DFT) positions of Weyl points W_2 are marked as pink dots, while experimentally determined locations of W_2 and W_3 points are marked as red dots. The chiralities of Weyl points are marked with "+" and "–" and their locations (k_x, k_y, E) are summarized in Table 7.1. **b** Same as in **a** above but taken at 10 meV above E_F. **c,** A sketch of constant energy contours of electron and hole bands showing the locations of Weyl points and Fermi arcs. **d** Constant energy contour measured at 30 meV above E_F using 5.9 eV photons for a sample with termination B. Positions of calculated and measured Weyl points are marked as above. **e** Same surface termination and photon energy as **d** but at 30 meV below E_F. **f - i** Experimental band dispersion along cuts at k_x = 0.24, 0.28, 0.32 and 0.36 π/b. **j - m** Calculated band dispersion for a sample with termination A along k_x = 0.24, 0.28, 0.32 and 0.36 π/b. Bands plotted with darker lines have more surface weights.

negative chirality W_3 points, we can deduce that they are likely connected, so the arcs on surface A between W_2-W_3 together with arcs on surface B W_2^+-W_2^- and W_3^+-W_3^- form a closed loop when connected via the bulk of the sample.

We now examine the locations of the Weyl points in the band dispersion. In Figure 7.3f-i we plot the band dispersion along k_y cut for selected values of k_x. At k_y=0.36 π/b (panel f) two bands are clearly visible: an "M" shaped band at higher binding energy and a "U" shaped band at slightly lower binding energy. Both bands appear connected at zero momentum with Dirac-like structure. As we move towards the zone center, both bands move to lower binding energy and their energy separation decreases. In panel h, the tips of the "M" shaped band (red dotted line) touches the E_F and form parts of the butterfly hole pockets. As these tips move above E_F, they touch merge with wings of the "U" shaped electron band (white dotted line) forming two Weyl points approximately 20 meV above E_F marked by black dots. At each side of the symmetry line, they form two tilted cones characteristic of a type II Weyl node.

The data along k_x direction are shown in Figure 7.4d-o along with results of calculations (Figure 7.4p-w) for the two surface terminations. The surface termination A is characterized by lower binding energy of electron pocket in panels d-g, when compared to the data from surface termination B shown in panels h-k and l-o. The data in panels l-o best illustrates the formation of the W_2 points. In panel l, the hole band is marked with red dashed line, while the electron band is marked with blue dashed line. As we move away from the symmetry line, the separation between those bands becomes smaller and they merge at a point located ∼20 meV above E_F marked by red dot in panel n. For higher values of k_y momentum they separate again as seen in panel o. The DFT calculation also demonstrates the energy difference of the band locations for the two terminations and formation of the W_2 Weyl point that agrees with experiment on a qualitative level.

The momentum location of the experimentally determined Weyl points is somewhat different from DFT predictions (marked as pink dots in Figures 7.3a and 7.3b) most likely due to high sensitivity of the band calculation to structural parameters. Table 7.1 summarizes the positions of WPs determined from experiment and DFT. Despite the discrepancy between the predicted locations of the Weyl nodes from DFT and where they are located experimentally,

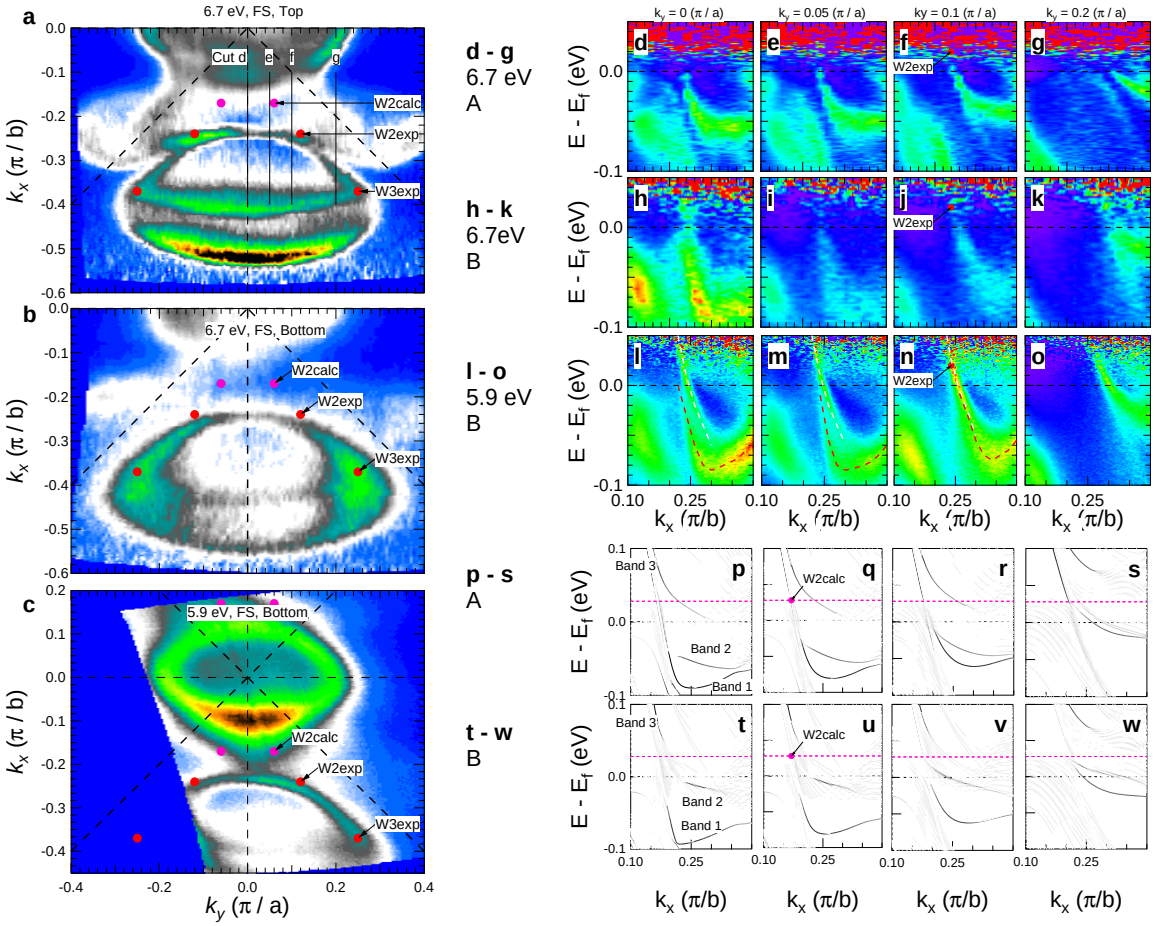

Figure 7.4 Identification of Weyl points and Fermi arcs from experimental data. **a** Constant energy contour at E_F, measured by 6.7 eV photons for surface termination A. DFT predicted locations for Weyl points W_2 and measured Weyl points W_2, W_3 are marked as red and pink dots respectively. **b** The same panel as **a** except for surface termination B. **c** The same panel as **b** except for using 5.9 eV photons. **d - g** Energy dispersion for surface termination A along $k_y = 0$, 0.05, 0.10 and 0.20 π/a. The projections of Weyl points W_2 are marked as dots. **h - k** The same panels as (**d - g**) except for surface termination B. **l - o** The same panels as (**h - k**) except for using 5.9 eV photons. **p - s** Calculated band dispersion for surface termination A along cuts at $k_y = 0$, 0.05, 0.10 and 0.20 π/a. Positions of W_2 are marked similarly as above. **t - w** The same as (**p - s**) except for surface termination B. Bands plotted with darker lines have more surface weights.

Table 7.1 The locations (k_x, k_y, E) of the Weyl points from DFT and ARPES.

	k_x (π/b)	k_y (π/a)	E (meV)
W_2 DFT	± 0.17	± 0.06	28
W_2 Exp	± 0.24	± 0.12	20
W_3 Exp	± 0.37	± 0.25	30

in each case they are at the touching points of the electron and hole bands. In the $k_y = 0$ cuts shown in Figures 7.4d, h, l, p, t, band 1 is connected to bulk states below the Fermi level, while band 3 dips down and goes into bulk just before it reaches the Weyl point. As we increase k_y, band 1 and band 3 merge together. In the $k_y = 0.1$ (π/a) cuts, the two bands merge into one band which goes through the position of the projection of W_2. This behavior is exactly the the behavior predicted in Figure 7.2d and 7.2e.

7.3.3 DFT And Topological Analysis

Figure 7.5 is the DFT calculation of the band structure of $MoTe_2$. 7.5a is the bulk Fermi surface for $k_z = 0.6\pi/c$ and calculated positions of four Weyl points are marked. The shapes of outermost electron and hole bands are very similar to our experiment result in Figure 7.3b. Pink dots are projections of the calculated Weyl points on the $k_z = 0$ plane from energy +28 meV above Fermi level, thus the electron band is not touching the two Weyl point projections. The surface weighted constant energy contours are shown in Figures 7.5d - 7.5g. 7.5d and 7.5e are at Fermi surfaces of termination A and B, while 7.5f and 7.5g are at Fermi level + 28 meV, the DFT predicted energy of W_2. In the calculations, W_2 is not directly connected to another W_2 by surface states on the Fermi surface of termination A calculation while they are connected by weak and short surface states in termination B calculation. However, the W_2 points are connected by bulk electron bands in termination A. This is consistent with our experimental results shown in Figures 7.3a - e. Figure 7.5b is the bulk band dispersion at $W_2 - W_2$ direction, as the vertical dashed line shown in 7.5a. The two W_2 points from DFT are right at the touching points of one hole band and one electron band. Figures 7.5h and 7.5i show termination A and B surface band dispersions along the same direction as in 7.5b. The

surface bands are to connect bulk states near the positions of the Weyl points. Figures 7.5j and 7.5k are termination A and B surface band dispersions along $k_y = 0.05\ \pi/a$ direction, as the horizontal dashed line shown in 7.5a. We also calculated the Berry curvature on Fermi surface. The bright points in Figure 7.5c are possible singular points of the Berry curvature and DFT calculated W_2 points are marked in red and blue, indicating different chiralities of the Weyl points. The summary of energy and momentum locations of Weyl points based on calculations and experiment are provided in Table 7.1.

7.4 Conclusion

We presented the discovery of a type II topological Weyl semimetal (TWS) state in pure $MoTe_2$, where two sets of WPs ($W_2^{\pm}, W_3^{\pm}$) exist at the touching points of electron and hole pockets and are located at different binding energies above E_F. Using ARPES, modeling, DFT and calculations of Berry curvature, we identified the Weyl points and demonstrate that they are connected by different sets of Fermi arcs for each of the two surface terminations. We also find new surface "track states" that form closed loops and are unique to type II Weyl semimetals. This material provides an exciting, new platform to study the properties of Weyl fermions.

This work was supported by Center for Emergent Materials, an NSF MRSEC, under grant DMR-1420451 (theory and data analysis). T. M. M. acknowledges funding from NSF-DMR-1309461 and would like to thank the 2015 Princeton Summer School for Condensed Matter Physics for their hospitality. H.C. received support from the Scientific User Facilities Division, Office of Basic Energy Sciences, US Department of Energy. ARPES data was acquired using Ames Laboratory spectrometer supported by the U.S. Department of Energy, Office of Science, Basic Energy Sciences, Materials Science and Engineering Division. Ames Laboratory is operated for the U.S. Department of Energy by Iowa State University under contract No. DE-AC02-07CH11358.

N. T. and T. M. M. provided theoretical modeling and interpretation. J. Y. and Z. Z. grew the samples. M. O., M. S. and R. A. performed DFT and Berry phase calculations. H. C. performed crystal structure determination. L. H., Y. W. and D. M. performed ARPES

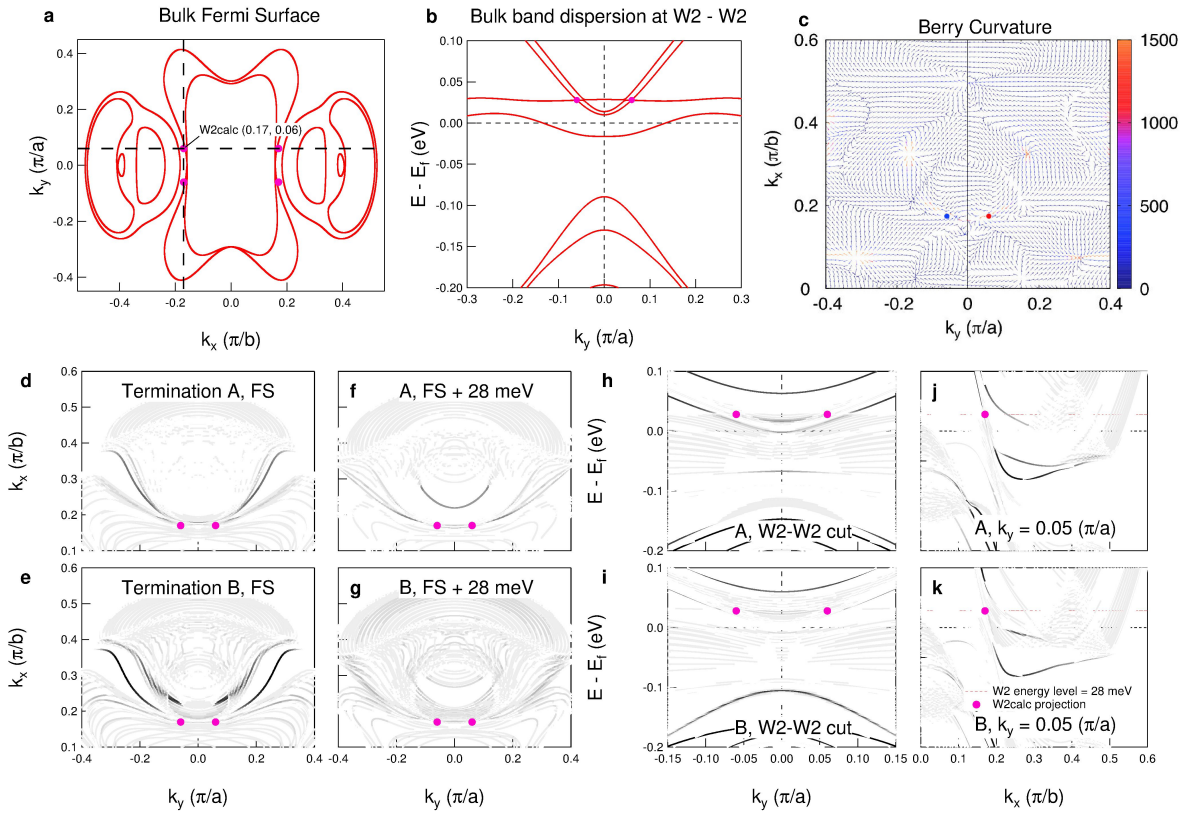

Figure 7.5 Results of DFT calculations. **a** Calculated bulk Fermi surface of $MoTe_2$ for $k_z = 0.6\pi/c$ and projections of W_2 $(k_x, k_y) = (\pm 0.17\ \pi/b, \pm 0.06\pi/a)$ are marked with pink dots. **b** Bulk band dispersion along $W_2 - W_2$ direction (the vertical dashed line in a). DFT predicted positions of W_2 $(k_y, \mathrm{E}) = (\pm 0.06\pi/a, 0.028\ \mathrm{eV})$ are marked. **c** The dominant contribution for the divergence of the Berry curvature $(\Omega^{DD}_{n,yz}, \Omega^{DD}_{n,zx})$ for the $n = N+1$ th band where N is the number of electrons in the unit cell with $k_z = 0$. Red and blue indicate different chiralities of the two Weyl points. **d - g** Calculated constant energy contours of $MoTe_2$. Darker bands are surface bands and lighter bands are bulk bands. **d, e** are at Fermi level for surface termination A and B. **f, g** are at Fermi level + 28 meV of surface termination A and B, respectively. **h, i** Surface band dispersions of termination A and B along W_2-W_2 direction. **j, k** Surface band dispersions of termination A and B along $k_y = 0.05\ \pi/a$ direction, which is very close to the k_y position of W_2 $(0.06\ \pi/a)$. Positions of calculated Weyl points W_2 are marked and darker bands have more surface weights in **d - k**.

measurements and support. L. H. analyzed ARPES data. The manuscript was drafted by L. H., T. M. M., N. T. and A. K. All authors discussed and commented on the manuscript.

BIBLIOGRAPHY

[1] S. D. Kevan. Evidence for a new broadening mechanism in angle-resolved photoemission from cu(111). *Phys. Rev. Lett.*, 50:526–529, Feb 1983.

[2] Andrea Damascelli, Zahid Hussain, and Zhi-Xun Shen. Angle-resolved photoemission studies of the cuprate superconductors. *Rev. Mod. Phys.*, 75:473–541, Apr 2003.

[3] Stephan Hfner. *Photoelectron Spectroscopy*. Springer-Verlag Berlin Heidelberg, 2003.

[4] M. P. Seah and W. A. Dench. Quantitative electron spectroscopy of surfaces: A standard data base for electron inelastic mean free paths in solids. *Surface and Interface Analysis*, 1(1):2–11, 1979.

[5] F. Mangolini, J. hlund, G. E. Wabiszewski, V. P. Adiga, P. Egberts, F. Streller, K. Backlund, P. G. Karlsson, B. Wannberg, and R. W. Carpick. Angle-resolved environmental x-ray photoelectron spectroscopy: A new laboratory setup for photoemission studies at pressures up to 0.4 torr. *Review of Scientific Instruments*, 83(9), 2012.

[6] C. Liu. Electronic structure of iron arsenic high temperature superconductors studied by angle resolved photoemission spectroscopy (arpes). *ISU Thesis*, 2011.

[7] R. Stern, M. Mali, I. Mangelschots, J. Roos, D. Brinkmann, J.-Y. Genoud, T. Graf, and J. Muller. Charge-carrier density and interplane coupling in $y_2ba_4cu_7o_{15}$: A cu nmr-nqr study. *Phys. Rev. B*, 50:426–437, Jul 1994.

[8] T. Kondo, R. Khasanov, J. Karpinski, S. M. Kazakov, N. D. Zhigadlo, T. Ohta, H. M. Fretwell, A. D. Palczewski, J. D. Koll, J. Mesot, E. Rotenberg, H. Keller, and A. Kaminski. Dual character of the electronic structure of $yba_2cu_4o_8$: The conduction bands of CuO_2 planes and cuo chains. *Phys. Rev. Lett.*, 98:157002, Apr 2007.

[9] S. Bollanti, P. Di Lazzaro, F. Flora, L. Mezi, D. Murra, and A. Torre. New technique for aberration diagnostics and alignment of an extreme ultraviolet schwarzschild objective. *Nuclear Instruments and Methods in Physics Research Section A: Accelerators, Spectrometers, Detectors and Associated Equipment*, 720:168 – 172, 2013. Selected papers from the 2nd International Conference Frontiers in Diagnostic Technologies (ICFDT2).

[10] Wikipedia. Pulse tube refrigerator — Wikipedia, the free encyclopedia, 2016.

[11] L.W. Yang and G. Thummes. High frequency two-stage pulse tube cryocooler with base temperature below 20 k. *Cryogenics*, 45(2):155 – 159, 2005.

[12] J. F. Herbst. $r_2fe_{14}b$ materials: Intrinsic properties and technological aspects. *Rev. Mod. Phys.*, 63:819–898, Oct 1991.

[13] A. Kreyssig, R. Prozorov, C. D. Dewhurst, P. C. Canfield, R. W. McCallum, and A. I. Goldman. Probing fractal magnetic domains on multiple length scales in $nd_2fe_{14}b$. *Phys. Rev. Lett.*, 102:047204, Jan 2009.

[14] T. Koyama, D. Chiba, K. Ueda, K. Kondou, H. Tanigawa, S. Fukami, T. Suzuki, N. Ohshima, N. Ishiwata, Y. Nakatani, K. Kobayashi, and T. Ono. Observation of the intrinsic pinning of a magnetic domain wall in a ferromagnetic nanowire. *Nat Mater*, 10(3):194–197, March 2011.

[15] Nanotechnology Encyclopedia. Atomic force microscope, 2016.

[16] Nanoscience Education. Atomic force microscopy, 2011.

[17] A. H. Castro Neto, F. Guinea, N. M. R. Peres, K. S. Novoselov, and A. K. Geim. The electronic properties of graphene. *Rev. Mod. Phys.*, 81:109–162, Jan 2009.

[18] Georg Held. Low-energy electron diffraction crystallography of surfaces and interfaces. *Bunsen-Magazin 12*, 12(12):124–131, April 2010.

[19] W. Witczak-Krempa, G. Chen, Y. B. Kim, and L. Balents. Correlated quantum phenomena in the strong spin-orbit regime. *ArXiv e-prints*, May 2013.

[20] M. Z. Hasan and C. L. Kane. *Colloquium* : Topological insulators. *Rev. Mod. Phys.*, 82:3045–3067, Nov 2010.

[21] S. Zhang. Topological insulators. *Scholarpedia*, 10(7):30275, 2015. revision 151969.

[22] Jian Sun and Jrgen Kosel. Finite-element modelling and analysis of hall effect and extraordinary magnetoresistance effect. In *Finite Element Analysis - New Trends and Developments*, pages –. InTech, 2012-10-10 N1 39764 UR http:.

[23] K. v. Klitzing, G. Dorda, and M. Pepper. New method for high-accuracy determination of the fine-structure constant based on quantized hall resistance. *Phys. Rev. Lett.*, 45:494–497, Aug 1980.

[24] Charles Kane and Joel Moore. Topological insulators. *Physics World*, 24(02):32, 2011.

[25] Shuichi Murakami. Phase transition between the quantum spin hall and insulator phases in 3d: emergence of a topological gapless phase. *New Journal of Physics*, 9(9):356, 2007.

[26] Z. K. Liu, L. X. Yang, Y. Sun, T. Zhang, H. Peng, H. F. Yang, C. Chen, Y. Zhang, Y. F. Guo, D. Prabhakaran, M. Schmidt, Z. Hussain, S.-K. Mo, C. Felser, B. Yan, and Y. L. Chen. Evolution of the fermi surface of weyl semimetals in the transition metal pnictide family. *Nat Mater*, 15(1):27–31, January 2016.

[27] H. Hertz. Ueber einen einfluss des ultravioletten lichtes auf die electrische entladung. *Annalen der Physik*, 267(8):983–1000, 1887.

[28] Albert Einstein. The photoelectric effect. *Ann. Phys*, 17(132):4, 1905.

[29] D. A. Shirley. High-resolution x-ray photoemission spectrum of the valence bands of gold. *Phys. Rev. B*, 5:4709–4714, Jun 1972.

[30] Adam Kaminski and Helen M Fretwell. On the extraction of the self-energy from angle-resolved photoemission spectroscopy. *New Journal of Physics*, 7(1):98, 2005.

[31] M. R. Norman, H. Ding, H. Fretwell, M. Randeria, and J. C. Campuzano. Extraction of the electron self-energy from angle-resolved photoemission data: Application to $bi_2sr_2cacu_2o_{8+x}$. *Phys. Rev. B*, 60:7585–7590, Sep 1999.

[32] Wikipedia. Gas-discharge lamp — Wikipedia, the free encyclopedia, 2016.

[33] Wikipedia. Mu-metal — Wikipedia, the free encyclopedia, 2016.

[34] Wikipedia. Microchannel plate detector — Wikipedia, the free encyclopedia, 2016.

[35] Antonio Budano, Francesco Flora, and Luca Mezi. Analytical design method for a modified schwarzschild optics. *Appl. Opt.*, 45(18):4254–4262, Jun 2006.

[36] R Flkiger, S. Y. Hariharan, R. Kntzler, H. L Luo, F Weiss, T Wolf, and J. Q. Xu. *Nb-H - Nb-Zr, Nd - Np Nb-Ti*, volume 21b2. Landolt-Brnstein - Group III Condensed Matter, 1994.

[37] Wikipedia. List of thermal conductivities — Wikipedia, the free encyclopedia, 2016.

[38] Lunan Huang, Valentin Taufour, T. N. Lamichhane, Benjamin Schrunk, Sergei L. Bud'ko, P. C. Canfield, and Adam Kaminski. Imaging the magnetic nanodomains in $nd_2fe_{14}b$. *Phys. Rev. B*, 93:094408, Mar 2016.

[39] Gordon B. Haxel, James B. Hedrick, and Greta J. Orris. Rare earth elementscritical resources for high technology. *U.S. Geological Survey*, 2002.

[40] K.H.J. Buschow. New permanent magnet materials. *Materials Science Reports*, 1(1):1 – 63, 1986.

[41] I Nowik, K Muraleedharan, G Wortmann, B Perscheid, G Kaindl, and N.C Koon. Spin reorientation transition in $nd_2fe_{14}b$ studied by ^{145}nd-mssbauer spectroscopy. *Solid State Communications*, 76(8):967 – 970, 1990.

[42] H. Lemke, T. Goddenhenrich, C. Heiden, and G. Thomas. Thin nd-fe-b films analyzed by lorentz and magnetic force microscopy. *Magnetics, IEEE Transactions on*, 33(5):3865–3867, Sep 1997.

[43] P. Grtter, E. Meyer, H. Heinzelmann, L. Rosenthaler, H.R. Hidber, and H.J. Gntherodt. Application of atomic force microscopy to magnetic materials. *Journal of Vacuum Science & Technology A*, 6(2):279–282, 1988.

[44] Volker Neu, Steffen Melcher, Ullrich Hannemann, Sebastian Fähler, and Ludwig Schultz. Growth, microstructure, and magnetic properties of highly textured and highly coercive nd-fe-b films. *Phys. Rev. B*, 70:144418, Oct 2004.

[45] Witold Szmaja. Investigations of the domain structure of anisotropic sintered ndfeb-based permanent magnets. *Journal of Magnetism and Magnetic Materials*, 301(2):546 – 561, 2006.

[46] L. H. Lewis, J.-Y. Wang, and P. Canfield. Magnetic domains of single-crystal $nd_2fe_{14}b$ imaged by unmodified scanning electron microscopy. *Journal of Applied Physics*, 83(11):6843–6845, 1998.

[47] J.-Y. Wang, L.H. Lewis, D.O. Welch, and Paul Canfield. Magnetic domain imaging of nd2fe14b single crystals with unmodified scanning electron microscopy. *Materials Characterization*, 41(5):201 – 209, 1998.

[48] M. Al-Khafaji, W. M. Rainforth, M. R. J. Gibbs, J. E. L. Bishop, and H. A. Davies. The origin and interpretation of fine scale magnetic contrast in magnetic force microscopy: A study using single-crystal ndfeb and a range of magnetic force microscopy tips. *Journal of Applied Physics*, 83(11):6411–6413, 1998.

[49] Yu.G. Pastushenkov, A. Forkl, and H. Kronmller. Temperature dependence of the domain structure in fe14nd2b single crystals during the spin-reorientation transition. *Journal of Magnetism and Magnetic Materials*, 174(3):278 – 288, 1997.

[50] Bernard Dennis Cullity and Chad D Graham. *Introduction to magnetic materials*. John Wiley & Sons, 2011.

[51] Charles Kittel. Physical theory of ferromagnetic domains. *Rev. Mod. Phys.*, 21:541–583, Oct 1949.

[52] B.A. Lilley. Lxxi. energies and widths of domain boundaries in ferromagnetics. *The London, Edinburgh, and Dublin Philosophical Magazine and Journal of Science*, 41(319):792–813, 1950.

[53] G. Binnig, C. F. Quate, and Ch. Gerber. Atomic force microscope. *Phys. Rev. Lett.*, 56:930–933, Mar 1986.

[54] H. Hopster and H.P. Oepen. *Magnetic Microscopy of Nanostructures*. NanoScience and Technology. Springer, 2005.

[55] U. Hartmann. Magnetic force microscopy. *Annual Review of Materials Science*, 29(1):53–87, 1999.

[56] Paul C. Canfield and Ian R. Fisher. High-temperature solution growth of intermetallic single crystals and quasicrystals. *Journal of Crystal Growth*, 225(24):155 – 161, 2001. Proceedings of the 12th American Conference on Crystal Growth and Epitaxy.

[57] A. Hubert. Zur theorie der zweiphasigen domnenstrukturen in supraleitern und ferromagneten. *physica status solidi (b)*, 24(2):669–682, 1967.

[58] R. Szymczak, H. Szymczak, and E. Burzo. Domain wall energy in $nd_2(fe, co, al)_{14}b$ alloys. *Magnetics, IEEE Transactions on*, 23(5):2536–2538, Sep 1987.

[59] M.A. Al-Khafaji, W.M. Rainforth, M.R.J. Gibbs, J.E.L. Bishop, and H.A. Davies. The effect of tip type and scan height on magnetic domain images obtained by mfm. *Magnetics, IEEE Transactions on*, 32(5):4138–4140, Sep 1996.

[60] P. R. Wallace. The band theory of graphite. *Phys. Rev.*, 71:622–634, May 1947.

[61] K. S. Novoselov, A. K. Geim, S. V. Morozov, D. Jiang, Y. Zhang, S. V. Dubonos, I. V. Grigorieva, and A. A. Firsov. Electric field effect in atomically thin carbon films. *Science*, 306(5696):666–669, 2004.

[62] Alexander A. Balandin, Suchismita Ghosh, Wenzhong Bao, Irene Calizo, Desalegne Teweldebrhan, Feng Miao, and Chun Ning Lau. Superior thermal conductivity of single-layer graphene. *Nano Letters*, 8(3):902–907, 2008. PMID: 18284217.

[63] Xu Du, Ivan Skachko, Anthony Barker, and Eva Y. Andrei. Approaching ballistic transport in suspended graphene. *Nature Nanotechnology*, 3(8):491495, Jul 2008.

[64] K.I. Bolotin, K.J. Sikes, Z. Jiang, M. Klima, G. Fudenberg, J. Hone, P. Kim, and H.L. Stormer. Ultrahigh electron mobility in suspended graphene. *Solid State Communications*, 146(910):351 – 355, 2008.

[65] Cheol-Hwan Park, Li Yang, Young-Woo Son, Marvin L. Cohen, and Steven G. Louie. Anisotropic behaviours of massless dirac fermions in graphene under periodic potentials. *Nat Phys*, 4(3):213–217, March 2008.

[66] Cheol-Hwan Park, Li Yang, Young-Woo Son, Marvin L. Cohen, and Steven G. Louie. New generation of massless dirac fermions in graphene under external periodic potentials. *Phys. Rev. Lett.*, 101:126804, Sep 2008.

[67] L. A. Ponomarenko, R. V. Gorbachev, G. L. Yu, D. C. Elias, R. Jalil, A. A. Patel, A. Mishchenko, A. S. Mayorov, C. R. Woods, J. R. Wallbank, M. Mucha-Kruczynski, B. A. Piot, M. Potemski, I. V. Grigorieva, K. S. Novoselov, F. Guinea, V. I. Fal/'ko, and A. K. Geim. Cloning of dirac fermions in graphene superlattices. *Nature*, 497(7451):594–597, May 2013.

[68] Rgis Decker, Yang Wang, Victor W. Brar, William Regan, Hsin-Zon Tsai, Qiong Wu, William Gannett, Alex Zettl, and Michael F. Crommie. Local electronic properties of graphene on a bn substrate via scanning tunneling microscopy. *Nano Letters*, 11(6):2291–2295, 2011. PMID: 21553853.

[69] Douglas R. Hofstadter. Energy levels and wave functions of bloch electrons in rational and irrational magnetic fields. *Phys. Rev. B*, 14:2239–2249, Sep 1976.

[70] C. R. Dean, L. Wang, P. Maher, C. Forsythe, F. Ghahari, Y. Gao, J. Katoch, M. Ishigami, P. Moon, M. Koshino, T. Taniguchi, K. Watanabe, K. L. Shepard, J. Hone, and P. Kim. Hofstadter/'s butterfly and the fractal quantum hall effect in moire superlattices. *Nature*, 497(7451):598–602, May 2013.

[71] B. Hunt, J. D. Sanchez-Yamagishi, A. F. Young, M. Yankowitz, B. J. LeRoy, K. Watanabe, T. Taniguchi, P. Moon, M. Koshino, P. Jarillo-Herrero, and R. C. Ashoori. Massive dirac fermions and hofstadter butterfly in a van der waals heterostructure. *Science*, 340(6139):1427–1430, 2013.

[72] G. L. Yu, R. V. Gorbachev, J. S. Tu, A. V. Kretinin, Y. Cao, R. Jalil, F. Withers, L. A. Ponomarenko, B. A. Piot, M. Potemski, D. C. Elias, X. Chen, K. Watanabe, T. Taniguchi, I. V. Grigorieva, K. S. Novoselov, V. I. Fal/'ko, A. K. Geim, and A. Mishchenko. Hierarchy of hofstadter states and replica quantum hall ferromagnetism in graphene superlattices. *Nat Phys*, 10(7):525–529, July 2014.

[73] Lei Wang, Yuanda Gao, Bo Wen, Zheng Han, Takashi Taniguchi, Kenji Watanabe, Mikito Koshino, James Hone, and Cory R. Dean. Evidence for a fractional fractal quantum hall effect in graphene superlattices. *Science*, 350(6265):1231–1234, 2015.

[74] A.J. Van Bommel, J.E. Crombeen, and A. Van Tooren. {LEED} and auger electron observations of the sic(0001) surface. *Surface Science*, 48(2):463 – 472, 1975.

[75] Ulrich Starke, M Franke, J Bernhardt, J Schardt, K Reuter, and K Heinz. Large unit cell superstructures on hexagonal sic-sufaces studied by leed, aes and stm. *Materials Science Forum*, 264:321–326, 1997.

[76] I. Forbeaux, J.-M. Themlin, and J.-M. Debever. Heteroepitaxial graphite on $6h-$SiC(0001) : interface formation through conduction-band electronic structure. *Phys. Rev. B*, 58:16396–16406, Dec 1998.

[77] P. Lauffer, K. V. Emtsev, R. Graupner, Th. Seyller, L. Ley, S. A. Reshanov, and H. B. Weber. Atomic and electronic structure of few-layer graphene on sic(0001) studied with scanning tunneling microscopy and spectroscopy. *Phys. Rev. B*, 77:155426, Apr 2008.

[78] J Hass, W A de Heer, and E H Conrad. The growth and morphology of epitaxial multilayer graphene. *Journal of Physics: Condensed Matter*, 20(32):323202, 2008.

[79] P. Xu, D. Qi, J.K. Schoelz, J. Thompson, P.M. Thibado, V.D. Wheeler, L.O. Nyakiti, R.L. Myers-Ward, C.R. Eddy, D.K. Gaskill, and et al. Multilayer graphene, moir patterns, grain boundaries and defects identified by scanning tunneling microscopy on the m-plane, non-polar surface of SiC. *Carbon*, 80:7581, Dec 2014.

[80] Taisuke Ohta, Aaron Bostwick, J. L. McChesney, Thomas Seyller, Karsten Horn, and Eli Rotenberg. Interlayer interaction and electronic screening in multilayer graphene investigated with angle-resolved photoemission spectroscopy. *Phys. Rev. Lett.*, 98:206802, May 2007.

[81] F. Varchon, R. Feng, J. Hass, X. Li, B. Ngoc Nguyen, C. Naud, P. Mallet, J.-Y. Veuillen, C. Berger, E. H. Conrad, and L. Magaud. Electronic structure of epitaxial graphene layers on sic: Effect of the substrate. *Phys. Rev. Lett.*, 99:126805, Sep 2007.

[82] S. Y. Zhou, G.-H. Gweon, A. V. Fedorov, P. N. First, W. A. de Heer, D.-H. Lee, F. Guinea, A. H. Castro Neto, and A. Lanzara. Substrate-induced bandgap opening in epitaxial graphene. *Nat Mater*, 6(10):770–775, October 2007.

[83] Aaron Bostwick, Taisuke Ohta, Thomas Seyller, Karsten Horn, and Eli Rotenberg. Quasiparticle dynamics in graphene. *Nature Physics*, 3(1):3640, Dec 2006.

[84] Taisuke Ohta, Aaron Bostwick, Thomas Seyller, Karsten Horn, and Eli Rotenberg. Controlling the electronic structure of bilayer graphene. *Science*, 313(5789):951–954, 2006.

[85] Aaron Bostwick, Taisuke Ohta, Jessica L McChesney, Konstantin V Emtsev, Thomas Seyller, Karsten Horn, and Eli Rotenberg. Symmetry breaking in few layer graphene films. *New Journal of Physics*, 9(10):385, 2007.

[86] M. Mucha-Kruczyński, O. Tsyplyatyev, A. Grishin, E. McCann, Vladimir I. Fal'ko, Aaron Bostwick, and Eli Rotenberg. Characterization of graphene through anisotropy of constant-energy maps in angle-resolved photoemission. *Phys. Rev. B*, 77:195403, May 2008.

[87] Taisuke Ohta, Farid El Gabaly, Aaron Bostwick, Jessica L McChesney, Konstantin V Emtsev, Andreas K Schmid, Thomas Seyller, Karsten Horn, and Eli Rotenberg. Morphology of graphene thin film growth on sic(0001). *New Journal of Physics*, 10(2):023034, 2008.

[88] S. Y. Zhou, D. A. Siegel, A. V. Fedorov, and A. Lanzara. Metal to insulator transition in epitaxial graphene induced by molecular doping. *Phys. Rev. Lett.*, 101:086402, Aug 2008.

[89] Isabella Gierz, Jürgen Henk, Hartmut Höchst, Christian R. Ast, and Klaus Kern. Illuminating the dark corridor in graphene: Polarization dependence of angle-resolved photoemission spectroscopy on graphene. *Phys. Rev. B*, 83:121408, Mar 2011.

[90] Andrew L. Walter, Aaron Bostwick, Ki-Joon Jeon, Florian Speck, Markus Ostler, Thomas Seyller, Luca Moreschini, Young Jun Chang, Marco Polini, Reza Asgari, Allan H. MacDonald, Karsten Horn, and Eli Rotenberg. Effective screening and the plasmaron bands in graphene. *Phys. Rev. B*, 84:085410, Aug 2011.

[91] Taisuke Ohta, Jeremy T. Robinson, Peter J. Feibelman, Aaron Bostwick, Eli Rotenberg, and Thomas E. Beechem. Evidence for interlayer coupling and moiré periodic potentials in twisted bilayer graphene. *Phys. Rev. Lett.*, 109:186807, Nov 2012.

[92] M. S. Nevius, M. Conrad, F. Wang, A. Celis, M. N. Nair, A. Taleb-Ibrahimi, A. Tejeda, and E. H. Conrad. Semiconducting graphene from highly ordered substrate interactions. *Physical Review Letters*, 115(13), Sep 2015.

[93] K. Oura, M. Katayama, A. V. Zotov, V. G. Lifshits, and A. A. Saranin. *Surface Science: An Introduction*, chapter Experimental Background, pages 19–46. Springer Berlin Heidelberg, Berlin, Heidelberg, 2003.

[94] L. de Broglie. Waves and Quanta. *Nature*, 112:540, October 1923.

[95] P. A. M. Dirac. The quantum theory of the electron. *Proceedings of the Royal Society of London A: Mathematical, Physical and Engineering Sciences*, 117(778):610–624, 1928.

[96] H Weyl. Gravitation and the Electron. *Proceedings of the National Academy of Sciences of the United States of America*, 15(4):323–334, 1929.

[97] J. Schechter and J. W. F. Valle. Neutrino masses in su(2) $\bigotimes$ u(1) theories. *Phys. Rev. D*, 22:2227–2235, Nov 1980.

[98] Xiangang Wan, Ari M. Turner, Ashvin Vishwanath, and Sergey Y. Savrasov. Topological semimetal and Fermi-arc surface states in the electronic structure of pyrochlore iridates. *Physical Review B - Condensed Matter and Materials Physics*, 83(20):1–9, 2011.

[99] E.H. Hall. Xxxviii. on the new action of magnetism on a permanent electric current. *Philosophical Magazine Series 5*, 10(63):301–328, 1880.

[100] D. J. Thouless, M. Kohmoto, M. P. Nightingale, and M. den Nijs. Quantized hall conductance in a two-dimensional periodic potential. *Phys. Rev. Lett.*, 49:405–408, Aug 1982.

[101] C. L. Kane and E. J. Mele. Z_2 topological order and the quantum spin hall effect. *Phys. Rev. Lett.*, 95:146802, Sep 2005.

[102] Liang Fu, C. L. Kane, and E. J. Mele. Topological insulators in three dimensions. *Phys. Rev. Lett.*, 98:106803, Mar 2007.

[103] Liang Fu and C. L. Kane. Topological insulators with inversion symmetry. *Phys. Rev. B*, 76:045302, Jul 2007.

[104] Sung-Sik Lee and Shinsei Ryu. Many-body generalization of the z_2 topological invariant for the quantum spin hall effect. *Phys. Rev. Lett.*, 100:186807, May 2008.

[105] Liang Fu and C. L. Kane. Time reversal polarization and a Z_2 adiabatic spin pump. *Phys. Rev. B*, 74:195312, Nov 2006.

[106] Shuichi Murakami, Satoshi Iso, Yshai Avishai, Masaru Onoda, and Naoto Nagaosa. Tuning phase transition between quantum spin hall and ordinary insulating phases. *Phys. Rev. B*, 76:205304, Nov 2007.

[107] G.E. Volovik. Superfluid analogies of cosmological phenomena. *Physics Reports*, 351(4):195 – 348, 2001.

[108] Shuichi Murakami and Naoto Nagaosa. Berry phase in magnetic superconductors. *Phys. Rev. Lett.*, 90:057002, Feb 2003.

[109] A. A. Zyuzin, Si Wu, and A. A. Burkov. Weyl semimetal with broken time reversal and inversion symmetries. *Phys. Rev. B*, 85:165110, Apr 2012.

[110] Shin-Ming Huang, Su-Yang Xu, Ilya Belopolski, Chi-Cheng Lee, Guoqing Chang, BaoKai Wang, Nasser Alidoust, Guang Bian, Madhab Neupane, Chenglong Zhang, Shuang Jia, Arun Bansil, Hsin Lin, and M. Zahid Hasan. A weyl fermion semimetal with surface fermi arcs in the transition metal monopnictide taas class. *Nat Commun*, 6:–, June 2015.

[111] B. Andrei Bernevig, Taylor L. Hughes, and Shou-Cheng Zhang. Quantum spin hall effect and topological phase transition in hgte quantum wells. *Science*, 314(5806):1757–1761, 2006.

[112] D. Hsieh, D. Qian, L. Wray, Y. Xia, Y. S. Hor, R. J. Cava, and M. Z. Hasan. A topological dirac insulator in a quantum spin hall phase. *Nature*, 452(7190):970–974, April 2008.

[113] Y. Xia, D. Qian, D Hsieh, L. Wray, A. Pal, H. Lin, A. Bansil, Y.S. Hor D. Grauer, R.J. Cava, and M.Z.Hasan. Observation of a large-gap topological-insulator class with a single dirac cone on the surface. *Nat Phys*, 5:398402, Jun 2009.

[114] Su-Yang Xu, Ilya Belopolski, Nasser Alidoust, Madhab Neupane, Guang Bian, Chenglong Zhang, Raman Sankar, Guoqing Chang, Zhujun Yuan, Chi-Cheng Lee, Shin-Ming Huang, Hao Zheng, Jie Ma, Daniel S. Sanchez, BaoKai Wang, Arun Bansil, Fangcheng Chou, Pavel P. Shibayev, Hsin Lin, Shuang Jia, and M. Zahid Hasan. Discovery of a weyl fermion semimetal and topological fermi arcs. *Science*, 349(6248):613–617, 2015.

[115] B. Q. Lv, H. M. Weng, B. B. Fu, X. P. Wang, H. Miao, J. Ma, P. Richard, X. C. Huang, L. X. Zhao, G. F. Chen, Z. Fang, X. Dai, T. Qian, and H. Ding. Experimental discovery of weyl semimetal taas. *Phys. Rev. X*, 5:031013, Jul 2015.

[116] M. Sprinkle, D. Siegel, Y. Hu, J. Hicks, A. Tejeda, A. Taleb-Ibrahimi, P. Le Fèvre, F. Bertran, S. Vizzini, H. Enriquez, S. Chiang, P. Soukiassian, C. Berger, W. A. de Heer, A. Lanzara, and E. H. Conrad. First direct observation of a nearly ideal graphene band structure. *Phys. Rev. Lett.*, 103:226803, Nov 2009.

[117] Z. K. Liu, B. Zhou, Y. Zhang, Z. J. Wang, H. M. Weng, D. Prabhakaran, S.-K. Mo, Z. X. Shen, Z. Fang, X. Dai, Z. Hussain, and Y. L. Chen. Discovery of a three-dimensional topological dirac semimetal, na_3bi. *Science*, 343(6173):864–867, 2014.

[118] Z. K. Liu, J. Jiang, B. Zhou, Z. J. Wang, Y. Zhang, H. M. Weng, D. Prabhakaran, S-K. Mo, H. Peng, P. Dudin, T. Kim, M. Hoesch, Z. Fang, X. Dai, Z. X. Shen, D. L. Feng, Z. Hussain, and Y. L. Chen. A stable three-dimensional topological dirac semimetal cd_3as_2. *Nat Mater*, 13:677681, Jul 2014.

[119] Su-Yang Xu, Nasser Alidoust, Ilya Belopolski, Chenglong Zhang, Guang Bian, Tay-Rong Chang, Hao Zheng, Vladimir Strokov, Daniel S Sanchez, Guoqing Chang, et al. Discovery of weyl semimetal nbas. *Preprint at http://arxiv. org/abs/1504.01350*, 2015.

[120] Su-Yang Xu, Ilya Belopolski, Daniel S. Sanchez, Chenglong Zhang, Guoqing Chang, Cheng Guo, Guang Bian, Zhujun Yuan, Hong Lu, Tay-Rong Chang, Pavel P. Shibayev, Mykhailo L. Prokopovych, Nasser Alidoust, Hao Zheng, Chi-Cheng Lee, Shin-Ming Huang, Raman Sankar, Fangcheng Chou, Chuang-Han Hsu, Horng-Tay Jeng, Arun Bansil, Titus Neupert, Vladimir N. Strocov, Hsin Lin, Shuang Jia, and M. Zahid Hasan. Experimental discovery of a topological weyl semimetal state in tap. *Science Advances*, 1(10), 2015.

[121] J.S. Bell and R. Jackiw. A pcac puzzle: 0 in the -model. *Il Nuovo Cimento A*, 60(1):47–61, 1969.

[122] Stephen L. Adler. Axial-vector vertex in spinor electrodynamics. *Phys. Rev.*, 177:2426–2438, Jan 1969.

[123] H. B. Nielsen and M. Ninomiya. The Adler-Bell-Jackiw anomaly and Weyl fermions in a crystal. *Physics Letters B*, 130:389–396, November 1983.

[124] Phillip E. C. Ashby and J. P. Carbotte. Magneto-optical conductivity of weyl semimetals. *Phys. Rev. B*, 87:245131, Jun 2013.

[125] A. A. Burkov and Leon Balents. Weyl semimetal in a topological insulator multilayer. *Phys. Rev. Lett.*, 107:127205, Sep 2011.

[126] Gang Xu, Hongming Weng, Zhijun Wang, Xi Dai, and Zhong Fang. Chern semimetal and the quantized anomalous hall effect in $hgcr_2se_4$. *Phys. Rev. Lett.*, 107:186806, Oct 2011.

[127] Kai-Yu Yang, Yuan-Ming Lu, and Ying Ran. Quantum hall effects in a weyl semimetal: Possible application in pyrochlore iridates. *Phys. Rev. B*, 84:075129, Aug 2011.

[128] Adolfo G. Grushin. Consequences of a condensed matter realization of lorentz-violating qed in weyl semi-metals. *Phys. Rev. D*, 86:045001, Aug 2012.

[129] S. A. Parameswaran, T. Grover, D. A. Abanin, D. A. Pesin, and A. Vishwanath. Probing the chiral anomaly with nonlocal transport in three-dimensional topological semimetals. *Phys. Rev. X*, 4:031035, Sep 2014.

[130] C. Zhang, E. Zhang, Y. Liu, Z.-G. Chen, S. Liang, J. Cao, X. Yuan, L. Tang, Q. Li, T. Gu, Y. Wu, J. Zou, and F. Xiu. Detection of chiral anomaly and valley transport in Dirac semimetals. *ArXiv e-prints*, April 2015.

[131] L. Huang, T. M. McCormick, M. Ochi, Z. Zhao, M.-t. Suzuki, R. Arita, Y. Wu, D. Mou, H. Cao, J. Yan, N. Trivedi, and A. Kaminski. Spectroscopic evidence for type II Weyl semimetal state in MoTe2. *ArXiv e-prints*, March 2016.

[132] Hongming Weng, Chen Fang, Zhong Fang, B. Andrei Bernevig, and Xi Dai. Weyl semimetal phase in noncentrosymmetric transition-metal monophosphides. *Phys. Rev. X*, 5:011029, Mar 2015.

[133] L. X. Yang, Z. K. Liu, Y. Sun, H. Peng, H. F. Yang, T. Zhang, B. Zhou, Y. Zhang, Y. F. Guo, M. Rahn, D. Prabhakaran, Z. Hussain, S.-K. Mo, C. Felser, B. Yan, and Y. L.

Chen. Weyl semimetal phase in the non-centrosymmetric compound taas. *Nat Phys*, 11(9):728–732, September 2015.

[134] N. Xu, H. M. Weng, B. Q. Lv, C. E. Matt, J. Park, F. Bisti, V. N. Strocov, D. Gawryluk, E. Pomjakushina, K. Conder, N. C. Plumb, M. Radovic, G. Autes, O. V. Yazyev, Z. Fang, X. Dai, T. Qian, J. Mesot, H. Ding, and M. Shi. Observation of weyl nodes and fermi arcs in tantalum phosphide. *Nat Commun*, 7:–, March 2016.

[135] Su-Yang Xu, Nasser Alidoust, Ilya Belopolski, Zhujun Yuan, Guang Bian, Tay-Rong Chang, Hao Zheng, Vladimir N. Strocov, Daniel S. Sanchez, Guoqing Chang, Chenglong Zhang, Daixiang Mou, Yun Wu, Lunan Huang, Chi-Cheng Lee, Shin-Ming Huang, BaoKai Wang, Arun Bansil, Horng-Tay Jeng, Titus Neupert, Adam Kaminski, Hsin Lin, Shuang Jia, and M. Zahid Hasan. Discovery of a weyl fermion state with fermi arcs in niobium arsenide. *Nat Phys*, 11(9):748–754, September 2015.

[136] Fumiyuki Ishii, Yo Pierre Mizuta, Takehiro Kato, Taisuke Ozaki, Hongming Weng, and Shigeki Onoda. First-principles study on cubic pyrochlore iridates $y_2ir_2o_7$ and $pr_2ir_2o_7$. *Journal of the Physical Society of Japan*, 84(7):073703, 2015.

[137] Yuanping Chen, Yuee Xie, Shengyuan A. Yang, Hui Pan, Fan Zhang, Marvin L. Cohen, and Shengbai Zhang. Nanostructured carbon allotropes with weyl-like loops and points. *Nano Lett.*, 15(10):6974–6978, October 2015.

[138] Yan Sun, Shu-Chun Wu, Mazhar N. Ali, Claudia Felser, and Binghai Yan. Prediction of weyl semimetal in orthorhombic $mote_2$. *Phys. Rev. B*, 92:161107, Oct 2015.

[139] Alexey A. Soluyanov, Dominik Gresch, Zhijun Wang, QuanSheng Wu, Matthias Troyer, Xi Dai, and B. Andrei Bernevig. Type-ii weyl semimetals. *Nature*, 527(7579):495–498, November 2015.

[140] S.-M. Huang, S.-Y. Xu, I. Belopolski, C.-C. Lee, G. Chang, B. Wang, N. Alidoust, M. Neupane, H. Zheng, D. Sanchez, A. Bansil, G. Bian, H. Lin, and M. Zahid Hasan. A new type of Weyl semimetal with quadratic double Weyl fermions in $SrSi_2$. *ArXiv e-prints*, March 2015.

[141] Z. Wang, D. Gresch, A. A. Soluyanov, W. Xie, S. Kushwaha, X. Dai, M. Troyer, R. J. Cava, and B. A. Bernevig. MoTe2: Weyl and Line Node Topological Metal. *ArXiv e-prints*, November 2015.

[142] A. A. Burkov, M. D. Hook, and Leon Balents. Topological nodal semimetals. *Phys. Rev. B*, 84:235126, Dec 2011.

[143] T. T. Heikkilä and G. E. Volovik. Dimensional crossover in topological matter: Evolution of the multiple dirac point in the layered system to the flat band on the surface. *JETP Letters*, 93(2):59–65, 2011.

[144] Y. Wu, L.-L. Wang, E. Mun, D. D. Johnson, D. Mou, L. Huang, Y. Lee, S. L. Budko, P. C. Canfield, and A. Kaminski. Discovery of Dirac Node Arcs in PtSn4. *ArXiv e-prints*, March 2016.

[145] Ilya Belopolski, Su-Yang Xu, Yukiaki Ishida, Xingchen Pan, Peng Yu, Daniel S Sanchez, Madhab Neupane, Nasser Alidoust, Guoqing Chang, Tay-Rong Chang, Yun Wu, Guang Bian, Hao Zheng, Shin-Ming Huang, Chi-Cheng Lee, Daixiang Mou, Lunan Huang, You Song, Baigeng Wang, Guanghou Wang, Yao-Wen Yeh, Nan Yao, Julien Rault, Patrick Lefevre, François Bertran, Horng-Tay Jeng, Takeshi Kondo, Adam Kaminski, Hsin Lin, Zheng Liu, Fengqi Song, Shik Shin, and M Zahid Hasan. Unoccupied electronic structure and signatures of topological Fermi arcs in the Weyl semimetal candidate $Mo_xW_{1-x}Te_2$. *arXiv.org*, December 2015.

[146] Paul C. Canfield, Tai Kong, Udhara S. Kaluarachchi, and Na Hyun Jo. Use of frit-disc crucibles for routine and exploratory solution growth of single crystalline samples. *Philosophical Magazine*, 96(1):84–92, 2016.

[147] Rui Jiang, Daixiang Mou, Yun Wu, Lunan Huang, Colin D. McMillen, Joseph Kolis, Henry G. Giesber, John J. Egan, and Adam Kaminski. Tunable vacuum ultraviolet laser based spectrometer for angle resolved photoemission spectroscopy. *Review of Scientific Instruments*, 85(3), 2014.

[148] J. P. Perdew, K. Burke, and M. Ernzerhof. Generalized gradient approximation made simple. *Phys. Rev. Lett.*, 77:3865, 1996.

[149] P. Blaha, K. Schwarz, G. K. H. Madsen, D. Kvasnicka, and J. Luitz, 2001. WIEN2k, *An Augmented Plane Wave + Local Orbitals Program for Calculating Crystal Properties* (Karlheinz Schwarz, Techn. Universität Wien, Austria), ISBN 3-9501031-1-2; http://www.wien2k.at.

[150] N. Marzari and D. Vanderbilt. Maximally localized generalized wannier functions for composite energy bands. *Phys. Rev. B*, 56:12847, 1997.

[151] I. Souza, N. Marzari, and D. Vanderbilt. Maximally localized wannier functions for entangled energy bands. *Phys. Rev. B*, 65:035109, 2001.

[152] A. A. Mostofi, J. R. Yates, Y.-S. Lee, I. Souza, D. Vanderbilt, and N. Marzari. Wannier90: A tool for obtaining maximally-localized wannier functions. *Comput. Phys. Commun.*, 178:685, 2008.

[153] X. Wang, J. R. Yates, I. Souza, and D. Vanderbilt. *Ab initio* calculation of the anomalous hall conductivity by wannier interpolation. *Phys. Rev. B*, 74:195118, 2006.